Institute for Nuclear Research
Russian Academy of Sciences
60th October Anniversary Prospect, 7A
Moscow, 117 312, Russia

Conceptual Design of a Positron Pre-Accelerator for the TESLA Linear Collider

Moscow-Hamburg, 1999

Working group:

INR

V.V. Balandin, N.I. Golubeva, I.V. Gonin, A.I. Kvasha, A.S. Kovalishin, L.V. Kravchuk, V.A. Moiseev, V.N. Mikhailov, V.V. Paramonov, O.D. Pronin, V.L. Serov, A.A. Stepanov, P.I. Reinhardt-Nickoulin, A.V. Vasyuchenko

DESY

K. Flöttmann

Edited by V.V. Paramonov, K. Flöttmann

Moscow-Hamburg, 1999

Contents

1 Introduction

The conceptual design of the TESLA 500 GeV electron-positron linear collider with integrated X-ray laser facility is presented in [1]. The collider will use the spent electron beam (250 GeV, after collision at the Interaction Point (IP)) to produce a positron beam, by passing the spent electron beam through a wiggler to produce photons, which will hit a thin target to yield the positrons. This scheme of the positrons source, proposed in [2] and investigated in [3] has the advantage of having a higher positron yield and a better positron beam performance at the target, as compared to the conventional concept of aiming high energy electrons onto a thick target.

The capture optics behind the target is of a conventional design. Since the positrons have a broad distribution of transverse and longitudinal momenta they have to be accelerated in an acceleration section embedded in a solenoid field. The acceptance of a solenoid channel is characterized by a large spot size and small angles while the positrons emerging from the target have a small spot size and large angles. To match the positrons to the acceptance of the solenoid, an Adiabatic Matching Device (AMD) is used. It consists of a tapered solenoid field which starts with a higher initial field and tapers down adiabatically to the constant end field [1].

After AMD the positron beam should be captured, pre-accelerated to $\approx 250\,\mathrm{MeV}$ in the Positron Pre-Accelerator (PPA) linac, transported to the superconducting linac, accelerated to $\approx 3\,\mathrm{GeV}$ and injected into the Damping Ring (DR). The acceptance of the DR is limited. Moreover, there should be no particle losses in the superconducting linac.

Despite of the correction of the particle momentum distributions in the AMD, both longitudinal and transverse positron momentum distribution functions are wider than for incoming beams in usual linacs. Therefore the quality of the positron beam is mainly formed within the AMD and the PPA.

The main PPA purpose is to provide a maximum capture efficiency for the useful part of the totally acceptable e^+ beam with technically reasonable parameters of the linac.

2 Beam Dynamics in the PPA

The main goal of our study is to design a positron pre-accelerator with as high as possible capture efficiency, which is determined as the ratio of the number of positron acceptable for further acceleration to the number of positrons emerging from the target. We suppose that a magnetic field law in the AMD has been preliminary defined as well as the incoming positron and electron phase space distributions [3].
Behind the positron target there will be a large background of positrons, electrons, photons and neutrons which will deposit energy in the first cavities. For this reason the pre-accelerator has to be done with normal conducting cavities up to an energy of $100 \div 250\,\mathrm{MeV}$, where the positrons can be separated from the background and further accelerated up to $\sim 3\,\mathrm{GeV}$ by using the TESLA superconducting structure [1].
The beam dynamics in the PPA has been studied by a modified LINCIC code [4]. It permits to simulate the particle dynamics in the time domain for realistic electric and magnetic fields of the accelerating and focusing elements. The space charge effects are excluded because the particles have a comparatively high energy ($> 2\,\mathrm{MeV}$), beam emittance is enough large and due to the fact that the positrons are overlapped in space with electrons which leads to charge compensation at least at the AMD and PPA input. The differently charged particles are separated in the accelerating cavities at higher energies.
In our case according to the previous notes the modified LINCIC code simulates the single particle dynamics. The rf electric and magnetic fields are calculated separately by MAFIA and accepted by the code. For static magnetic elements the analytical description is used.

2.1 Beam Parameters

From the computed distributions of the accepted positrons and electrons at the AMD exit (AMD length is more than 80 cm) one can estimate that:
- The total energy spread is $1 \div 300\,\mathrm{MeV}$ and approximately one-half of the total number of positrons lies within the energy range $3 \div 24\,\mathrm{MeV}$ with average energy about $10 \div 12\,\mathrm{MeV}$.
- The transverse momentum can reach $0.5\,\mathrm{MeV/c}$.
- The total bunch length is extended up to $14 \div 18\,\mathrm{cm}$. The main part of particles ($\sim 90\%$) occupies the longitudinal interval of $3 \div 3.5\,\mathrm{cm}$.
- The number of electrons is about a factor of 1.7 higher than the number of positrons. These electrons are overlapped with positrons in the same space at the PPA input.

The time structure of the positron beam [1]:

Repetition rate, Hz	5
Beam pulse length, μs	800
Number of bunches per pulse	1130
Bunch spacing, ns	708

The positron beam requirements at the entrance of the Damping Ring (DR) and Interaction Point (IP) [1] are:
- The total normalized transverse beam emittance should satisfy the condition $\varepsilon_x + \varepsilon_y \leq 0.048\,\mathrm{m}$.
- The acceptable energy and phase spreads required for the DR are about $\pm 1\%$ and $\pm 7.5^o$ for L-band (1.3 GHz) operating frequency, respectively.
- The number of positrons per bunch should be $3.63 \cdot 10^{10}$ at the IP.

According to these requirements we suppose that the positron beam parameters at the PPA

output acceptable for further acceleration in the DR are:
- The normalized transverse beam emittance

$$\varepsilon_x + \varepsilon_y \leq 0.048\,\mathrm{m}.$$

- The average energy $\sim 250\,\mathrm{MeV}$.
- The energy acceptance of $\pm 6\%$ (recalculated to the PPA output energy) and phase spread $\pm 7.5\%$ for L-band frequency with respect to an optimized point in the longitudinal phase space of the positron beam.
- The number of positrons per bunch $9.08 \cdot 10^{10}$. Here the safety factor of 2.5 (it is defined as ratio of the accepted positrons at the PPA output to the required number of positrons at IP) is taken into account.

2.2 Preliminary Study

The particles which leave the AMD have to be accelerated in a cavity embedded in a uniform solenoid field for focusing. Here the final emittance and the efficiency of the positron source are mainly defined.
Several reference PPA options were considered assuming focusing with a solenoid to explore the influence of different parameters for the PPA performance.
Accelerating gradient E_0T. An important effect is the bunch lengthening in the axial magnetic field of the AMD and first accelerating structures where the ratio of the transverse momenta to the longitudinal momenta is still large. It leads to a broadening of the output positron energy spectrum. The particle dephasing in the subsequent Accelerating Sections (AS) depends on E_0T and can be sufficiently suppressed by keeping E_0T as high as possible to accelerate the positrons up to more relativistic energies. The test simulation (solenoid magnetic field B=0.32 T, AS aperture diameter D= 52 mm) has shown an increase of the PPA capture efficiency from 23.5% up to 26.8% when E_0T was changed from 8 MV/m to 16 MV/m. Moreover, the number of captured electrons was reduced by a factor 1.5. When the high gradient was kept up to an average energy of $\sim 40\,\mathrm{MeV}$ and then a transition to a moderate gradient AS was made, the capture efficiency was equal to 25.3%.
Aperture diameter D= $2a$. The transverse acceptance of the PPA depends on the solenoid field B and the aperture radius of the accelerating structure. The choice of a large aperture helps in improving the transverse acceptance. However, bunch lengthening due to particle spiralling in the longitudinal magnetic field is made easier in large apertures [3]. The test simulations were carried out for B= 0.16 T; $E_0T = 12\,\mathrm{MV/m}$ and an aperture diameter of 40 mm and 52 mm. The capture efficiency was 15% and 18.1% respectively. It should be pointed out here that by changing the aperture diameter the number of the positrons acceptable in the longitudinal phase space at the PPA exit is appoximately proportional to the number of positrons incoming to the PPA. But the latter number varies slower than the aperture square. Apparently it takes place due to the angular distribution of positrons emerging from the target. Also, at the PPA exit, from the number of positrons acceptable in the longitudinal phase space, there is a part of the positrons which populates the required transverse phase space volume. This part grows slower starting from some aperture due to the fact that the PPA acceptance becomes higher than the required transverce emittance. Moreover, there are technical reasons connected with rf requirements limiting the aperture diameter. In detail the rf problems will be discussed in Chapter 3.

Note, that by increasing the aperture we also increase the number of electrons and parasitic positrons (not acceptable for DR) in the PPA.

Solenoid magnetic field B. Rising the longitudinal magnetic field of the solenoid surrounding the accelerator structure we improve the capture efficiency and increase the transverse acceptance of the PPA. In addition the AMD becomes shorter resulting in a reduction of the dephasing at the PPA input. The test simulations (D=52 mm; E_0T = 7.5 MV/m) for B= 0.16 T and B= 0.32 T have shown capture efficiencies of 18.1% and 20.4% respectively. Like in the previous case the capture efficiency grows slower than the number of positrons acceptable in the longitudinal phase space due to the transverse emittance limitation. Also the magnetic field increasing is related with technical problems (the main one is the DC power consumption). In detail the solenoid design and operating parameters are discussed in Chapter 6.

From the results of the preliminary simulations we have chosen the main parameters as follows:

Aperture diameter of the cavity	D= 52 mm
Field strength of the solenoid	B= 0.24 T
AMD length	0.8 m

In this case the PPA acceptance will be about twice the DR acceptance. This reserve permits to optimize the capture efficiency carefully. If it will be necessary, the transverse phase space can be scraped further downstream.

2.3 PPA Accelerating Structure

We propose to use a standing wave structure for $\beta = 1$ with π-operating mode as a good candidate for the positron pre-accelerator. The complex analysis of this choice is presented in Chapter 3.

The segmentation of the accelerating structure into independent resonators and into separate sections is determined by the available klystron power. The application of a standard TESLA main linac klystron with rf-output of 10 MW at 1.3 GHz is expected.

Segmentation. AMD is followed by the four high gradient ($\sim$ 14.9 MV/m) accelerating sections. These sections are followed by 14 moderate gradient ($\sim$ 8.5 MV/m) sections which boost the mean particle energy to $\sim$ 250 MeV. Each pair of sections is powered by one klystron. The sections are separated by a drift space of $\sim$ 11.5 cm ($\lambda_{rf}/2$). The parameters of the high gradient (Type ♯1) and moderate gradient (Type ♯2) sections are listed in Table 2.3.1.

For both types of accelerating cell geometries electromagnetic field maps have been calculated and used in the simulation code. Moreover, the correction of E_0T is carried out: the real accelerating gradient E_0T is estimated taking into account the beam loading for each AS according to the algorithm which is described in Paragraph 4.4.

2.4 Reference PPA design with Solenoid Focusing

In this case the PPA accelerating structure is fully embedded in a focusing solenoid. This realization is interesting because it collects some important processes and gives the basic estimation for the PPA operation.

Particle losses. In Fig. 2.4.1 the histogram of positron and electron losses in each structure element is presented with respect to the total number of positrons and electrons emerging

Table 2.3.1: Accelerating sections parameters

Section type	Type ♯1	Type ♯2
Number of sections	4	14
Number of cells per section	5	17
Accelerating gradient E_0T, MV/m	< 14.88	< 8.5
Shunt impedance Z_{sh}, MΩ/m	31.92	35.38
Transit time factor T	0.78393	0.79657
Length, m	0.5765	1.9602
Dissipated power, MW	< 4	< 4
Quality factor	∼23690	∼23580
Aperture diameter, mm	52	52

from the target. The first column is the particle losses in the AMD. About 58% of the positrons and 71% of the electrons will be lost in the AMD and first five AS resulting in an additional heating. In Table 2.4.1 the power of lost particles P_L is presented for each AS. This value is calculated as energy per second of all lost particles for the positron flux from the target providing the desired number of positrons at the IP.

Beam loading. The particle dynamics permits to estimate the beam loading effect for each AS. In Fig. 2.4.2 the time dependent energy extraction from the first six sections is shown. There is not integral consumption of energy stored in the first section due to the energy exchange of section - accelerated particles and decelerated particles - section. Mainly the accelerated particles are positrons and decelerated particles are electrons. Moreover, due to this effect, the first four high gradient sections operate with low beam loading, whereas the downstream moderate gradient sections operate with approximately constant, high integral beam loading. In Table 2.4.1 the power P_{bl}^{sol} extracted from the sections during the operation pulse (800μs) is listed.

Positron and electron acceleration. At the PPA input the positrons and electrons are overlapped in the same space. In an AS optimized for positron acceleration, the electrons are at first decelerated and then due to dephasing re-accelerated or lost. In Fig. 2.4.3 the longitudinal positron and electron phase spaces are shown at the time when the first positron bunch has completely left the pre-accelerator. The particle behaviour is evidently complicated. Due to the long tail of the positron bunch at the PPA input a part of the positrons is decelerated. Also, for the same reason, a part of the electrons is directly accelerated on the rf-wave crest shifted by 180^o from the fist positron bunch center. Moreover, the deceleration leads to the development of positron and electron bunch trains. The latter one is longer and more populated. Except the first positron bunch, the other parasitic bunches should be destroyed before further acceleration. Note, that the first positron bunch includes $\sim 94\%$ of the "survived" positrons.

In Fig. 2.4.4 some output phase space portraits for the first positron bunch are presented. In the first picture the acceptable region for the DR is marked by a rectangle.

In Table 2.4.2 the final parameters for the PPA with solenoid focusing are noted. It should be pointed out that the capture efficiency is negligibly changed within $\pm 5^o$ deviation from the optimum rf-phase.

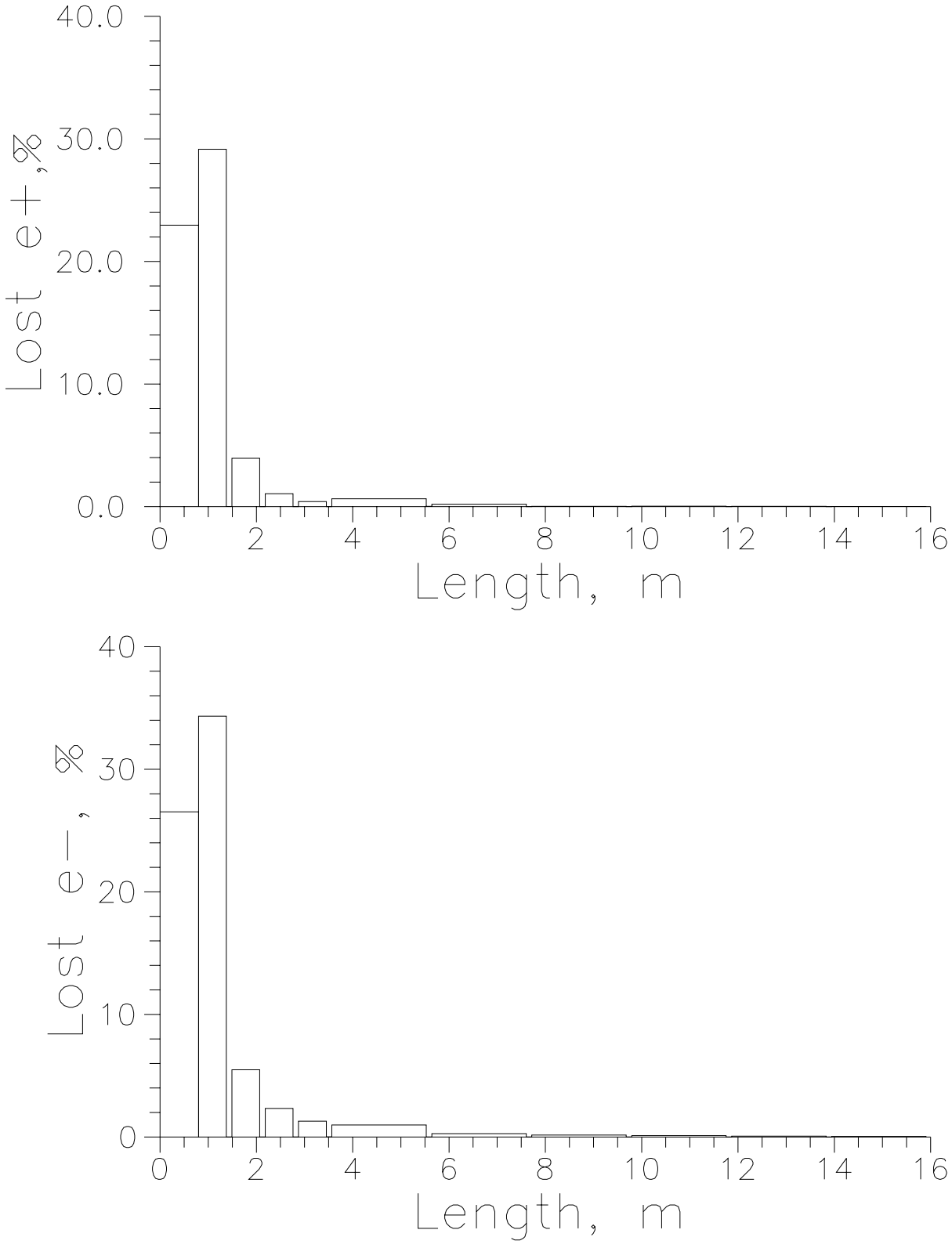

Figure 2.4.1: Particle loss distribution along the PPA.

Table 2.4.1: Accelerating section power performance.

P_L – power of lost particles for the PPA with solenoid focusing;
P_{bl}^{sol} – pulsed (800μs) beam loading power for the PPA with solenoid focusing;
P_{bl}^{sep} – pulsed (800μs) beam loading power for the PPA with collimating separator.

Section number	P_L, kW	P_{bl}^{sol}, MW	P_{bl}^{sep}, MW
1	6.250	0.0385	0.0385
2	1.031	0.3179	0.3179
3	0.385	0.4060	0.4060
4	0.124	0.4485	0.4485
5	0.284	0.9187	0.9187
6	0.048	0.9598	0.9598
7	0.0049	0.9666	0.9666
8	0.0009	0.9726	0.9726
9	0.0007	0.9730	0.4723
10	0.0003	0.9750	0.4721
11	0.0004	0.9761	0.4720
12	0.0002	0.9758	0.4719
13	0.0196	0.9756	0.4718
14	0.0043	0.9760	0.4717
15	0.0214	0.9763	0.4716
16	0.0100	0.9755	0.4715
17	0.0002	0.9741	0.4714
18	0.0001	0.9638	0.4713

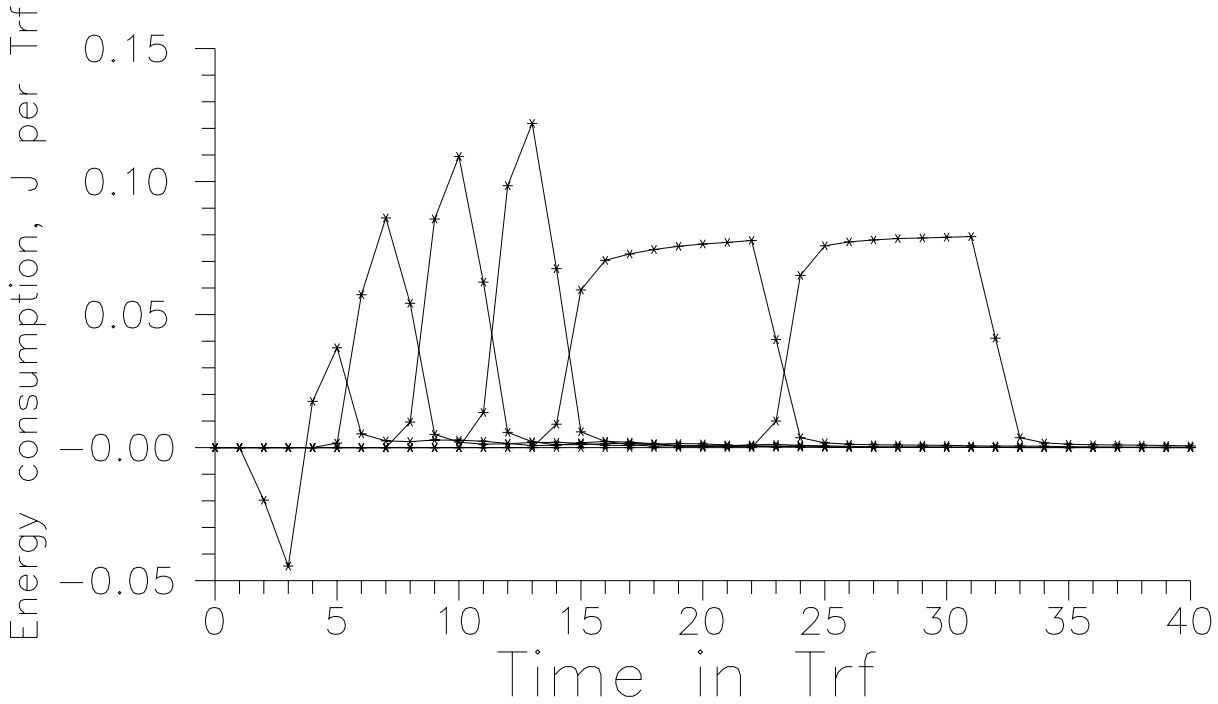

Figure 2.4.2. Time dependent energy extraction from the first six AS.

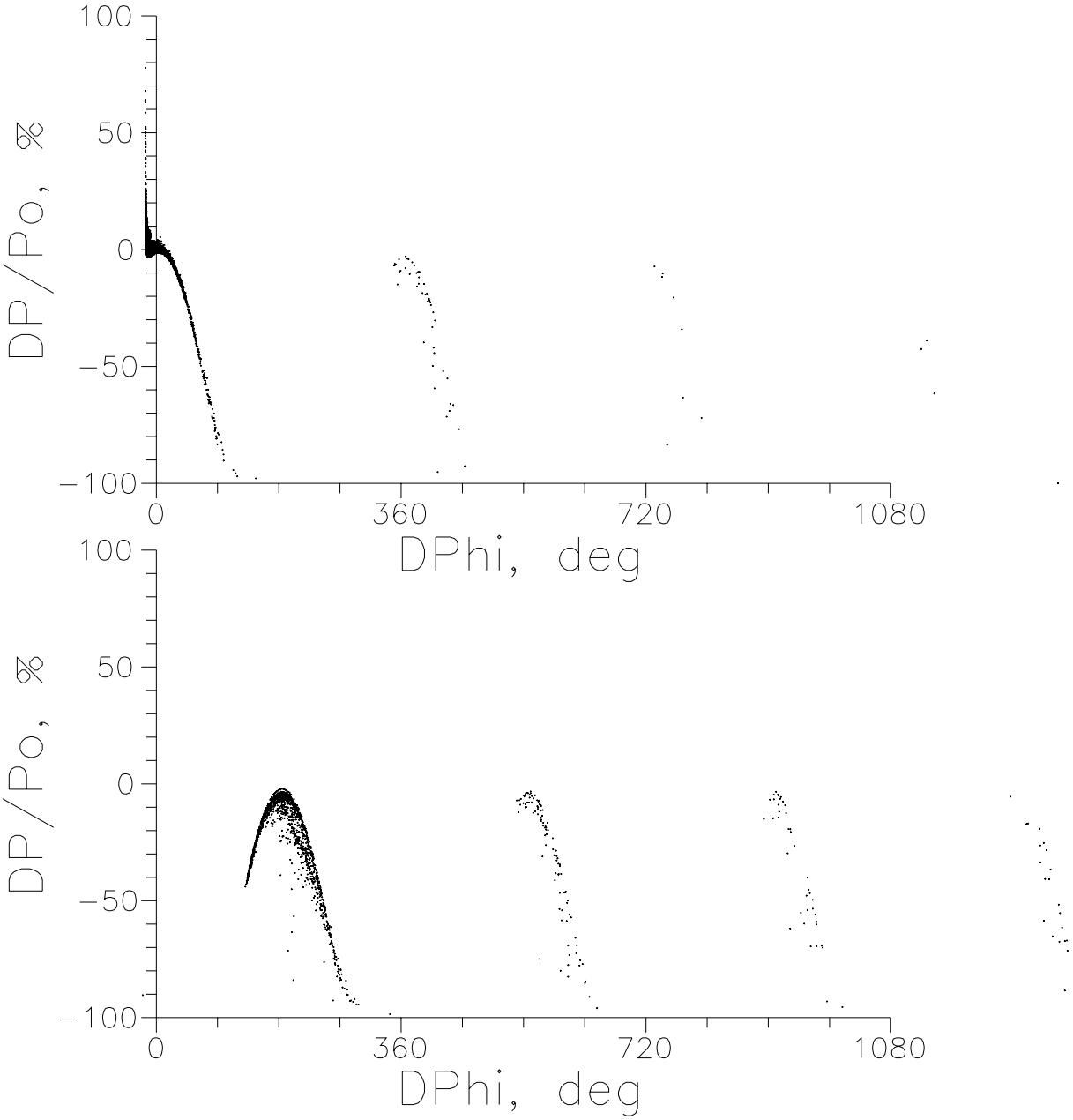

Figure 2.4.3. Longitudinal phase space of positrons (top) and electrons (bottom) at the exit of PPA with solenoid focusing.

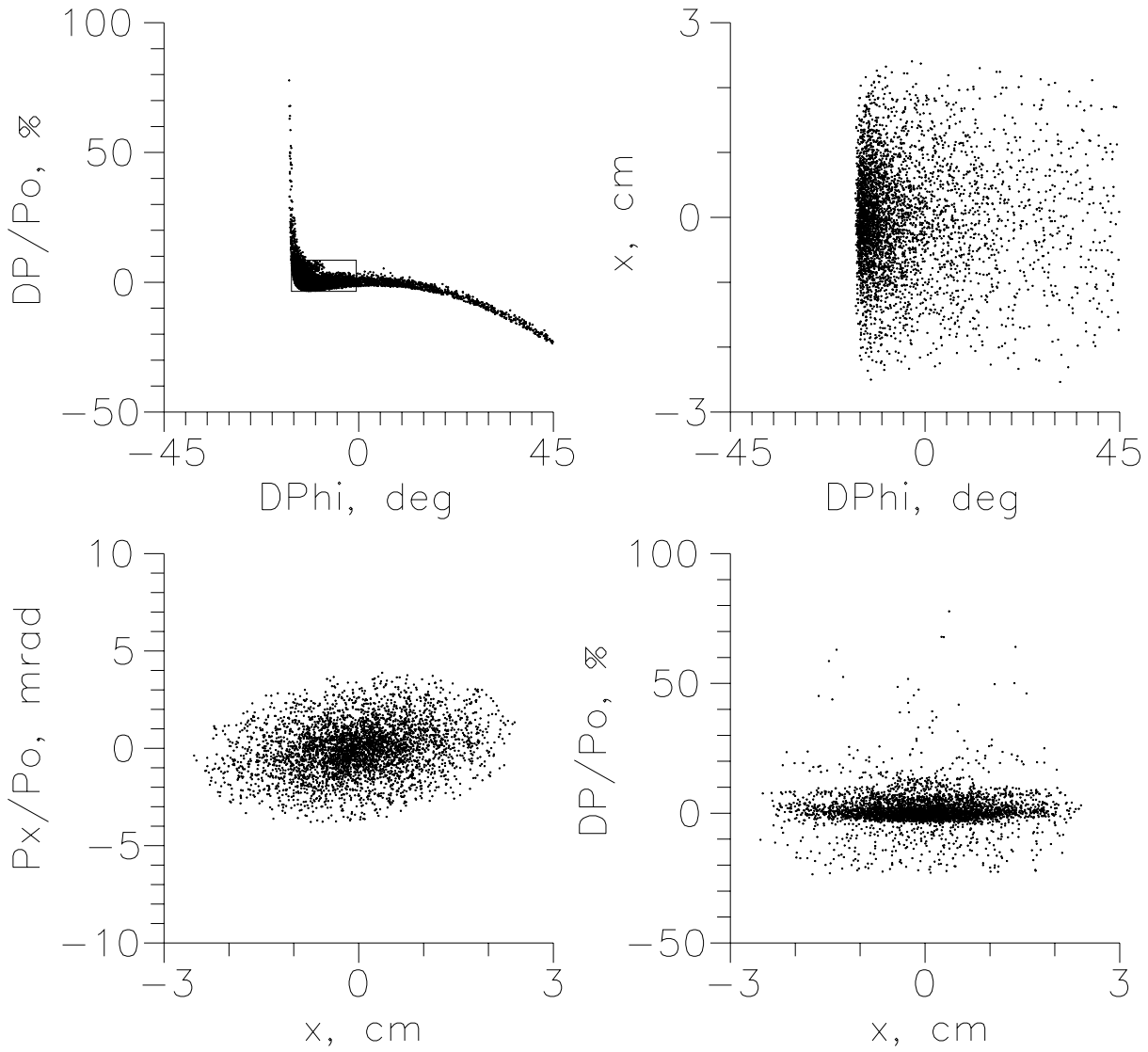

Figure 2.4.4. Phase space portraits of positrons at the exit of PPA with solenoid focusing.

2.5 Reference PPA design with Solenoid and Quadrupole Focusing

As one will see from Chapter 6, the solenoid is power consuming device. There is another way to realize the PPA focusing structure. After accelerating the beam within the focusing field of the solenoid to an energy of $\sim 100\,\mathrm{MeV}$, the divergence of the beam has been sufficiently reduced, therefore it can be focused further by means of quadrupole magnets and accelerated to $\sim 250\,\mathrm{MeV}$ or any other required energy. Following this conception we have decided to embed only the first eight AS in the solenoid and then make a transition to quadrupole focusing. Evidently a matching section will be needed. In this case the optimized central energy associated with the transition and matching system will be equal $\sim 107\,\mathrm{MeV}$ and the solenoid length will be 11 m. A simple FODO, doublet and triplet quadrupole structures can be used as candidates for focusing in the second pre-accelerator part.

FODO-structure. The focusing and defocusing quadrupoles are placed sequentially between the ASs. Because of the constant section length it is reasonable to find the periodic solution by the well known method. In Fig. 2.5.1 the calculated typical dependences are plotted. On the right side graph the phase advance per unit FODO cell is presented. It is identical for the horizontal and vertical planes because of the same strength of both quadrupoles in the cell. On the left side the dependences of the β-functions at the first AS input are plotted. It follows that at the entrance of each AS the positron beam with the required transverse emittance must have an extremely high size in x- or y-direction. That is not adequate to the aperture diameter of the ASs. The additional investigations have shown that the acceptance of the FODO periodic channel will be approximately equal to the acceptable transverse emittance of the positron beam, if the section length is reduced by a factor two (here we suppose that the accelerating structure can not be placed inside of the quadrupole aperture because of the large outer diameter of the ASs). From our point of view the technical disadvantages (twice the number of quadrupoles, the additional bridge coupling cavities) are undesirable and therefore the realization of a FODO structure becomes unattractive.

Doublet structure. This periodic structure was not studied. Apparently, taking into account the above notes, it will be possible to design the focusing channel without dividing the ASs. But the acceptance of this channel will be close to the acceptable transverse emittance of the positron beam. It means that during acceleration the focusing system will work as a filter in the transverse phase space. We suppose it will be better to separate particles by a more controllable method.

Triplet structure. In Fig. 2.5.2 the characteristic functions are plotted for the periodic solution of the triplet focusing cell. The different line types are for different transverse directions. The parameter is the strength of the central quadrupole, whereas the side quadrupoles have $k = 6.2\,\mathrm{m}^{-2}$. This particular solution is satisfying for our purpose. Any values of quadrupole strength which give a phase advance for the periodic cell less than $\sim 85^o$ in both planes (for stability) and more or less small values of the β-functions at the cell input can be used. The results have shown that for a wide region of quadrupole strength it is possible to trace the positron beam through the accelerating structure without losses. For simulation the following parameters of the triplet quadrupoles were used:

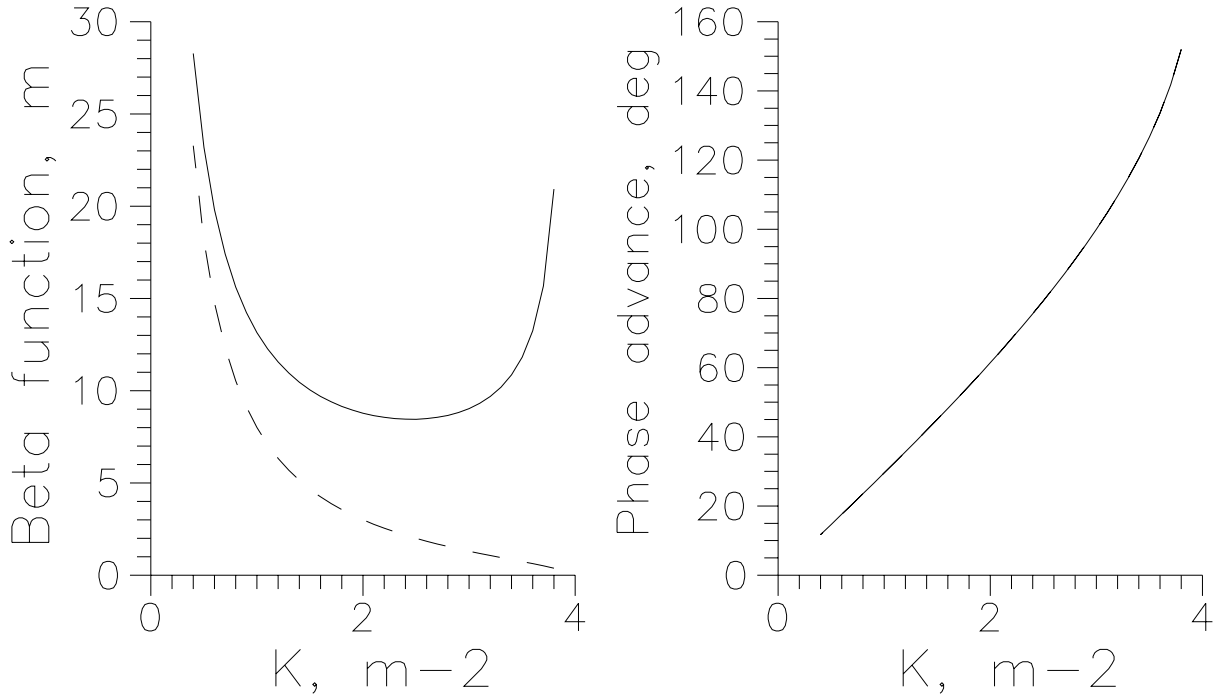

Figure 2.5.1. FODO periodic cell operation.

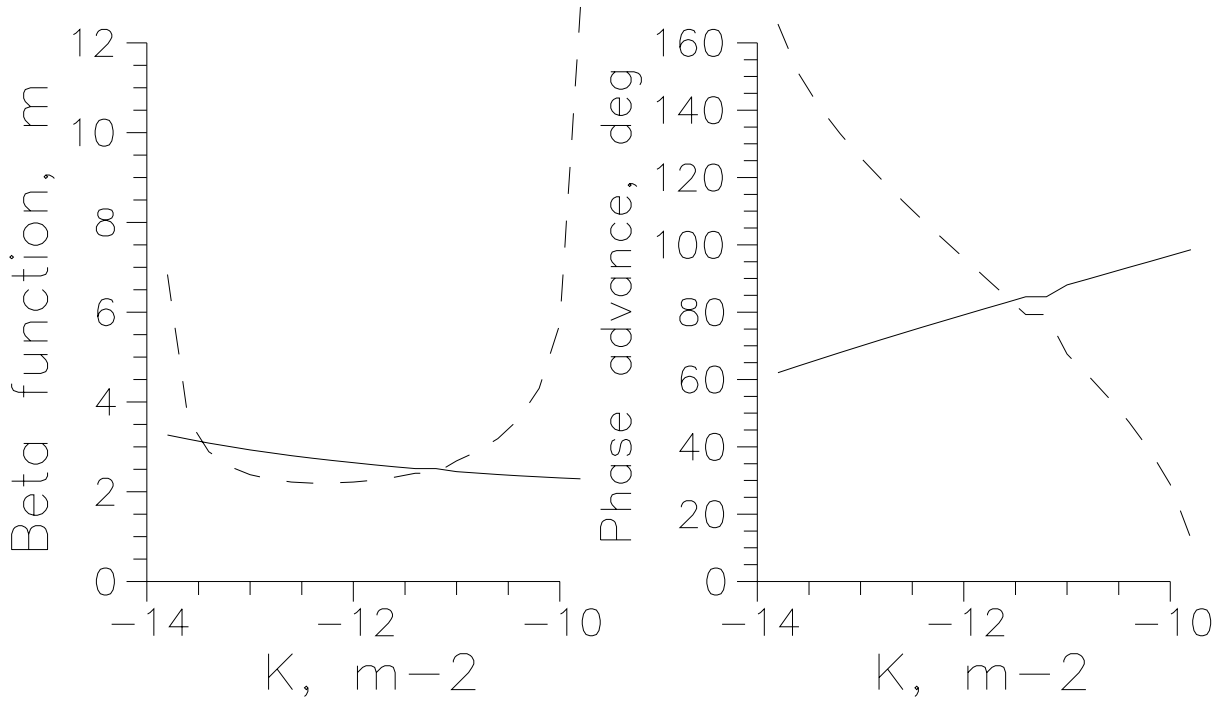

Figure 2.5.2. Triplet periodic cell operation

side quadrupole strength, m^{-2}	6.2
central quadrupole strength, m^{-2}	-11.6
quadrupole length, cm	20
quadrupole aperture diameter, cm	8
distance between quadrupoles, cm	12

For this choice the field gradient in quadrupoles does not exceed 1 kG/cm.

Matching section. For the transverse matching of the two accelerating parts with solenoid and quadrupole focusing four quadrupoles were used. Their typical parameters are:

field gradient, kG/cm	< 0.7
length, cm	25
quadrupole aperture diameter, cm	12
distance between quadrupoles, cm	18

The positron losses at the matching section are not more than 2%. They result from the envelope manipulation and consist of particles from the peripheral region of the transverse beam emittance.

In Fig. 2.5.3 the final longitudinal phase spaces for positrons and electrons are shown for the PPA with combined transverse focusing. Compared with Fig. 2.4.3 it is evident that the number of parasitic positrons and electrons is reduced. This is due to the mismatching of dynamic parameters of the parasitic particles with the triplet periodic focusing. More than 93% of the "survived" positrons are in the first bunch. Approximately 5% of particles emerged from the target are uniformly lost along the second part of the pre-accelerator.

Some phase space pictures of the output positron beam are presented in Fig. 2.5.4. The characteristic parameters of the PPA with combined focusing and parameters of the acceptable positron beam are collected in Table 2.4.2. The reduction of the capture efficiency is the result of longitudinal dephasing in the matching section.

2.6 Particle separation

All parasitic particles and photons used for positron production must be separated before further acceleration. It can be done by using a series of bending magnets. However it has to be done without losing the quality of positron beam and without significant reduction of the capture efficiency. The separation can take place behind the PPA. But, may be, it will be better from the operation and beam diagnostics point of view to separate as soon as possible. Below we will consider a separator which is placed between the two parts of the PPA discussed in the previous paragraph.

Because of the specific peculiarities of the LINCIC code, the particle tracking in the separator was carried out by using the first order matrix formalism.

We also propose to place two matching sections, one before and one behind the separator. The section parameters are the same as presented above.

The required characteristics of the magnet system are:

- The entire magnet system has to shift the original axis of a beam to a parallel line displaced from its original location by a distance $1.0 \div 1.2$ m.
- In order to prevent the beam blow up at the exit due to energy dispersion, the system must be at least in first order achromatic as an entire system, but at the same time it must have a relatively large dispersion of the beam at some intermediate locations inside the separator, where collimators can be inserted.
- The transverse dimensions of the beam must not be too large at any point within the

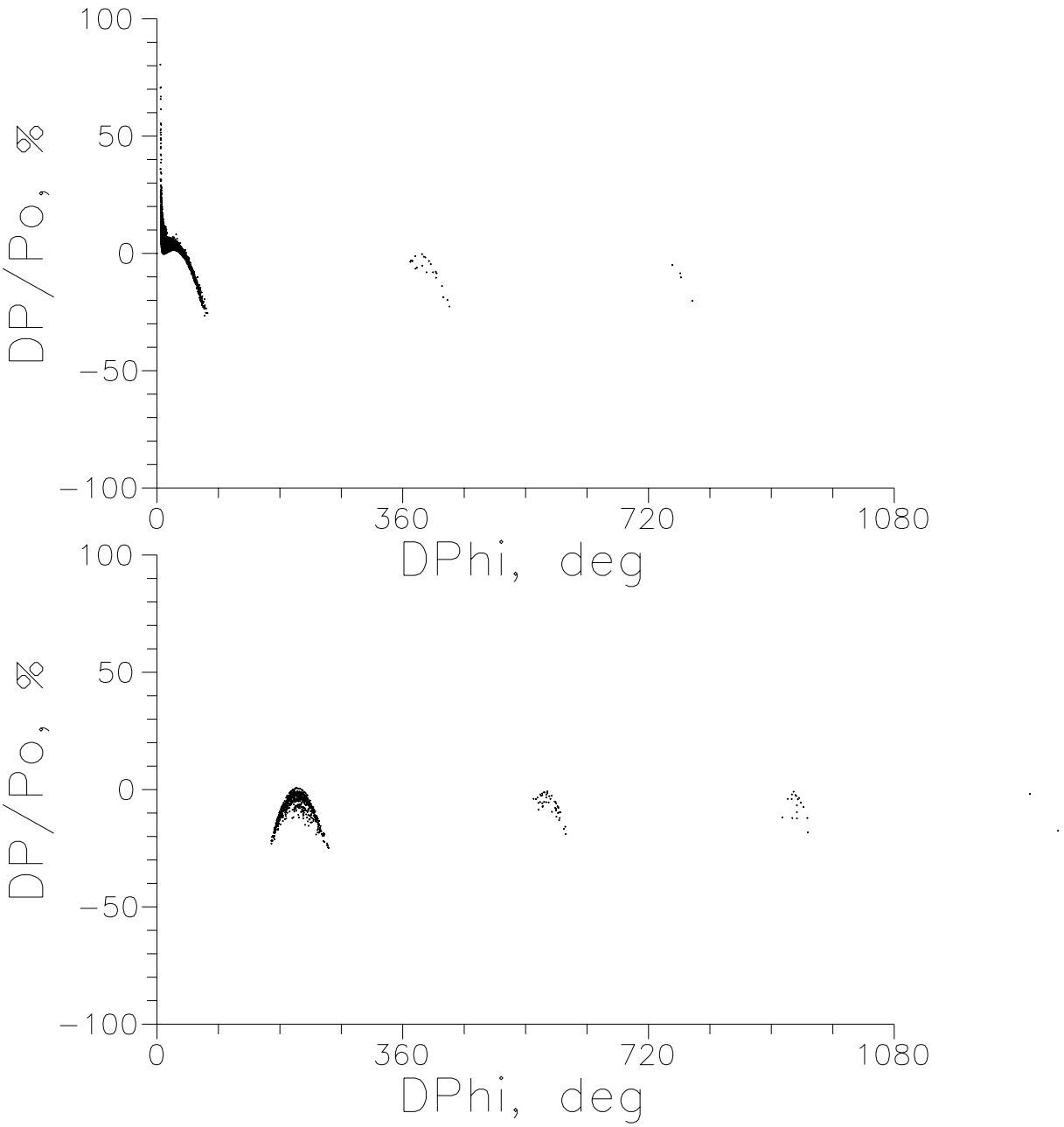

Figure 2.5.3. Longitudinal phase space of positrons (top) and electrons (bottom) at the exit of PPA with combined focusing.

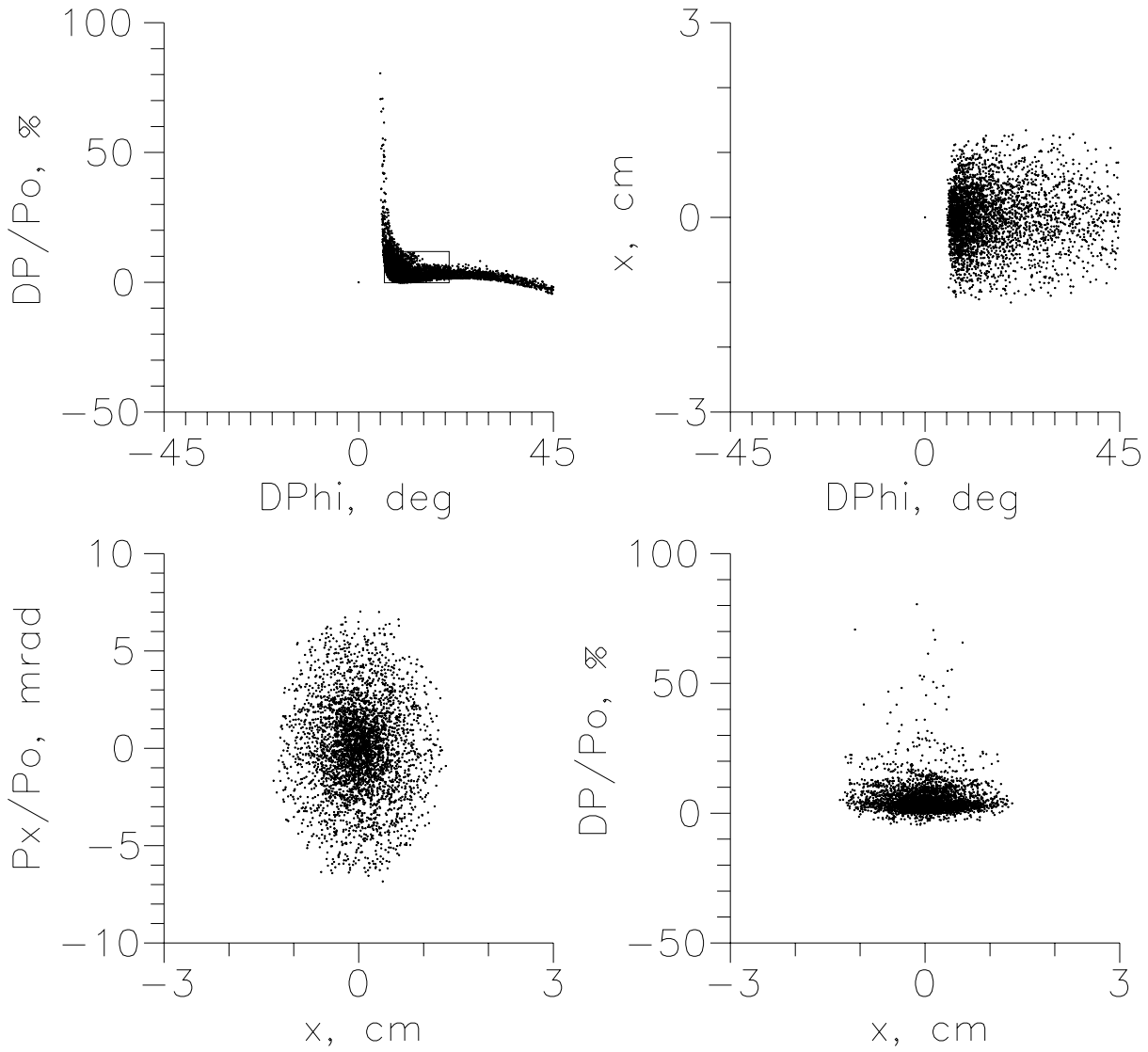

Figure 2.5.4. Phase space portraits of positrons at the exit of PPA with combined focusing.

transport system. Together with the chosen physical aperture of quadrupole lenses (< 0.2 m) it imposes the limitations on the behaviour of the betatron functions inside the separator.
- It is important also to keep track of the flight times through the system. Since two particles that take different paths through the magnet system do in general not travel the same distance, an unwanted expansion of the beam resulting in additional particles losses might happen. So it is desirable to make the separator to be an isochronous system or a system with small negative (due to longitudinal asymmetry of the beam at the entrance) value of the path length difference from that of the reference particle.
To satisfy the above mentioned constraints on the linear level we have developed a separator which contains quadrupoles and bending magnets. The complete magnet system is composed of four 90^o (or multiple of 90^o) cells, which are only differed by the sign of the magnetic field in the bending magnets. The linear phase space transformation corresponding to such a system automatically will be achromatic and will transport the beam with no change in properties with respect to the transverse coordinates [5]. Although in theory this four-cell separator can not be made completely isochronous [6], the bunch lengthening coefficient can be easily fitted to a small negative value. This fit was done finally by numerical optimization, taking also into account in the objective function the required limitations for betatron functions and dispersion. The linear transformation describing the transverse dynamics is equal to the identity matrix, and hence the transverse dimensions of the beam are left unchanged after passing this magnet system.
The technical parameters of the separator elements are as follows:

Dipole:	total number	4
(sector magnet)	bend angle	$\pi/20$
	central energy, MeV	107
	magnetic field, T	1.1307
	central trajectory, m	0.5
Quadrupole:	total number	16
	length, cm	40
	aperture diameter, cm	12 and 15
	field gradient, kG/cm	< 0.25

The distance between the separator elements was chosen to be 30 cm.
Finally the separator and the two matching sections have a length of ~ 17.75 m in projection on the linac axis and effect the parallel translation of the beam from its original axis by the distance ~ 1.13 m (note that this distance can be easily fitted within the range ± 0.2 m by small changes of the quadrupole and dipole magnetic fields as well as with small changes of the quadrupole fields the sector bending magnets used in this design can be easily replaced by rectangular bending magnets).
The scheme proposed is enough flexible and allows to obtain different options. For example, the options with α-functions equal to zero at the separator end may be obtained allowing to exclude at least the input matching. The lengthening coefficient value -0.044 looks now as the reasonable limit for the presented design. Further improvements to ≈ -0.01 are possible by using other high-field focusing elements instead of quadrupole lenses but this option needs more development.

In Fig. 2.6.1 the β-functions and dispersion for the total insertion (matching section - separator - matching section) are shown. According to the separator requirements the lengthening coefficient was set at -0.044.
The separation of the photons and electrons takes place in the first bending magnet. Here

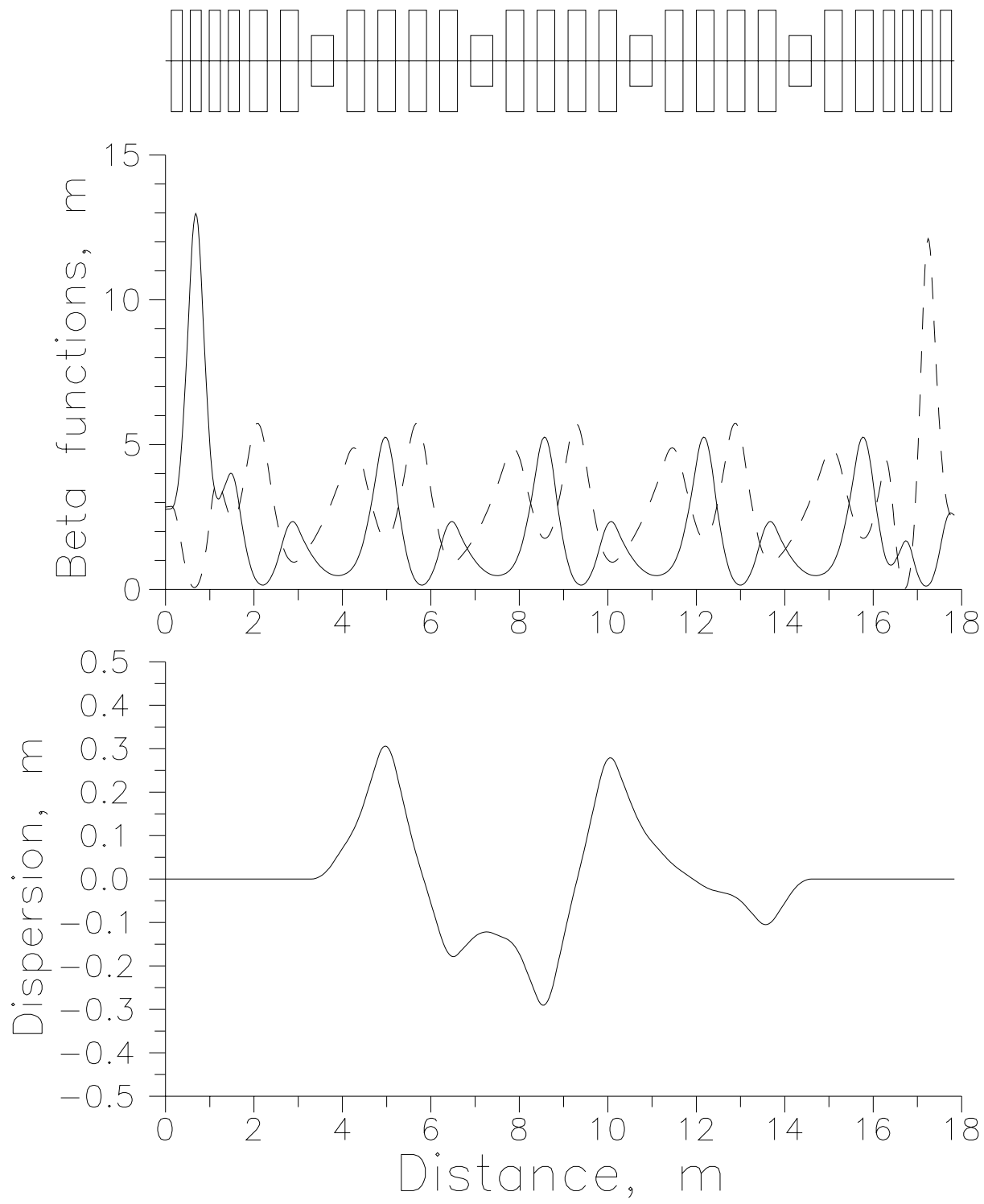

Figure 2.6.1. Separator structure functions.

the dump system has to be foreseen with the handling electron losses power capability $(14 \div 20)$kW. The main part of the parasitic positrons can be absorbed in the separator at the points defined from the behaviour of separator structure functions. The fact that the transverse phase advance in both planes for positron crossing the separator is close to 2π permits to carry out the transverse collimation efficiently. The energy collimation can be done by standard method on the part of the separator with non-zero dispersion. For example in Fig. 2.6.2 the beam envelopes collimated in both transverse planes are shown. The absorbers have a rectangular central hole and were installed just behind the first, second and third bending magnets. The dashed lines are the double rms envelopes. In Fig. 2.6.3 the envelopes for a beam emittance containing 90% of the positrons behind the separator are plotted along the second part of the PPA.

In Fig. 2.6.4 the longitudinal phase space distribution for the positron beam is presented at the output of the pre-accelerator. Compared to Fig. 2.4.3 and Fig. 2.5.3 the amount of positrons in the parasitic bunches is significantly reduced. The first bunch contains 99.5% of the "survived" particles. The total energy and phase spreads for the first bunch are $\sim 30\%$ and $\sim 50^o$ respectively. Apparently, a better cleaning can be done by a detailed study of the particle dynamics in the separator. The additional transverse phase space collimation can be qualitatively carried out in the transport line placed behind the PPA.

Some phase space pictures of the positron beam are presented in Fig. 2.6.5. The reduced number of positrons and the absence of electrons lead to a reduced beam loading for the ASs in the second part of pre-accelerator resulting in a higher optimized energy of the output beam. The pulsed beam loading power P_{bl}^{sep} for the PPA with collimating separator is listed in the last column of Table 2.4.1 whereas the other parameters are collected in Table 2.4.2.

In Fig. 2.6.6 the dependence of the capture efficiency as well as the optimized average beam energy at PPA exit with respect to the rf-phase in the second part of pre-accelerator is plotted. It can be concluded the capture efficiency is stable within a wide rf-phase range. And also the central energy associated with the output positron beam is well defined.

In addition, the study of the PPA with collimating separator has been done with increased solenoid field B= 0.32 T in the first part. The other parameters were kept the same as for the PPA with B= 0.24 T discussed above. Comparing these realizations it should be pointed out that the growth of the capture efficiency from 22.4% up to 23.5% goes ahead with a reduction of the final energy from 264.9 MeV to 262.4 MeV. Insignificant changes of the acceptable output beam parameters with respect to the essential growth of the solenoid power feed (~ 1.8 times) mean that this variant can be considered as hypothetical.

2.7 The beam dynamics summary. Final PPA proposal.

The simulation study of the particle dynamics in the pre-accelerator of a positron source for the TESLA Linear Collider permits to formulate the purposes and operation peculiarities for different parts of the pre-accelerator:

- Due to an excessive 6-dimensional phase space volume of the incoming beam with respect to the PPA acceptance the optimum operation phase space point has to be defined. It is especially important for the longitudinal phase space to populate as much as possible of the positrons in the acceptable phase space region. The deviations from the optimum don't change the PPA capture efficiency significantly. It means that the particle acceleration is well determined.
- At the beginning a solenoid transverse focusing has to be applied to have the appropriate

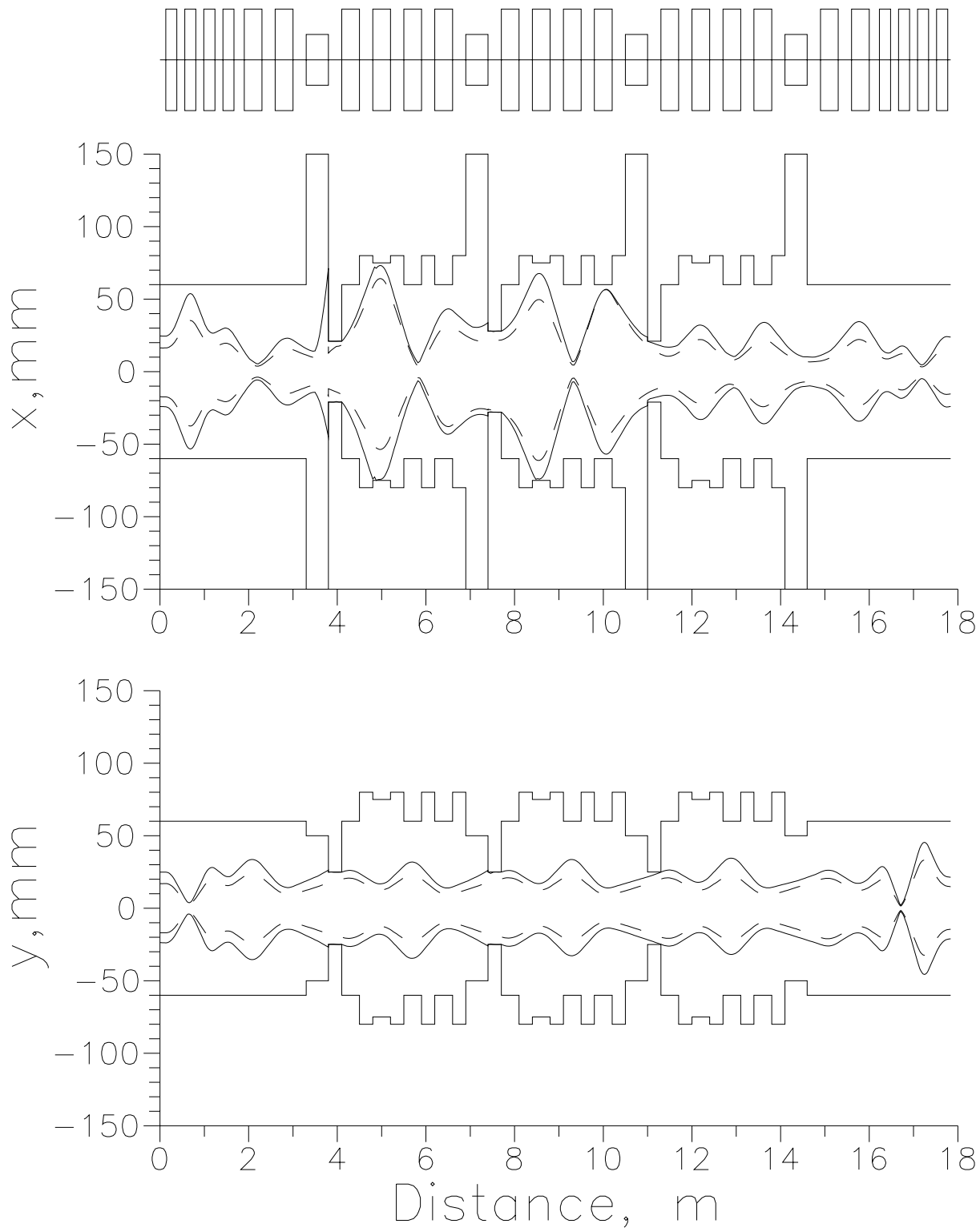

Figure 2.6.2. Collimated beam envelopes along an insertion section.

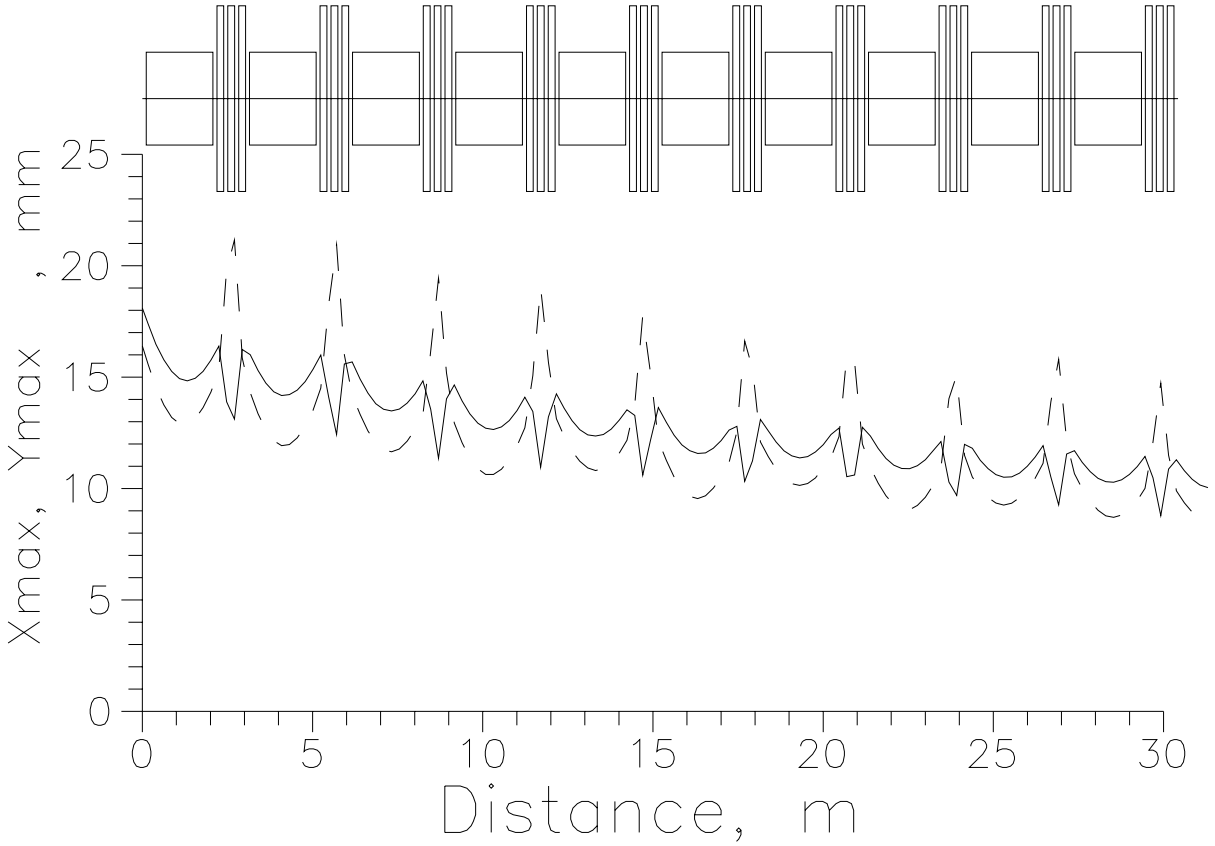

Figure 2.6.3. Beam envelopes containing 90% of positrons along the second PPA part.

Table 2.4.2: Final results.

Parameter	PPA with solenoid focusing	PPA with combined focusing	PPA with collimating separator
Final energy W_f, MeV	252.8	254.4	264.9
Longitudinal capture efficiency, % (for $\Delta W/W_f = \pm 6\%$; $\Delta\varphi = \pm 7.5^o$)	26.7	26.1	24.4
Total capture efficiency, % (for $\varepsilon_x = \varepsilon_y = 0.024$ m)	24.1	23.5	22.4
AMD length, m	0.8	0.8	0.8
Solenoid length, m	~32	~11	~11
Solenoid field, T	0.24	0.24	0.24
Number of quadrupoles	-	44	64
Number of dipoles	-	-	4
Number of klystrons	9	9	9
Total length, m	~33	~43	~59

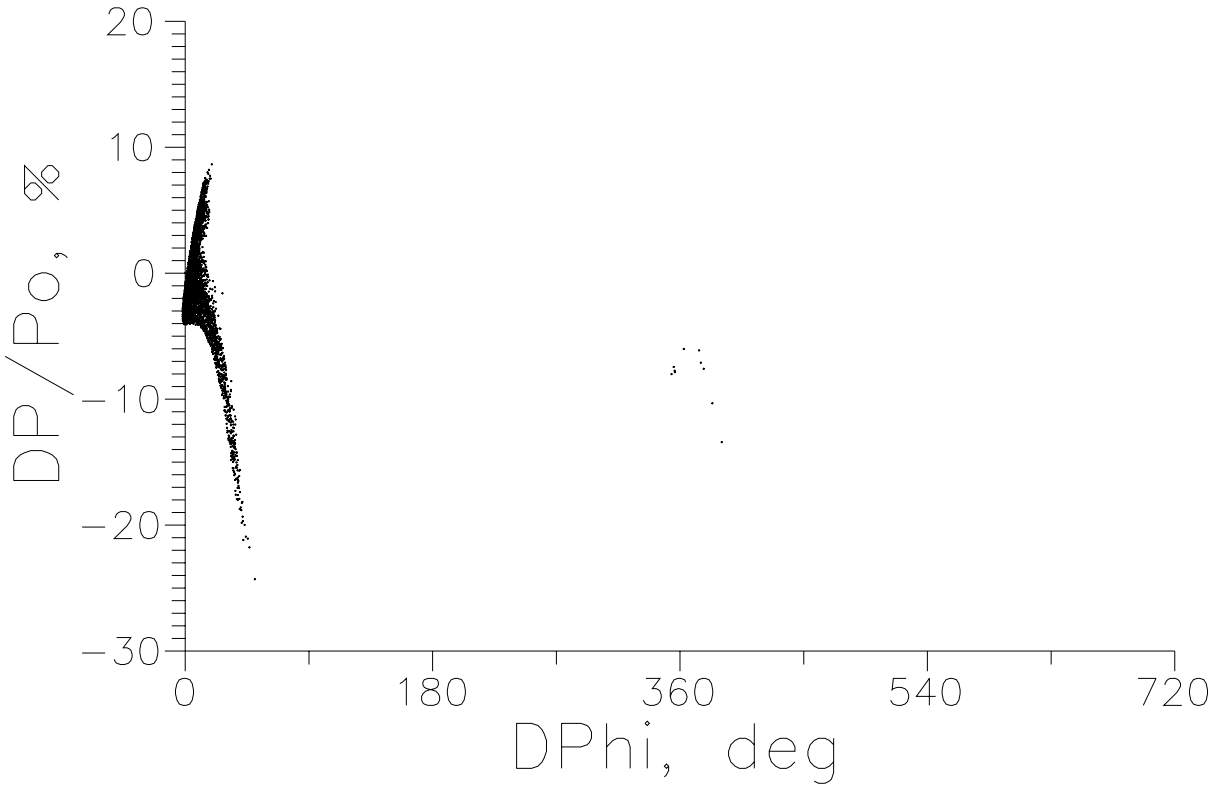

Figure 2.6.4. Longitudinal phase space of positrons at the exit of PPA with collimating separator.

capture of positrons with high enough ratio of transverse and longitudinal momentum.
- In the first accelerating cavities embedded in a uniform solenoid field, where the positron energy growth is at least $\sim 30 \div 40$ MeV, the final emittance and the efficiency of the positron source are mainly defined. Here, to reduce the longitudinal phase space dilution, the accelerating gradient has to be as high as possible. Also the main particle losses are taken place in this part. Moreover the differently charged particles are separated in longitudinal direction resulting in a reduced beam loading of the first accelerating cavities.
- Further all kinds of charged particle are accelerated and, therefore, the energy extracted from the ASs is maximal. This accelerating part has to be adjusted for reliable operation with technically reasonable parameters. The using of moderate gradient ASs with small number of feeding klystrons is a suitable decision for the second accelerating part of PPA.
- The transverse acceptance of the PPA depends on the solenoid field and the aperture radius of the accelerating structure. The choice of these parameters is determined from the technical possibilities and has to result in the PPA acceptance larger than the desired positron beam emittance.
- The pre-accelerator with only solenoid transverse focusing up to an energy > 150 MeV is power consuming device. Therefore, after the beam acceleration within the focusing field of the solenoid to an energy of ~ 100 MeV, where the divergence of the beam has been sufficiently reduced, it is reasonable to apply quadrupole triplets for periodic transverse focusing.
- To relieve the operation of cavities in a low gradient accelerating part the particle separator can be installed. All foreign particles must be dumped in it. The separation can be done by using a series of bending magnets and quadrupoles when the positron beam energy will

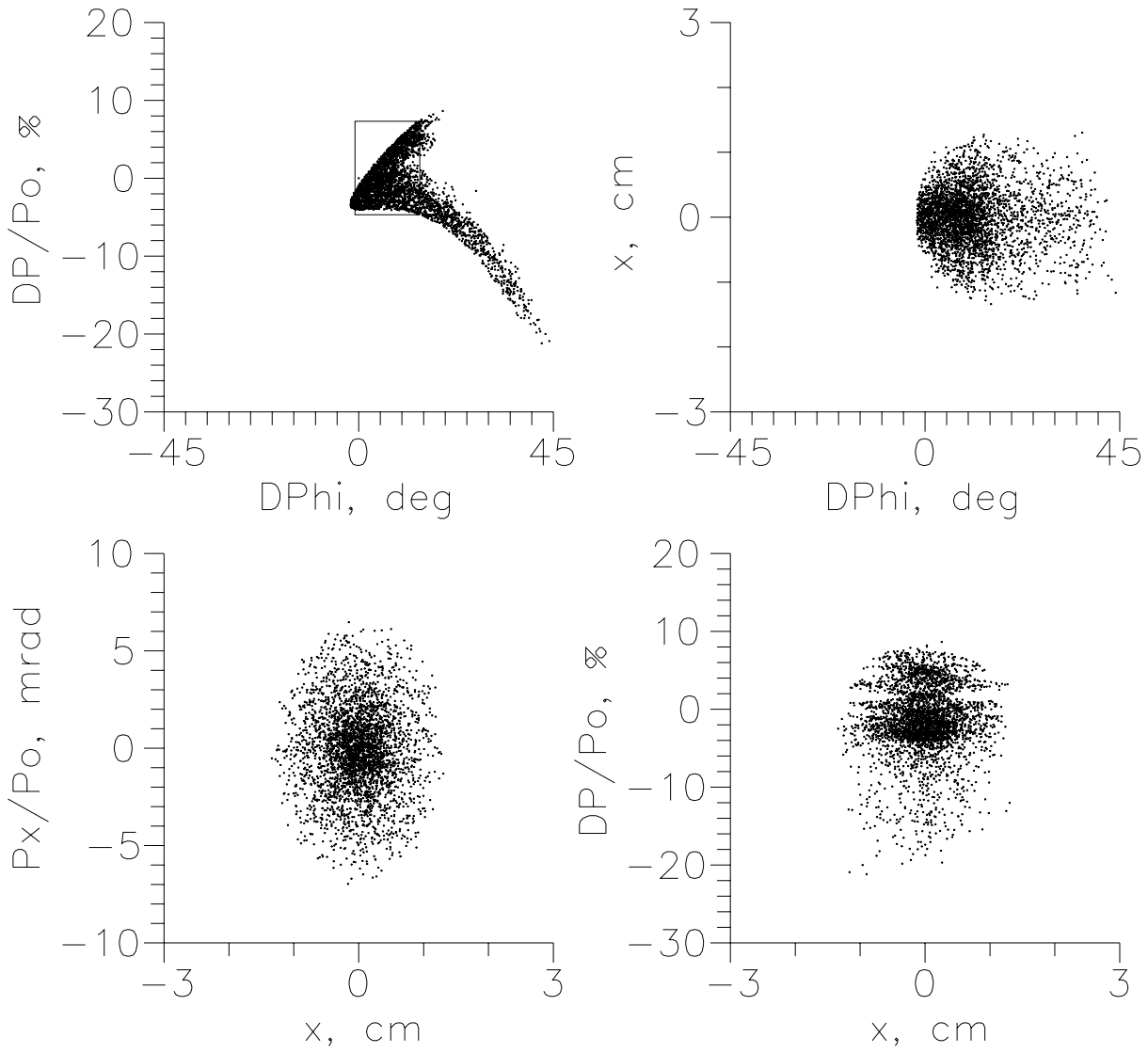

Figure 2.6.5. Phase space portraits of positrons at the exit of PPA with collimating separator.

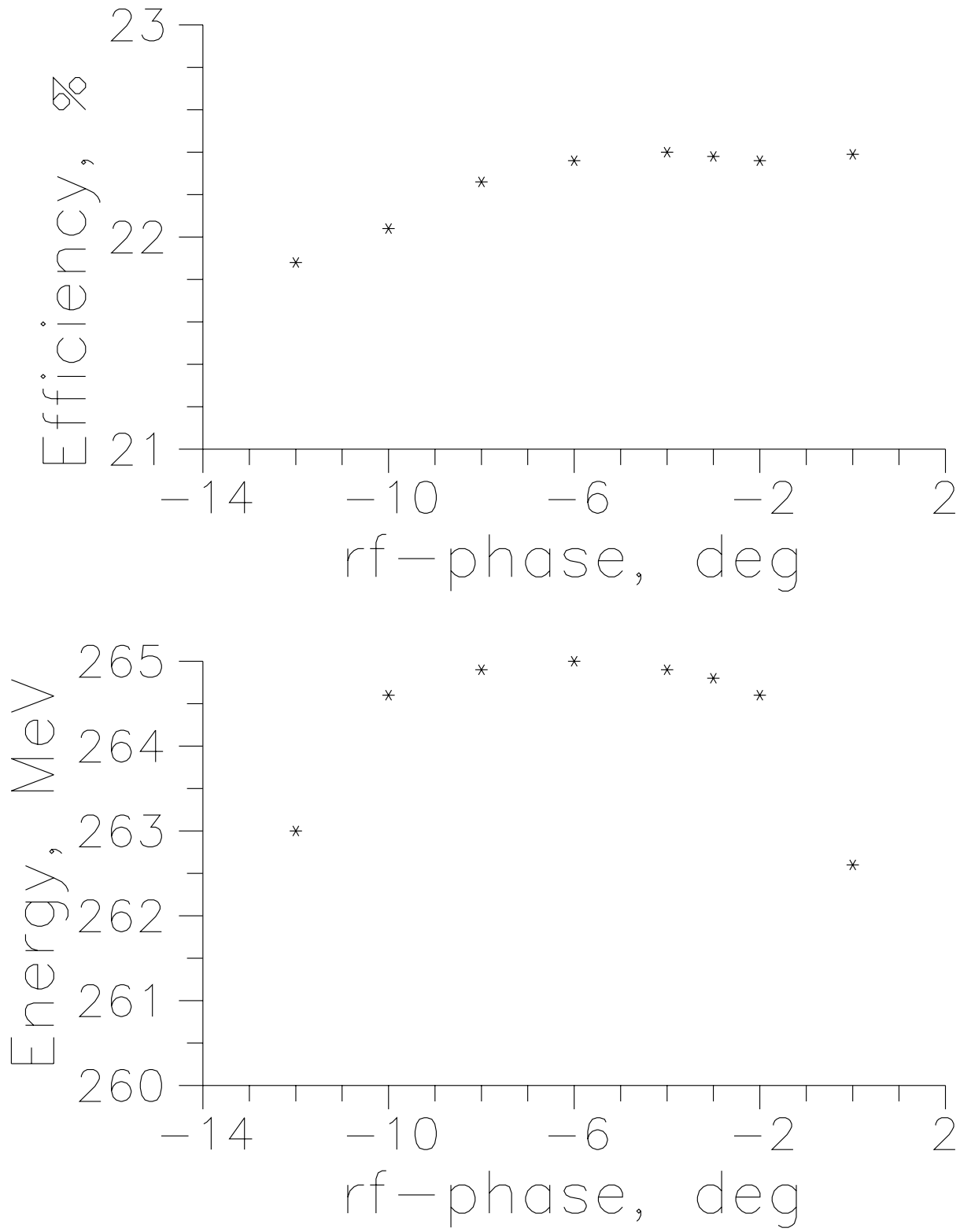

Figure 2.6.6. Capture efficiency and average beam energy vs rf-phase in the second PPA part.

be more than $\sim$ 100 MeV. Evidently it will be reasonable to combine the separator and transition between the parts with solenoid and quadrupole transverse focusing. Moreover there are other productive separator functions: at first, it is possible to translate the beam axis; then, the effective energy separation for positrons can be done by using the dispersion properties of the separator magnet structure; adjusting the transport lengthening coefficient for separator slightly less than zero with respect to the energy deviation from the optimum value, a bunching can be performed; and, at last, together with the following periodic triplet focusing the transverse phase space collimation can be carried out to get the desired output positron beam emittance.

The final PPA proposal is recommended as follows (see Fig. 8.1 for comments):

- A standing wave accelerating structure with optimized rf-parameters is used for acceleration.
- 4 accelerating sections with high gradient and 5 cells per section followed by 14 accelerating sections with moderate gradient and 17 cells per section compose the pre-accelerator up to an energy more than 250 MeV.
- The accelerating structure is divided in two parts containing 8 and 10 accelerating sections, respectively.
- The transverse focusing by a solenoid with field of 0.24 T and length of 11 m in the first part is followed by a periodic transverse focusing with triplets in the second part.
- An insertion (matching section - separator - matching section) is placed between the accelerating parts.

The simulation results of the particle dynamics for the proposed preaccelerator have shown:

- A pure positron beam with energy > 260 MeV and capture efficiency $> 22\%$ can be produced at the pre-accelerator output.
- The capture efficiency and central output beam energy are negligibly changed within at least $\pm 5^o$ deviation from the optimum rf-phase. It is possible to realize the effective energy and transverse phase space collimation using the separator properties and periodicity of the second PPA part.

Further studies of the particle dynamics in the PPA are needed to explore possible improvements in the capture efficiency. At first the careful particle tracking in the separator has to be done. The separator possibilities have to be carefully studied.

Additional complex investigations are also required to understand and to optimize the beam dynamics at any element during the acceleration from the target to the injection into the Damping Ring.

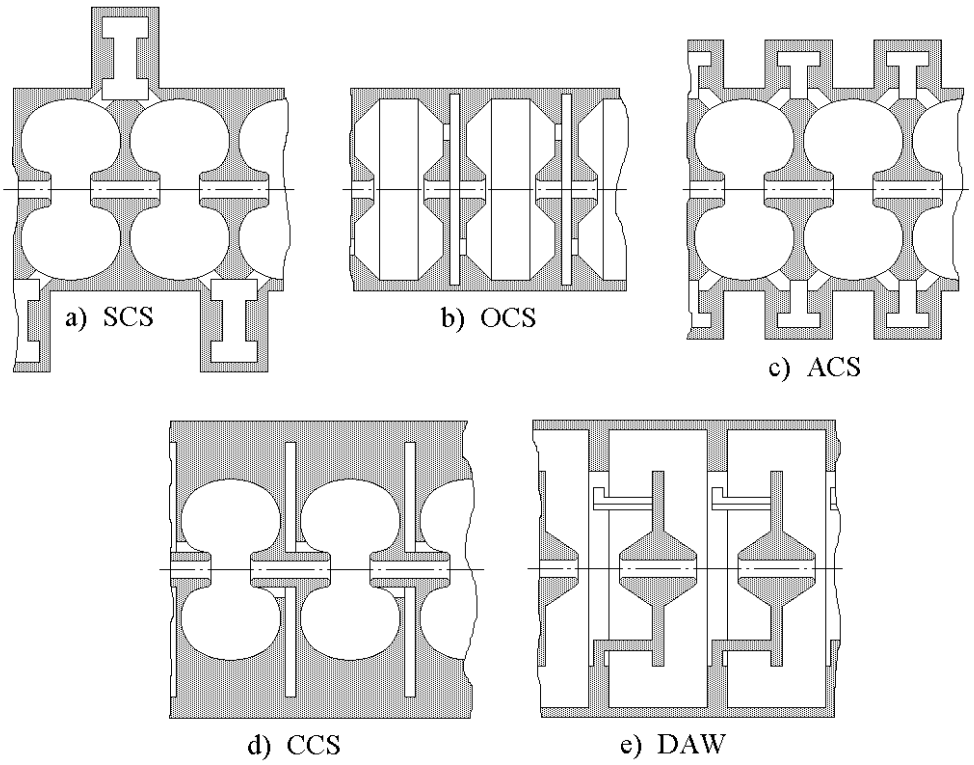

Figure 3.1.1: Standing wave coupled cells accelerating structures.

3 Accelerating Structure

3.1 Particularities of an accelerating structure. Special requirements

For L-band operation $f_0 = 1300 MHz$ both Standing Wave (SW) Coupled Cells (CC) structures and Traveling Wave (TW) structures may be used. For present-time review of SW structures see [7].

In particle accelerators Side Coupled Structure (SCS), On-axis Coupled Structure (OCS), Annular Coupled Structure (ACS), Co-axial Coupled Structure (CCS) and Disk and Washer (DAW) structures are known. These structures achieve practically the same values of effective shunt impedance Z_e and coupling coefficient $k_c \approx 5\%$ (except DAW $k_c \approx 40\%$) but differ in the design (see Fig. 3.1.1).

The line of the SW CC structures may be continued with the new INR development: Cut Disk Structure (CDS) [8], which looks similar to OCS but realize a different idea in the design of the coupling cell, resulting in $k_c \approx 20\%$ without drop of Z_e. CDS rf properties were tested in cold model measurements, confirming the idea and design parameters of this structure [19].

For TW operation mode Disk Loaded Waveguide (DLW) with different cell shape (Fig. 3.1.2) are widely use (see, for example [9]).

Together with the usual requirements of high efficiency etc., the accelerating structure for the PPA has additional restrictions.

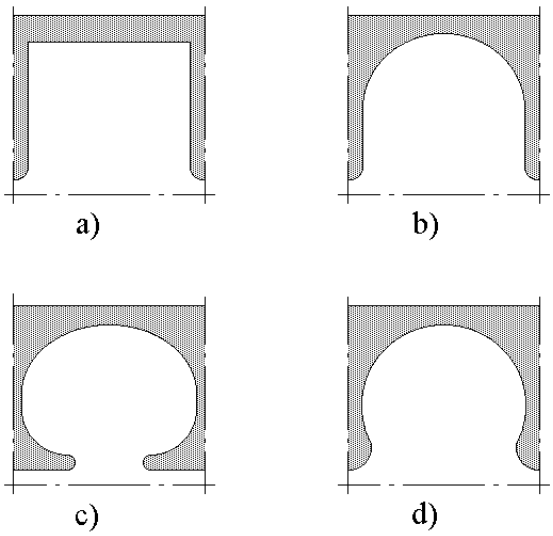

Figure 3.1.2: Different shapes of the DLW cells.

Accelerating Sections (AS) in the first part of the PPA should be placed inside solenoid, the structure should have a small outer diameter. This restrict our further consideration for SW OCS and CDS structures, or TW DLW one.
In the longitudinal magnetic field of the solenoid e^+ and e^- move along spiral trajectories with the frequency of rotation f_{rot}:

$$f_{rot} = \frac{Bc^2}{2\pi W_e}, \tag{1}$$

where B is the inductance of the magnetic field, c is the speed of light, and W_e is the energy of particles. For $B = 0.24T, W_e(3 \div 100)MeV$ this corresponds to wide range $f_{rot} \approx (33 \div 700)$ MHz. To avoid parasitic interaction of the beam, the structure should have no modes in this frequency range. The operating mode with a frequency $f_0 = 1300.0$ MHz should be the fundamental mode of the structure. This excludes such structures with small outer diameter as cross-bar structures [11].
The consideration above shows SW OCS, CDS or TW DLW as possible candidates for the PPA application.
An important parameter of the structure is the maximum surface electric field E_{smax}. Usually this value is described in units of the Kilparrck limit $E_k = 32.1MV/m$ for $f_0 = 1300MHz$. In present proton linac design [12] and in operating linacs [13] with frequency $800 \div 1000MHz$ usually $E_{smax} = (1.3 \div 1.8)E_k$. The best results shows an S-band TW DLW section [14] with stable operation at $E_{smax} \approx 2E_k$.
Taking into account that:
- the total e^-, e^+ losses in the first PPA sections are high;
- the PPA rf pulse is long enough ($800\mu s$);
- the PPA is a multi-gap accelerator (total ≈ 255 accelerating gaps);

- the sparking rate rises fast and nonlinear with increasing E_{smax};
- the possible improvement in the shunt impedance rises slow with increasing E_{smax},
we limit for PPA design to $E_{smax} = 40MV/m = 1.29E_k$ - a rather conservative value.

3.2 TW or SW operating mode

Today L-band linacs both in TW (8 units according to [10]) and in SW (4 units) operating modes are known. The choice between SW or TW mode should be done considering the complete set of linac particularities.
Extensive cell dimensions optimization both for Disk Loaded Waveguide (DLW) in $2\pi/3$ mode and for Coupled Cells (CC) structures have been performed at the operating frequency $1300MHz$ (see Appendix A).
In the design of a TW accelerating structure with DLW the choice of the total attenuation α_t per section is of primary importance. It defines the rf efficiency of the accelerating sections, because the input rf power P_{inp} should be distributed between total rf power losses in the section P_s and rf power losses in rf load P_{load}.

$$P_s \approx P_{inp}(1 - e^{-2\alpha_t}), \qquad P_{load} = P_{inp} - P_{st} \approx P_{inp}e^{-2\alpha_t}. \tag{2}$$

The attenuation per unit length α is related to other DLW parameters:

$$\alpha = \frac{\pi f_0}{Qc\beta_g}, \qquad \alpha_t = \int_0^L \alpha dz, \tag{3}$$

where Q is the quality factor of the DLW cell, β_g is the DLW relative group velocity and L is the the length of the section.
To work as constant gradient structure, β_g should change along the DLW section [11] as:

$$c\beta_g = \frac{2\pi f_0 L(1 - (1 - e^{-2\alpha_t})z/L)}{Q(1 - e^{-2\alpha_t})}. \tag{4}$$

In order to reach accelerating gradient E_0T, one should provide an rf power flux P_t according to:

$$P_{tw} = \frac{c\beta_g Q(E_0T)^2}{2\pi f_0 Z_e}. \tag{5}$$

Combining (4) and (5), for the beginning of the TW section ($z = 0, P_{inp} = P_{tw}$) we have:

$$P_{inp} = P_{tw} = \frac{L(E_0T)^2}{Z_e(1 - e^{-2\alpha_t})}. \tag{6}$$

It is the same expression as for SW structures, differing only by the multiplier $(1 - e^{-2\alpha_t})^{-1}$:

$$P^{sw}_{inp} = \frac{L(E_0T)^2}{Z^{sw}_e}, \qquad P^{tw}_{inp} = \frac{L(E_0T)^2}{Z^{tw}_e(1 - e^{-2\alpha_t})}. \tag{7}$$

To have a similar rf efficiency, TW and SW structures should have $Z^{sw}_e \approx Z^{tw}_e(1 - e^{-2\alpha_t})$. Results of the optimization for DLW and CC cells (see Appendix A) show $Z^{sw}_e \leq Z^{tw}_e \leq 1.05Z^{sw}_e$. To have $(1 - e^{-2\alpha_t}) \approx 1$, $e^{-2\alpha_t} \ll 1$ one need $\alpha_t \geq 1$. In this case we have very small β_g values in the end of the TW section (see (4), Table A in Appendix A). It will provide strong problems both with the section tuning and with the parameter stability

during operation.
For constant gradient DLW in S-band the usual value $\alpha_t \sim 0.55 \div 0.7$ ($P_s \approx (0.33 \div 0.25) P_{inp}$) is the result of a compromise between rf efficiency and parameter stability (defined by β_g). In general, scaling relations as $\beta_g \sim f^{1/2}$, (4), from S-band to L-band are not favorable for DLW.
The main parameter in the DLW cell is the aperture radius a. It simultaneously defines both Z_e and $\beta_g \sim a^3$. From (5), (see also Appendix A), it is excluded to have a DLW with high $E_0T \geq 12.0 MV/m$ and large $a \geq 20mm$ at moderate $P_{inp} \approx 8MW$ simultaneously. Also it is not possible to have a DLW section with moderate with moderate $P_{inp} \approx 8MW$ $E_0T \leq 6.0 MV/m$ and moderate $a \leq 18mm$ (to save total rf power). Because only two parameters, aperture radius a and lower aperture thickness T_d are available for changing in DLW cells, the DLW section is restricted in combinating of high rf efficiency, parameter stability and a variety of a and E_0T.
From this point of view, SW CC structures are more flexible and open a wider variety to chose high E_0T values in the beginning of the linac to prevent bunch lengthening and moderate E_0T to save rf power at the end of the linac.
The main advantage of the TW mode - the smaller filling time τ_{tw},

$$\tau_{tw} = \int_0^L \frac{dz}{c\beta_g}, \tag{8}$$

is not realized for the L-band range, because for room-temperature SW CC structures rise-time $\tau_{sw} \approx \tau_{tw} \approx 2 \div 4 \mu s$. This parameter is not important, taking into account long ($800 \mu s$) PPA rf pulse.
One preferable point for a DLW is the lower $E_{smax}/(E_0T) = (1.8 \div 2.0)$ ratio for a DLW cells configuration (Fig. 3.1.2 a). With an optimization of the cell to have a higher Z_e or lower β_g values (Fig. 3.1.2 c,d) the DLW loses this preference.
Taking into account, that:
- for a reasonable stability of the parameters the TW mode of operation needs more rf power for the same E_0T and a values;
- the SW CC structures open a wider flexibility for the choice of E_0T and a, allowing to have a high E_0T in the PPA beginning for bunch lengthing reduction and moderate E_0T to save rf power in the PPA main part;
- the difference in filling time for the TW mode and rise-time for the SW mode is not so big and not important for the long PPA pulse,
the SW mode for the PPA accelerating structure is chosen.

3.3 Single or compensated SW mode. Stability of rf parameters

It is well known (see, for example [11], page 655) that in order to realize high Z_e value, SW structures should operate in $\phi = \pi$ mode (ϕ - phase shift of the field per CC structure period). Two options are possible:
- single π mode (monoperiodic structures, one cell - one structure period);
- compensated π mode (so called bi-periodic structures, two cells - accelerating and coupling in the structure period).
The Brillouine diagrams for simple and compensated accelerating structures are shown in Fig. 3.3.1 for the same $k_c = 0.1$ value.

It is also well known, compensated structures have a mutch lower sensitivity to beam

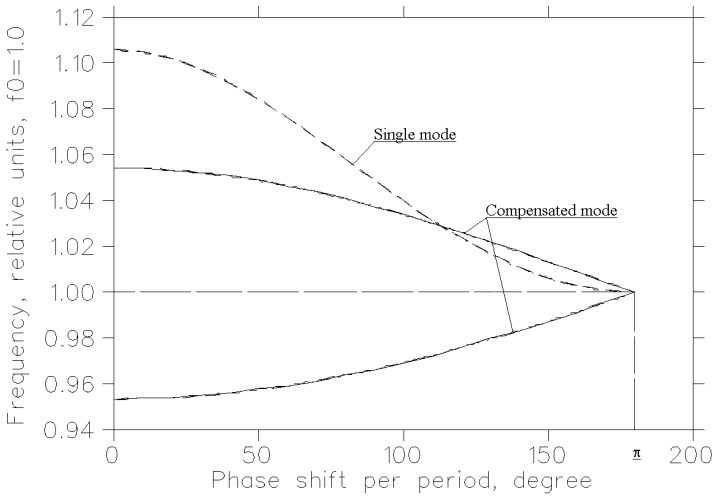

Figure 3.3.1: The Brillouine diagram for the single π-mode structure (broken line) and for compensated π-mode structure (solid line).

loading and cells parameters deviation during manufacturing and tuning. The rms value of the electric field deviation for single π-mode σ_{se} and compensated π mode σ_{ce} are [15]:

$$\sigma_{se}^2 \approx \frac{4\sigma_f^2}{k_c^2}\left(\frac{N^2+N}{3} - \frac{(2N^3-2N^2+N)k_c}{6}\right), \tag{9}$$

$$\sigma_{ce}^2 \approx \frac{64\sigma_{fa}^2}{k_c^4}\left(\sigma_{fc}^2\frac{N^2+3N}{12} + \left(\frac{\delta_f}{f_0}\right)^2\frac{N^3+4N^2+6N}{30}\right), \tag{10}$$

where σ_f is the rms frequency deviation for cells in a single π-mode structure while σ_{fa} and σ_{fc} are the rms frequency deviations for the accelerating and coupling cells in compensated π-mode structure (δ_f is the stopband width, N - number of structure periods in the section). Assuming $k_c = 0.1, N = 17$ and realistic values $\sigma_f = \sigma_{fa} = 0.3\sigma_{fc} = 5.0 * 10^{-4}, \delta_f/f_0 = 2.0{*}10^{-4}$, one gets $\sigma_{se} \approx 0.8, \sigma_{ce} \approx 0.027$. Despite the fact that the PPA beam dynamics does not need severe requirements for accelerating field homogeneity as e.g. multi-cells proton linacs of the "meson-facility" type ($\sigma_e \sim 0.02$), acceleration in the field with $\sigma_e \approx 0.8$ is out range. The section manufacturing and tuning would have mutch more severe tolerances, leading to cost increasing in the case of long π-mode structures.
For PPA accelerating structure OCS and CDS SW compensated π-mode structures may be applied.
The OCS realizations for electron linacs are well known and well tested - [16], [17],[18]. Comparing OCS and CDS structures and taking into account:
- the enlarged coupling coefficient for CDS structure;
- the higher (several percent) shunt impedance in CDS,
and basing on:
- results of numerical simulations [8];
- results of the cold model measurements [19];

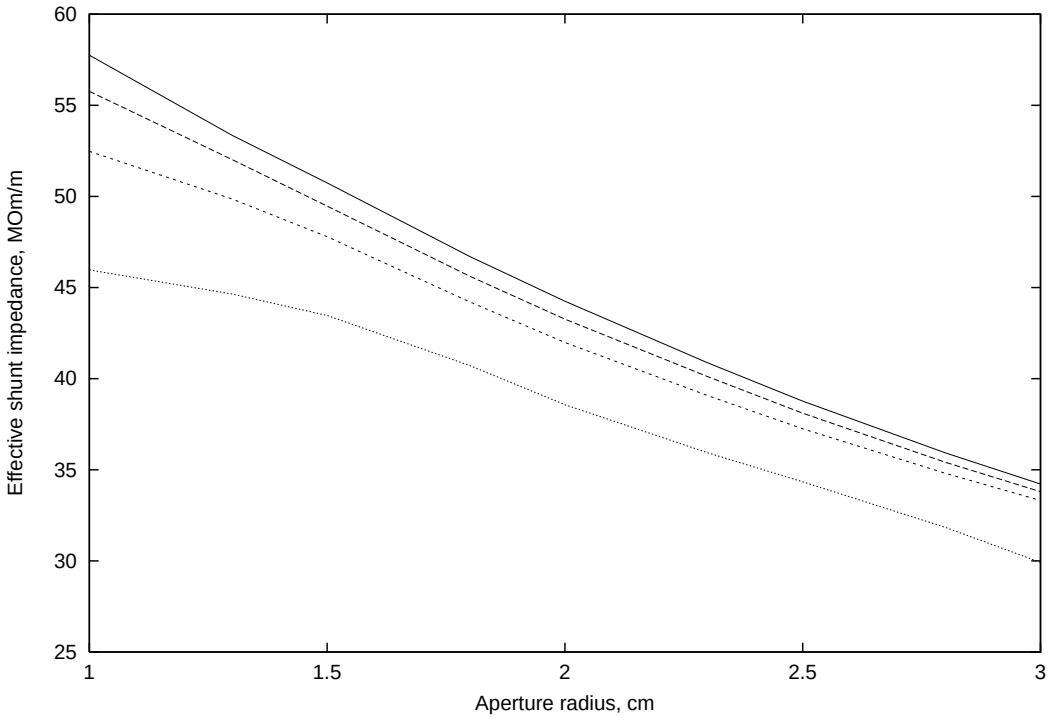

Figure 3.4.1: Effective shunt impedance Z_e vs. aperture radius for different accelerating gradient E_0T. Up to down - $E_0T = 6.0MV/m, 8.0MV/m, 10.0MV/m, 14.0MV/m$.

- and the fact that OCS and CDS are similar in parameters of the accelerating cells (operating mode) and differs in the concept of the coupling mode,
the CDS structure for PPA is recommended.

3.4 Different options and final parameters for the SW structure

The procedure for the SW structure cell shape optimization is described in detail in Appendix A. The optimal shape changes for different E_0T values (Fig. A4). The total web width is chosen to be equal $T_w = 30mm$, consisting of two walls ($13mm$ thick) and $4mm$ for the coupling cell length. The wall thickness of $13mm$ is sufficient for the mechanical strength and for the cooling channel placement. For the optimized cell shape the plots of the Z_e dependences are shown in Fig. 3.4.1 and Fig. 3.4.2 assuming $T_w = 30mm$, $E_{smax} = 40MV/m$.

The plots on (Fig. 3.4.1) and (Fig. 3.4.2) show, in general, the well known behaviour - Z_e decreases with a and E_0T increasing. But due to the extensive optimization these Z_e are maximized. From the beam dynamics study (Chapter 1) two E_0T values $14.8MV/m$ and $8.5MV/m$ are required. The first one is mostly limited by the structure. A maximum reasonable E_0T of $\approx 18MV/m$ may be achieved, ($E_{smax} \leq 40.0MV/m$) but not with the tolerable rf power $4MW$. It also doesn't provide a significant increase of the capture efficiency. The moderate $8.5MV/m$ value is also related to the available rf power and the section length in the second PPA part (restricted by the triplet focusing period length). Even though the Z_e value difference for $E_0T = 14.8MV/m$ and $E_0T = 8.5MV/m$ is not drastic $\approx 14\%$, it is reasonable to chose two cell geometry options.
Z_e depends strongly on a. In order to reduce the number of klystrons one have to increase

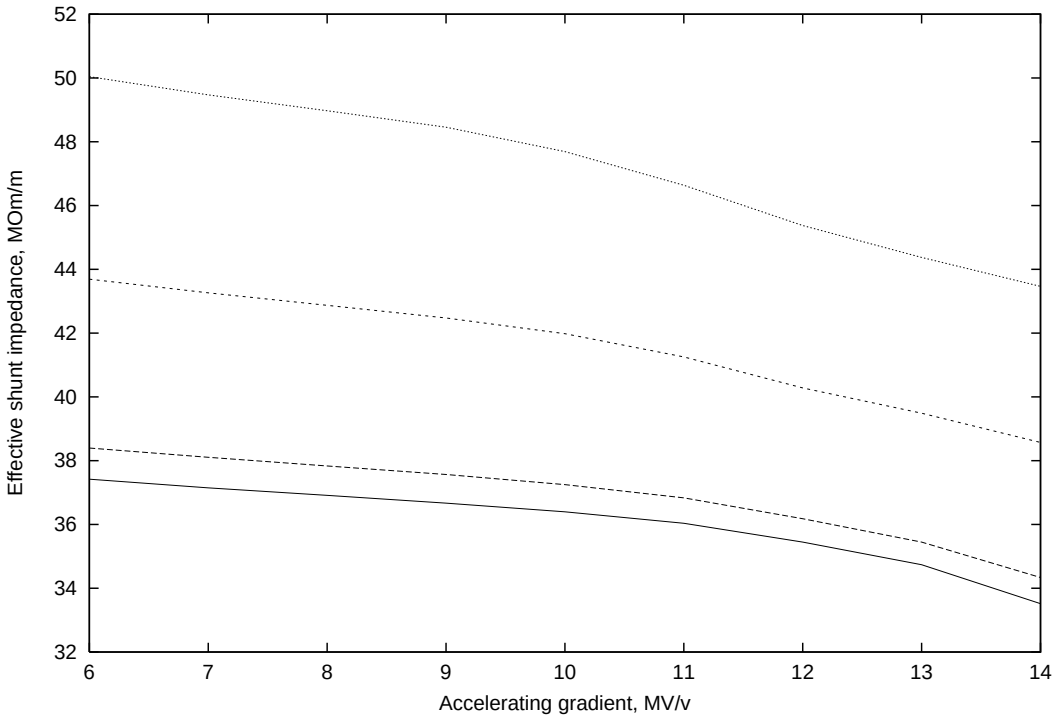

Figure 3.4.2: Effective sunt impedance Z_e vs. accelerating gradient E_0T for different aperture radius a. Up to down - $a = 15mm, 20mm, 25mm, 26mm$.

Z_e at least by $(22 \div 25)\%$ to save two klystrons. It is difficult to save one klystron only due to the PPA structure (0.5 in the first PPA part and 0.5 in the second part is not a good solution). One klystron in the first PPA part or one in the second is also not a good solution taking into account all related topics as beam dynamics and focusing structure. So it is reasonable to save two klystrons, but it would lead to $a \approx 16mm$ and the PPA acceptance would be decreased essentially. The aperture diameter choice $a = 26mm$ looks not usual, but it is matched to the total PPA scheme, leading improved beam parameters. For such big aperture diameter the total rf efficiency of the SW accelerating structure is still higher than for TW structure with aperture radius $a = 15mm$.
The final parameters for the SW CDS structure are listed in the Table 3.4.1.
The general view for the CDS structure with $E_0T = 14.8MV/m$ is shown in Fig. 3.5.1 and in Fig.3.4.3 for $E_0T = 8.5MV/m$. The last picture is shown with a coarse mesh to present the general picture only. A fine 3D optimization (with $\approx 3.5 \cdot 10^6$ mesh point for the geometries of Fig. 3.5.1 and Fig. 3.4.3) has been performed to optimize the coupling window shape. The coupling windows, following the CDS idea, are chosen shorter and wider in comparison to standard OCS slots. In this CDS geometry the coupling window shape is optimized to reduce as mutch possible as the rf current redistribution due to the windows. As the result, the shunt impedance obtained in 3D calculations is not less than shunt impedance in the 2D calculations. It confirms the general CDS particularity: - no Z_e decrease with increasing coupling coefficient [19]. Due to the large relative aperture radius $a/\lambda_0 \approx 0.113$ in the CDS option, there is no space to realise the maximum coupling coefficient $k_c \approx 20\%$ for CDS at $\beta = 1$ [8]. For this purpose the lower window radius should be smaller. But the values obtained are higher than for OCS structures and are sufficient for the PPA applications taking

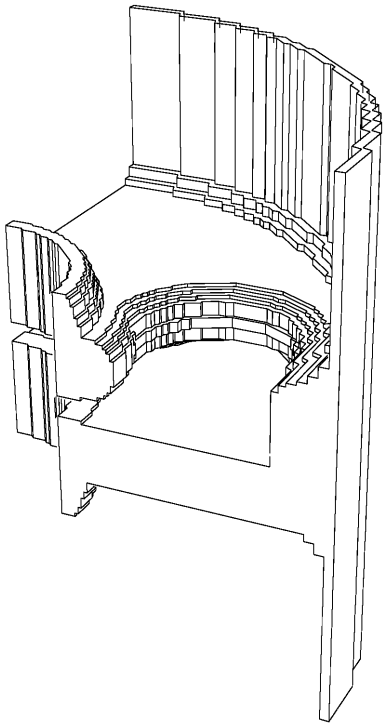

Figure 3.4.3: The draft picture for the CDS structure, $E_0T = 8.5MV/m$.

into account that the PPA sections are not so long.

3.5 Thermal stress analysis for the SW structure

With the high accelerating gradient $E_0T \approx 14.9MV/m$, long rf pulse $\approx 800\mu s$ and a repetition rate of $5Hz$ the first sections of the PPA operate with a high heat load of $P_h \approx 30kW/m$. The power handling capability for OCS was studied [17] during the development of cw electron linacs for industrial purpose [16]. On the one hand, the possibility of a power handling of $P_h \approx 150kW/m$ has been shown (but with an adaptive rf system and boiling water cooling, which is not applicable for the PPA). From the other hand, a careful thermal stress analysis is important to ensure stable operation and reproductibility of parameters.
For the CDS structure a thermal stresses study has been performed by direct 3D simulation of the coupled field problem. Both for the CDS option for the first PPA part (see Fig. 3.5.1) and for the second part, 3D MAFIA calculated distributions of rf losses, scaled to real E_0T values, were used as input data (boundary condition) for the temperature and stress calculations with ANSYS. For this purpose special procedure and interface code has been developed.
The scheme for cooling - two web channels and several circumferential channels is the same as in [16]. Preliminary estimations have shown, that the web channels are necessary for the drift tube region cooling. With only circumferential channels the drift tube temperature will be $\approx 250C^o$. The study has been performed for several values for the heat transfer constant

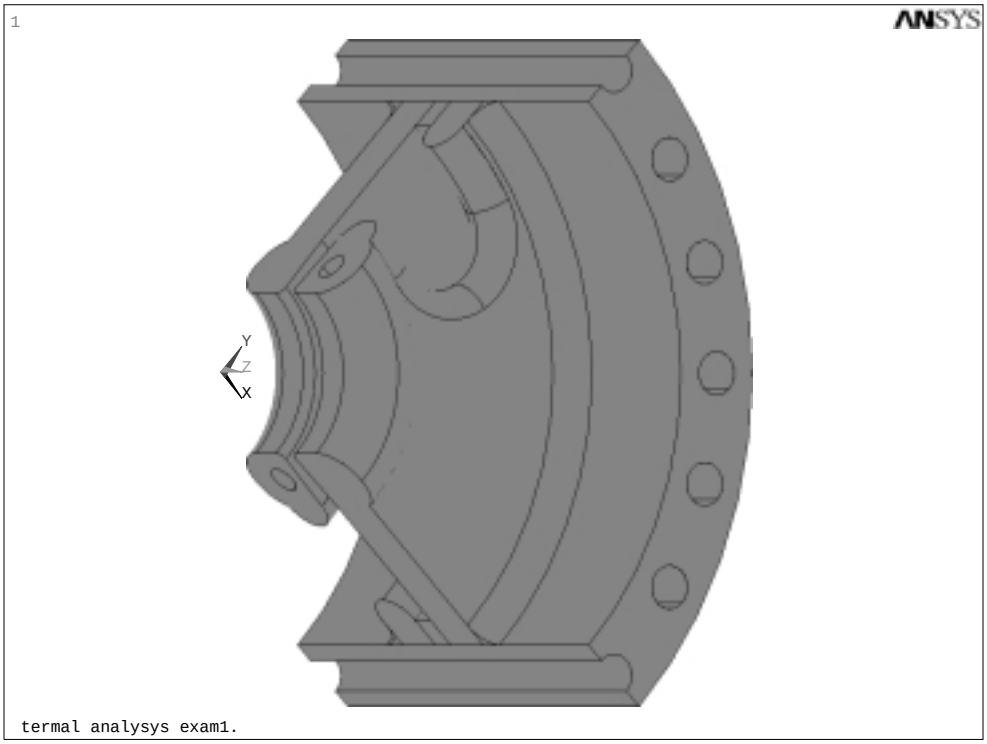

Figure 3.5.1: The CDS structure for the first sections of the PPA.

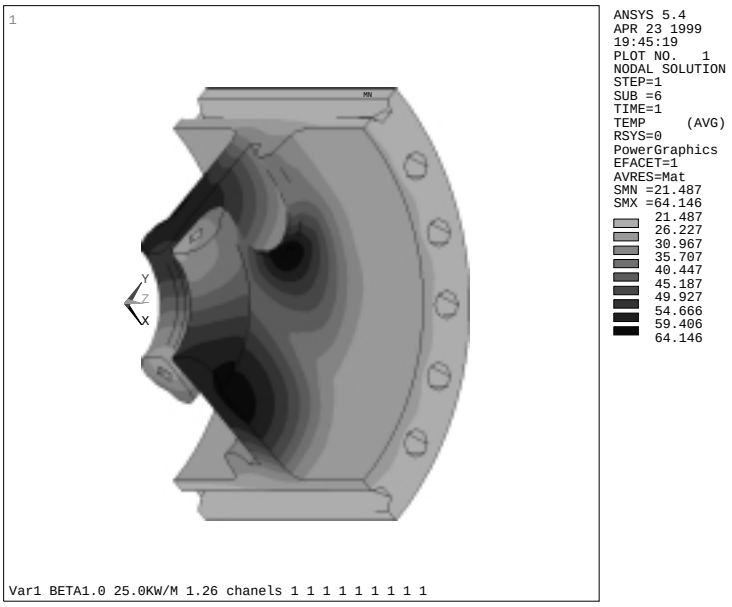

Figure 3.5.2: The temperature distribution of the CDS structure surface for a heat load of $27kW/m$.

η, corresponding to a water flow velocity of $1.0 \div 3.0m/s$. For high gradient CDS sections $P_h = 26.0kW/m$ was considered, and $P_h = 5.7kW/m$ - for CDS sections with moderate gradient.
A typical temperature distribution is shown in Fig. 3.5.2. There are "hot" regions at the structure surface - at the drift tube (between the web channels) and at the ends of the coupling windows. The overheating value t_h - the difference between local surface temperature and cooling water temperature - may achieve $t_h \approx 47C^o$ for $P_h \approx 26kW/m$ and depends only weakly on η. The heat conductivity of copper is not sufficient to transfer a large heat flow from the "hot" point to the cooling channel.
Overheating leads to an increasing of the surface resistance (total reduction of the shunt impedance $\approx (2 \div 4)\%$, not dangerous), to nonuniform surface deformation, and to development of internal stresses.
The frequency shift due to the surface deformation was estimated for the accelerating (operating) mode frequency and for coupling mode frequency by using perturbation theory:

$$\frac{\delta f_{a,c}}{f_{a,c}} \approx \frac{\int_S (\mu_0 H_{a,c}^2 - \epsilon_0 E^2 a, c)\vec{n}d\vec{S}}{4W_{a,c}}, \tag{11}$$

where $f_{a,c}, W_{a,c}, E_{a,c}, H_{a,c}$ are frequency, stored energy, electric and magnetic fields distributions for accelerating mode and coupling mode respectively.
Results of simulations for the temperature and stress distributions are summarized in Table 3.5.1. Due to the relatively small overheating a linear approximation of the results is valid and $t_h, \delta f_{a,c}/f_{a,c}, S_{stmax}$ values for fixed η and CDS geometry are proportional to the heat

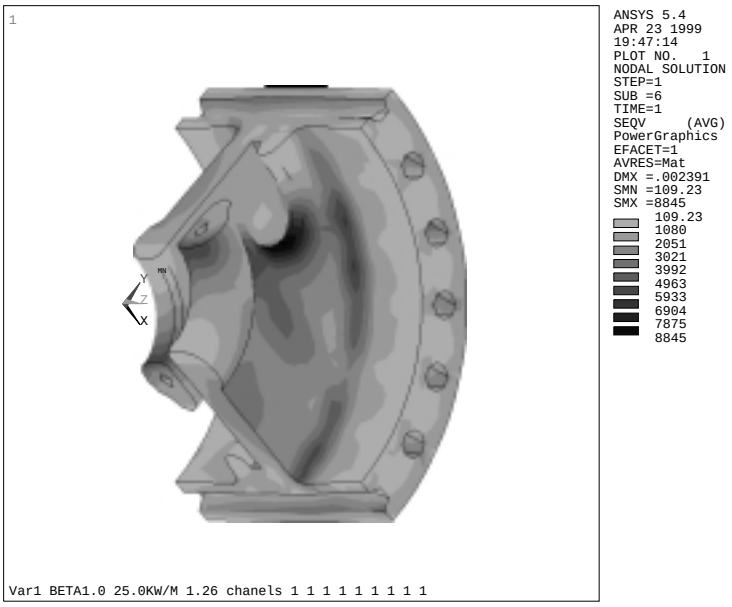

Figure 3.5.3: Von Mises thermal stress distribution for a heat-load of $27kW/m$.

load P_h.
The operating frequency shifts due to the surface deformation ($\leq 200kHz$) are within tolerable limits to be removed by the frequency control system. The frequency shifts for the accelerating mode and the coupling mode have different signs, leading to a stop-band opening during the section heating. It means, that structure should be tuned at normal temperature with some stop-band width, with the purpose to close the stopband in the operating regime. For high heat load $P_h \approx 27kW/m$ with the usual web channel scheme the internal stress value $S_{stmax} \sim 900kg/cm^2$ exceeds the yield strength $S_{stlim} \approx 530kg/cm^2$ of OFHC copper. S_{stmax} also doesn't depend strongly on η. Increasing η is limited by the water flow velocity ($\leq 3m/s$ to preserve channel erosion). To keep $S_{stmax} \leq S_{stlim}$, another scheme for the web cooling channel (see Chapter 3.6.1, second CDS cup option) has been developed for the first sections in the PPA. For the other structure with $E_0T \approx 8.5MV/m, P_h \leq 7.5kW/m$) S_{stmax} is acceptable.

3.6 Proposal of the CDS structure design. Manufacturing and tuning procedures

Each Accelerating Section (AS) consists of separate cups, (Fig. 3.6.1), brazed together in a vacuum or hydrogen furnace with silver alloy. Each cup contains one-half of the accelerating cell and one-half of the coupling cell. In each period of the structure there are two cups. Joints between caps are in the middle-planes of accelerating and coupling cells. The cups are machined from oxygen-free copper by using numerically controlled lathe and milling ma-

Table 3.5.1. The results of the thermal stress simulations for the CDS accelerating sections. η is the heat transfer constant at the surface of the cooling channels, t_h is the maximum difference between local surface temperature and cooling water temperature, δf_a is the accelerating mode frequency deviation due to the surface deformation, δf_c is the coupling mode frequency deviation due to the surface deformation, S_{stmax} is the internal stress value.

P_h	η	t_h	δf_a	δf_c	S_{stmax}
kW/m	$W/(m^2C^o)$	C^o	kHz	kHz	kg/cm^2
5.7	7250	18.55	76	91	460
5.7	9000	17.44	68	84	418
26.0	9000	47.30	-255	296	980
26.0	12600	44.16	-210	221	901

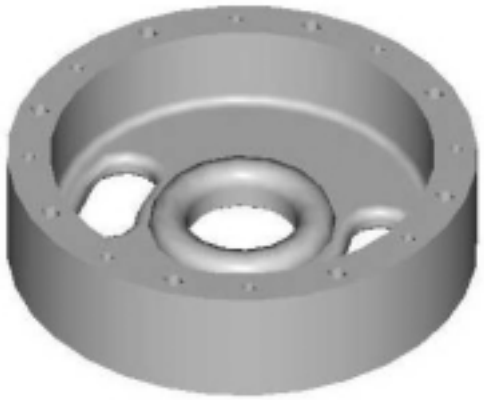

Figure 3.6.1: The cup of the CDS structure.

chines. Due to the enlarged coupling k_c in CDS, tolerances for all accelerating cell dimension are relaxed in comparison to OCS structures and values of $\pm(50 \div 80)\mu m$ are reasonable. For the length of the coupling cell the deviations should be smaller $\pm(15 \div 25)\mu m$. All technological methods and equipment used in the manufacturing process are well known and widely used in the fabrications of accelerating structures. The fabrication of the CDS structure is cheaper, in comparison to other SW structures, due to the CDS simplicity and the relaxed tolerances.

Taking into account the reasonably small section length, the brazing procedure also is usual. Cooling circuits are composed of series of flow circumferential channels and two web channels. Circumferential channels (with diameter $\approx 10mm$) are drilled into the outer wall of the cup. Another version of the circumferential channels is possible by brazing rectangular tubes into grooves, preliminary machined along structure (like the channel along DLW S-band sections).

Also two options of the cups design are presented, differing in the web channels design.

- in the first option two straight web channels (with diameter $\approx 7mm$) are drilled across through the 13 mm thick web between the coupling slots and nose cones (Fig. 3.6.2). The water flow in these channels has opposite direction. Such web channel design was considered in Chapter 3.5, showing tolerable cooling.

- in the second option the web has a circular groove and a ring (Fig. 3.6.3). The ring is

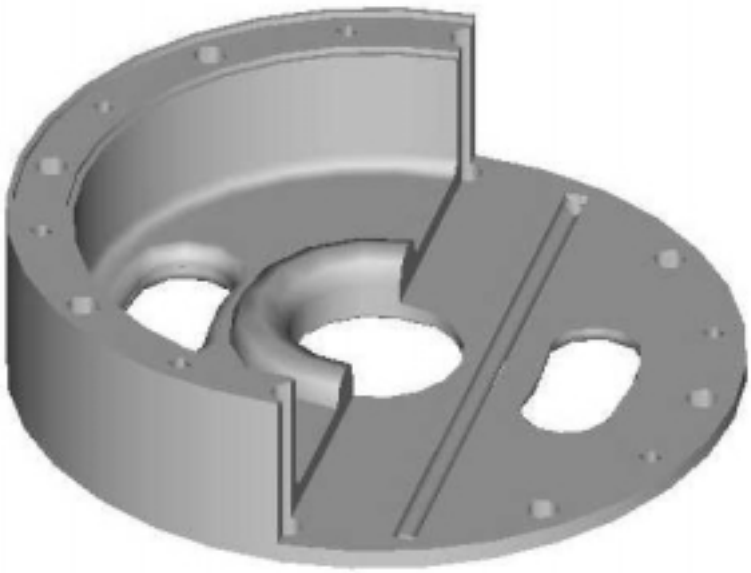

Figure 3.6.2: The CDS cup with straight web chanel.

welded into the web body by electron-beam welding. The groove and four radial channels, drilled in the web, form two channels for the cooling of the nose cone area and the web body (Fig. 3.6.4). The water flow has opposite direction in these channels.

The first (usual) option is simpler and may be recommended for the main part of the PPA accelerating structure. For the first four PPA sections with $E_0T \approx 15MV/m$ the second scheme has been chosen, which is a more complicated but provides more effective cooling (see Chapter 4.3), resulting in a more uniform temperature distribution, acceptable internal stresses and lower frequency deviations.

The scheme of the cups assembly into the section is shown in Fig. 3.6.5 for the second cup option. To reduce the quadruple perturbation of the accelerating field by the coupling windows, windows are placed face-to-face at opposite sides of the accelerating cell.
In order to restrict the section diameter to $\approx 220mm$, cooling water inputs and outputs take place at the ends of the section.

The tuning procedure for the CDS structure was developed and described in [19].
As usual, tuning of a compensated accelerating structure should have three procedures:
- tuning of the accelerating mode frequency f_a to f_0;
- tuning of the coupling mode frequency f_c to confine f_a (closing of the stop-band);
- tuning of the accelerating field distribution (if needed).

During the mode frequency tuning there is no tuning of individual cells due to large coupling. Both for accelerating mode and coupling mode tuning the change in dimensions was the same for all cells in the section.
The accelerating mode frequency tuning in CDS doesn't differ from the same procedure in other CCL and may be performed by increasing R_a (decreasing of f_a) or drift tube shortening (increasing of f_a).
In structures with large k_c direct determination of the coupling mode frequency both for each cell and for the total section, which is reasonable in usual CCL structures, provides a large error $\Delta f_c \approx f_c k_c^2/2$. The coupling mode frequency f_c tuning is based on general properties

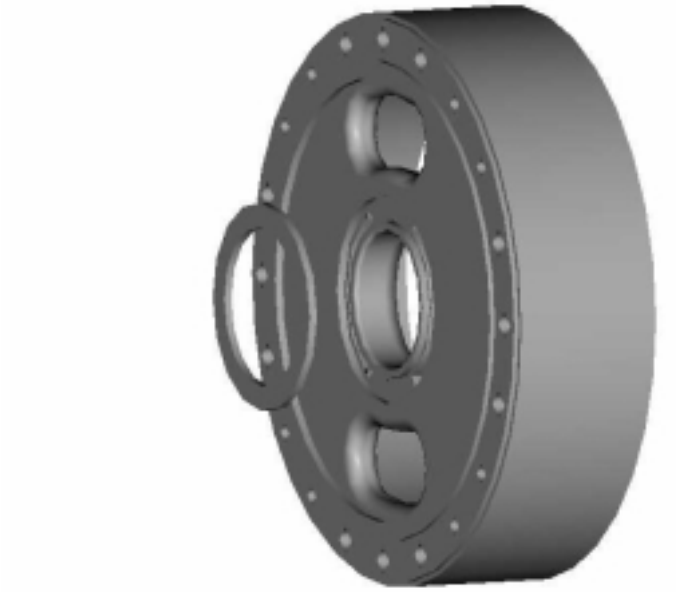

Figure 3.6.3: The second option of the CDS cup.

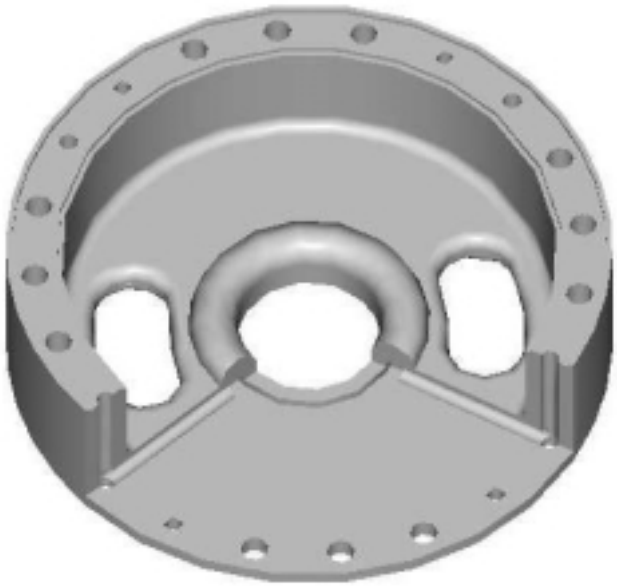

Figure 3.6.4: The cooling scheme for the second CDS cup option.

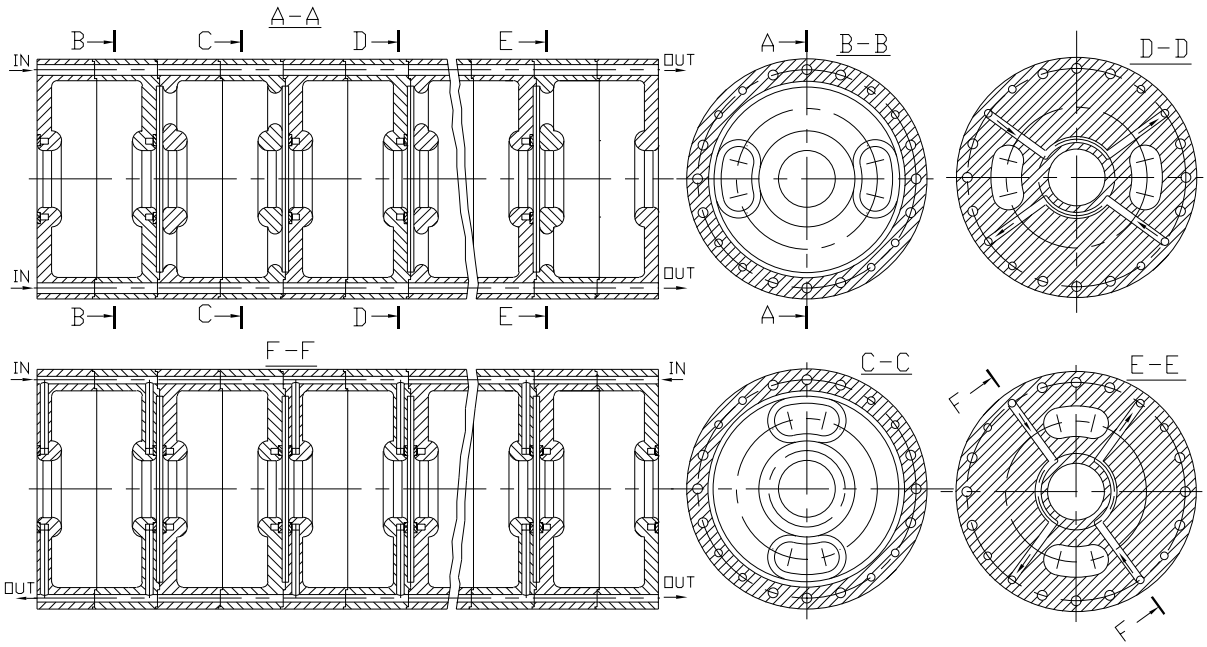

Figure 3.6.5: The CDS section scheme.

of compensated structures. In all compensated structures the stop-band width $\delta f = f_a - f_c$ may be determined [20] as:

$$\delta f = \frac{n^2 \Delta F_m - m^2 \Delta F_n}{m^2 - n^2}, \qquad \Delta F_m = f_m^+ + f_m^- - 2f_0, \tag{12}$$

where f_m^+ is the mode frequency of $\frac{(N-m)\pi}{N}$ type at the top branch of dispersion curve, and f_m^- - at the bottom branch.
The coupling mode frequency tuning in the CDS may be performed by increasing R_c (decreasing of f_c) or by increasing the gap between half drift tubes l_c (increasing of f_c). Because the CDS cells are symmetric, normally no field distribution tuning is needed. For the the CDS cold model [19], the electric field distribution, as the result of a bead-pull measurements, is shown at Fig. 3.6.6. It exhibits the standard deviation value $\sigma_E = 1.05\%$.

3.7 Summary

The comparison of the TW and SW operating modes for the PPA L-band case show preference for the SW mode, resulting in flexibility of the parameter choice and higher total rf efficiency. The SW structure with compensated π-mode in the CDS option, resulting in an enlarged coupling coefficient at the same shunt impedance, small transverse dimensions, a simple design and high parameters stability. Two options are chosen for high and moderate accelerating gradients. The structure cells shape is highly optimized, resulting in a minimal Z_e reduction with increasing aperture diameter. As the result of the thermal stress study two options of the structure cooling are developed, showing realistic solutions for a high heat load structure operation. All proposals for the accelerating structure are sufficient for a technical design and development during the PPA accelerating system construction.

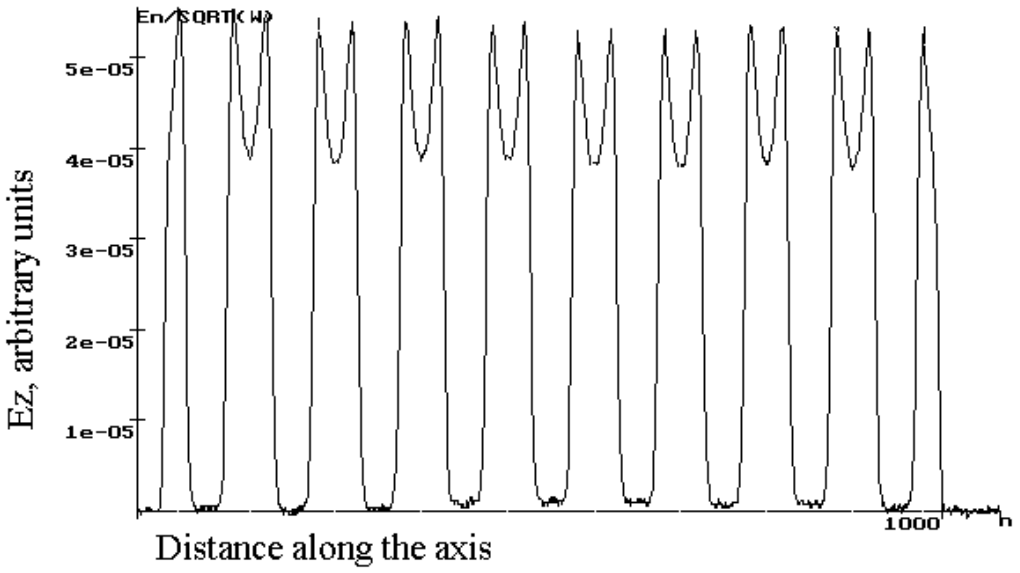

Figure 3.6.6. Measured electric field distribution along the axis of a CDS cold model.

4 RF power system based on TESLA standard equipment

To reduce the total linac cost and to simplify maintenance it is supposed that the PPA rf system should be based on standard powerful TESLA equipment [1] - the same $10MW$ klystron with two waveguide outputs, the powerful circulators after the klystron output windows, anode modulator and standard WR650 waveguide as Transmission Line (TL).

4.1 Special requirements

But the PPA rf system should take into account the PPA particularities. Other than the regular TESLA rf system, in the PPA each klystron feeds only two normal conducting Accelerating Sections (AS), which parameters (wall rf power dissipation, Q-factor) are identical. Due to the low - as compared to a superconducting structure - Q_0-factor (≈ 23000), the field rise-time for the PPA AS is short enough $3\tau_l \approx 7.5\mu s$. The rf pulse with $\approx (820 \div 830)\mu s$ duration is sufficient for the PPA purpose and the standard TESLA modulator might be modified to reduce the pulse length. Usually this is easier than to increase the pulse length. The PPA rf system has nine rf channels. Each rf channel consists of a complete set - klystron, modulator, pulse transformer, circulators, powerful TL and control system. All rf channels are driven by the TESLA drive line. It is designed to have $8MW$ (in equal parts) at the accelerating sections entrance. The rest of $2MW$ is estimated as rf losses in the circulator (assuming attenuation of $\approx 0.16dB$), in the transmission line and a small reserve for regulation.
The beam loading in the PPA AS is much lower than in the TESLA cavities and it may be disregarded during the cavity tuning, including the coupling with the power TL. It means that the sections have to be tuned on the operating frequency and the coupling ratio with the TL should be chosen to minimize the reflected power without beam.

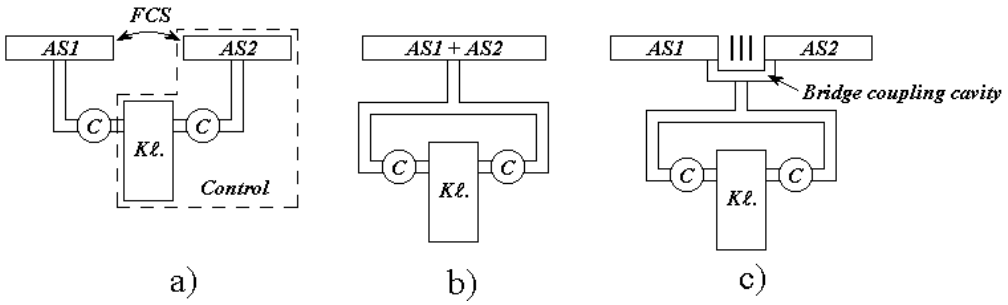

Figure 4.1. Different option of the rf power distribution. a) - under further consideration, b) for the first PPA part with rf power summation, c) for the second PPA part.

Taking into account that the TESLA kystron has two output windows, two options for the PPA rf system are possible.

It looks very attractive to add the rf power from the two shoulders, so that only one waveguide will go to the accelerating sections (Fig. 4.1. b,c). Right now we can not refer to this solution as proved for particle accelerator technology. We don't see a prohibition for this solution, but this design must be considered carefully and tested for reliability at a high rf power high level.

If the rf power from klystron shoulders will be summarized, the rf and control system structure becomes evident. Multi-cavity linacs with one rf channel per accelerating cavity are well investigated in the design of proton linacs with energies $\approx (600 \div 1000) MeV$ and there is world-wide experience in the technical development of the rf systems. For the PPA system this solution is acceptable. For the accelerating structure in the first PPA part each two sections should simply be joined into one section with doubled cell number. The accelerating structure parameters allow such a transformation. For the second PPA part two AS should be joined with a coupling bridge cavities. In this case the waveguide should be connected to the bridge cavity. Such solution is also well investigated [21].

In this report we consider another scheme - the two klystron outputs are independent (Fig. 4.1. a). This proposal is strongly based on the next PPA points:

- The PPA linac is a linac 'in average'. Due to the wide e^+ energy spread there are not so rigid requirements in the phase and amplitude adjustment as for proton linacs of the meson-facility type.
- Two accelerating sections belonging to one rf chanel must be manufactured and tuned identically and the TL phase length (including circulator) to both sections must be equalized in the limits $(2 \div 3)^o$.
- The cavity frequency control system must keep the resonant frequency for both AS to provide a phase difference $\leq (2 \div 3)^o$.

4.2 Narrow range field amplitude adjustment

Feeding rf power from one klystron to two sections generates some problems, because the rf voltage amplitudes and the phase relations of both sections have to be adjusted separately. The first problem can be solved by connecting the klystron to identically tuned sections and by changing the coupling ratio in small limits with the TL. The solution of the second

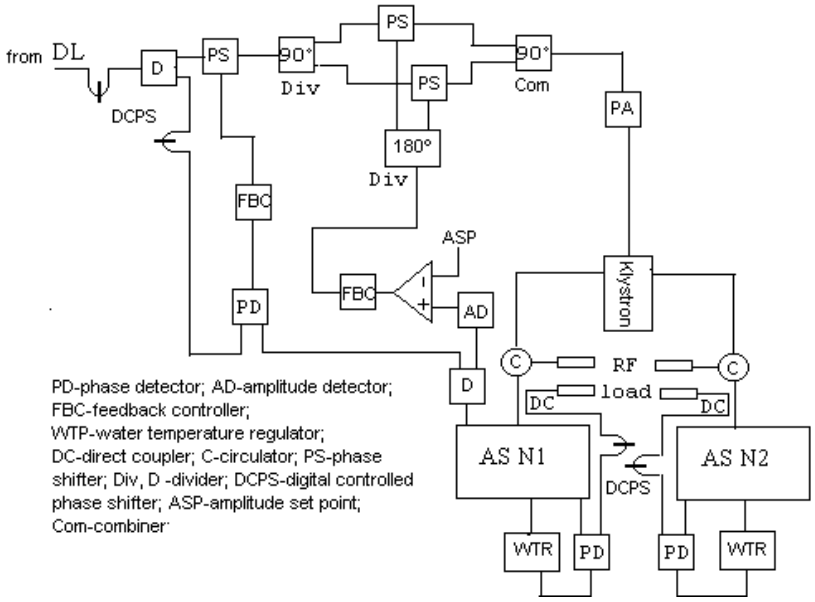

Figure 4.2.1a. The simplified scheme of the PPA rf system.

problem assumes equal phase lengths of the TL between the klystron output and both AS and exact maintenance of the AS tuning. Installation of a powerful phase regulator solves this problem entirely. But at present a powerful phase regulator is only under consideration for the WR650 waveguide.

It is necessary to examine the possibility to adjust the phase relation between the rf fields in the AS by detuning them. The simplified scheme of the PPA rf system is shown in Fig. 4.2.1. Only in one of the two AS the Feedback Control System (FeedCS) supports the cavity voltage at the set-point level, while in the other AS maintenance of the rf field level depends on the quality and accuracy of the Cavity Frequency Control System (CFCS) working for both cavities. Due to the circulator in the TL every cavity as if it is fed by an rf source with constant RF power P_g, which is distributed between the cavity (P_c) and the circulator load P_r. It can be shown that for tuned AS:

$$P_r = P_g \frac{\xi_c^2}{4+\xi_c^2}, \qquad \phi_c = arctg(\frac{\xi_c}{2}), \tag{13}$$

where $\xi_c = 2Q_c\Delta f_0/f_0$ is the relative AS detuning and ϕ is the phase shift in the detuned AS. Expression (13) allow to estimate the phase shift due to the AS detuning and the amount of additional rf power needed to compensate the reflected power.

The procedure to find the necessary phase relations between the rf fields is as follows:

1 - The AS $N1$ is detuned by changing the set-point of the CFCS. The feedback in the FeedCS, stabilizing the rf voltage in this AS, is open. According to (13), the AS $N1$ rf voltage amplitude and phase are:

$$U_{c1} = U_{c0}\frac{2}{\sqrt{4+\xi_1^2}}, \qquad \phi_{c1} = arctg(\frac{\xi_1}{2}), \tag{14}$$

where U_{c0} is the rf field amplitude in the tuned AS with the matched input impedance.

2 - The feedback in the FeedCS, stabilizing the rf voltage in the AS $N1$, is closed. After that

the rf voltage vector in the AS $N2$ is turned to the angle $-\phi_{c1}$ and the rf voltage amplitude is increased $\sqrt{1+\xi_1^2}$ times.
3 - To restore the previous U_{c0} amplitude in the AS $N2$, the latter one also has to be detuned, so that the common phase shift in it achieves $\phi_{c2} = -2\phi_{c1}$. The price for this way of the phase shift control between cavities is the $P_r = P_g\xi_1^2/2$ reflected rf power, dissipated in the circulator loads.

4.3 Feedback control system for rf voltage stabilization

The realization of the FeedCS depends on the correct choice of the control coordinates. The particle dynamics simulations are based on amplitudes and phases of the rf voltages in the accelerator cavities. The choice of a polar coordinate system (amplitude and phase FeedCS) allows immediately to estimate the efficiency of the amplitude and phase stabilization in the real time domain. Such (A/P) control system demands phase and amplitude detectors as demodulator, and precision rf phase shifters and rf control attenuators as modulator.
The new microwave technologies opens new possibilities in the FeedCS controller design, as modulator and demodulator with rectangular coordinates and (I/Q) controler, particularly, for digital systems. The amplitude and the phase has to be either calculated, using DAC's and ADC's, or be measured with phase and amplitude detectors. Since it is impossible to apply the fast digital control systems (due to the lower Q_c value) for the stabilization of the rf voltage vector in the PPA, as it was developed for the TESLA [1], we consider both the (A/P) and the (I/Q) control system.
For the high Q-factor accelerating cavities the first order equation for the complex amplitude $\overline{U_c(t)}$ of the rf voltage is valid:

$$\tau_l \frac{d\overline{U_c(t)}}{dt} + (1+j\xi_c)\overline{U_c(t)} = \frac{\tau_l}{\tau_c}\overline{I_g}R_c, \tag{15}$$

where τ_l, τ_c are the cavity time constants corresponding to the loaded and unloaded cavity, $\overline{I_g}$ is the complex amplitude of the rf generator current and R_c is the cavity shunt impedance.
The polar (A/P) coordinates. After the usual transformations, one can derive from (15) the equation system for $\Delta a_c and \Delta\phi_c$ - small amplitude and phase deviations from the steady-state values. After the Laplace transformation the direct and the cross couple transfer functions are determined from:

$$\begin{pmatrix} \Delta a_c(s) \\ \Delta\phi_c(s) \end{pmatrix} = \frac{1}{(1+s\tau_l)^2+\xi_c^2} \begin{pmatrix} \tau_l\frac{1+\xi_c^2+s\tau_l}{\tau_l\sqrt{1+\xi_c^2}} & |\overline{U_{c0}}|\xi_c\tau_l s \\ -|\overline{U_{c0}}^{(-1)}|\xi_c\tau_l s & 1+\xi_c^2+s\tau_l \end{pmatrix} \begin{pmatrix} \Delta I_g(s)R_c \\ \Delta\phi_g(s) \end{pmatrix},$$

The rectangular (I/Q) coordinates. In this coordinates $\overline{U_c(t)} = U_x(t) + jU_y(t)$. One can derive the following equation:

$$\begin{pmatrix} U_x(s) \\ U_y(s) \end{pmatrix} = \frac{\tau_l}{\tau_c(1+s\tau_l)^2+\tau_l\xi_c^2} \begin{pmatrix} 1+s\tau_l & \xi_c \\ -\xi_c s & 1+s\tau_l \end{pmatrix} \begin{pmatrix} I_x(s)R_c \\ I_y(s)R_c \end{pmatrix},$$

From these expressions follows:
- In the transfer functions of the detuned cavity there are cross coupled links between feedback loops both in the polar and rectangular coordinates.
- In the frequency domain the cross coupled links in both coordinates are different. With

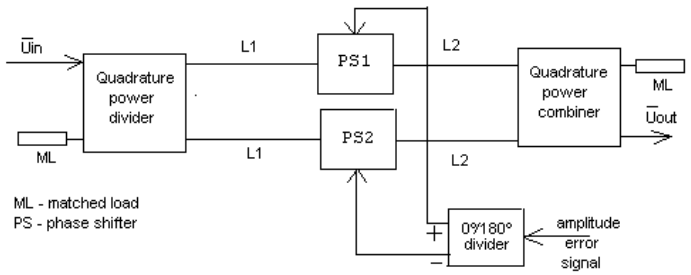

Figure 4.3.1. The variable attenuator with two voltage controlled phase shifters.

growing frequency they fall off as f^{-1} in the (A/P) coordinates and as f^{-2} in the (I/Q) coordinates. It means that the influence of the cross coupled links in the (I/Q) coordinates is less than in (A/P) coordinates.

- the (I/Q) feedback control systems keep linearity at any value of disturbances while the (A/P) FCS - at small disturbances only.

In the general case the cross coupled links diminish the stability and worsen the quality of the FeedCS. Artificial cross coupled links may be realized both in the (A/P) and the (I/Q) feedback control systems, destroying links caused by cavity detuning. In the (A/P) control system the design of artificial cross coupled links isn't simple due to the nonlinear cavity transfer function, but this problem also can be solved [22]. As a result, both loops in each system of coordinates become independent from each other.

Cross coupled links in the modulator. Another source of cross coupled links between two control loops in different system coordinate (A/P or I/Q) is a FeedCS modulator. In the (A/P) feedback control system the modulator consists of a control phase shifter (PS) and a control attenuator (control rf amplifier). In the modulator a phase rf signal modulation is accompanied by an amplitude modulation and vice versa. The amplitude modulation can be suppressed by installation of a limiter after the PS, the phase modulation - by means of the correct choice of the control attenuator. At Fig. 4.3.1 a control attenuator without spurious phase modulation is shown. It is successfully working in the feedback control systems of the main part of the Moscow Meson Factory [23] with an input signal level of $+30dBm$. The output signal varies from $+28dBm$ up to $-6dBm$.

For the (I/Q) option of the FeedCS the whole circuit of the demodulator and modulator is presented in Fig. 4.3.2. Cross coupled links between I and Q components may appear due to several reasons:

- A phase deviation from perfect quadrature in the power dividers PD1, PD2 and power combiner PC1.
- Different coupling between the input and the output of all qudrature power dividers PD1, PD2 and combiner PC1.
- A nonlinearity in the mixer characteristics.
- A time-varying phase shift in the power amplifier . It induces a rotation of the control

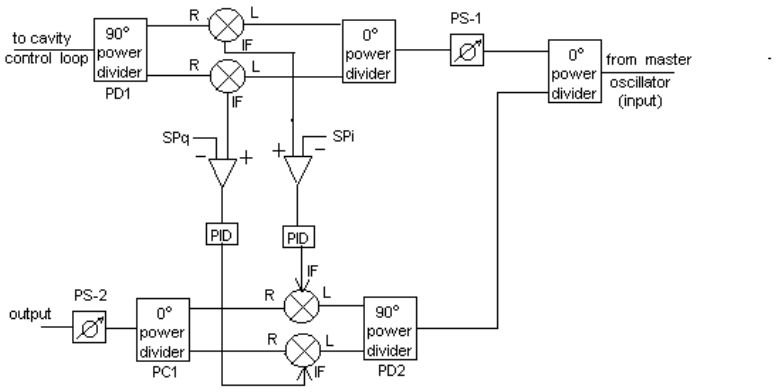

Figure 4.3.2. The modulator and demodulator circuits for (I/Q) feedback control system.

vector, an effect for which, for small phase shift variations, the I and Q loops are too weakly cross coupled.

The relationship between I and Q components in the modulator circuit changed drastically during significant phase shifts in the rf channel (klystron, preamplifier, power TL). To minimize the control effort of the feedback loop and to decrease the influence of the mixers nonlinearity it is worth while to put the phase shifters PS1 and PS2 into operation. The phase shifter PS1 allows to set up the same I and Q set points. PS2, switched on as a phase controller in the simplest slow feedback phase control system, unloads the main fast analog (I/Q) system from large phase drifts.

Time delays. The time delays τ_d in the power TL and in the feedback coaxial cables play a significant role in the behaviour of the FeedCS. Assuming each individual element in the control loop can be described as a first order unit with time constant $\tau_i \ll \tau_l$, the static loop gain K_{st} and the self-excitation frequency f_{ex} can be estimated as:

$$K_{st} \sim \frac{\pi \tau_l}{2\tau_\Sigma}, \qquad f_{ex} \sim \frac{1}{4\tau_\Sigma}, \qquad \tau_\Sigma = \tau_d + \sum \tau_i. \tag{16}$$

Usually, τ_d has the main influence on K_{st} and f_{ex}. Contributions to the rest of the loop units are not so significant. For the TESLA klystron the time constant is $0.02\mu s$, for the (I/Q) modulator $0,016\mu s$ [1]. If the cavities are placed far from the klystron and $\tau_d \approx \tau_l$, it is reasonable to use a Smith predictor. If $\tau_d \geq \tau_l$, an integrator has to be introduced in the feedback controller, lowering the quality of the FCS. So, the structure of the feedback controller is mainly determined by the relationship between the τ_d and τ_l.

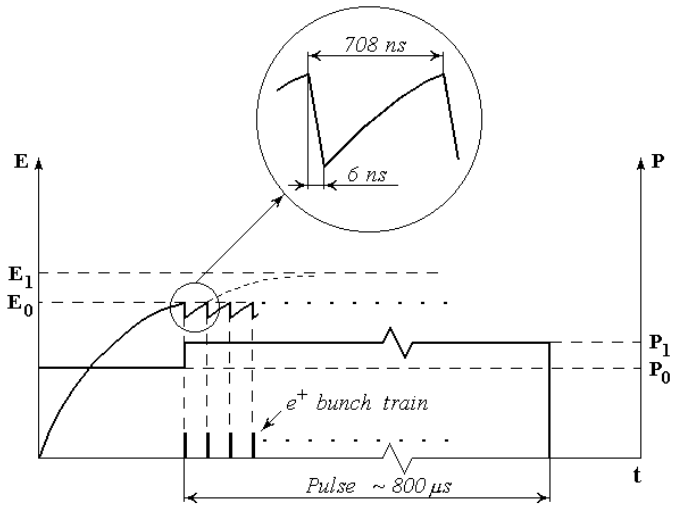

Figure 4.4.1. The simplified diagram for the accelerating field amplitude.

4.4 Beam loading

The PPA bunch train represents a sequence of very short e^+ bunches following with a period $\delta t \approx 708ns$, so one bunch comes after 920 empty rf periods. The additional rf power needed to compensate rf energy losses for the e^+ beam acceleration depends on $\delta t, \tau_l$ and the energy W_b, acquired by the beam in the cavity. No additional power is necessary if $\delta t \geq 3\tau_l$ and the acceleration takes place for account of the cavity stored energy only. On the contrary, if $\delta t \sim f_0^{-1}$, the additional rf power is $P_b \sim \frac{q_b E_0 T L}{\delta t}$, where q_b is the bunch charge and L is the accelerating section length. Due to the application of room-temperature accelerating structures with $\tau_l \approx 2.5\mu s$, in the PPA the intermediate case is realized. Several time values are important to describe it. The time of flight of the e^+ through the long (17 cells) AS is $\tau_f = 8.5 f_0^{-1} \approx 6ns$. The time of the travelling wave propagation τ_{tr} through the long AS is:

$$\tau_{tr} = \frac{L}{c\beta_g}, \qquad \beta_g = \frac{\pi k_c}{4} \approx 0.063, \qquad \tau_{tr} \approx 100ns. \tag{17}$$

The time to restore the AS field level without additional rf power $3\tau_l \approx 3Q_0/(2\pi f_0) \approx 7.5\mu s$. The simplified time diagram for the accelerating field amplitude is shown in Fig. 4.4.1. The accelerating voltage amplitude in the AS has a 'saw-tooth' form, because the FeedCS is not so fast to react at each bunch. Suppose, before the bunch train entered an accelerating field amplitude E_0 was in the AS, corresponding to the rf generator power P_0. Passing through the AS, the first e^+ bunch takes out from the stored energy W_c the part $W_b = E_0 T L q_0$, leading to an accelerating field reduction [24] (see also references related to the beam loading in the TTF linac [25]) :

$$\Delta E \approx -\frac{\pi f_0 q_0 Z_e}{Q E_0 T} \tag{18}$$

Because $\tau_f \ll \tau_{tr}$, this process can be considered as simultaneous for all AS cells. During the bunch passing a complicated instantaneous field pattern in the AS will be realized. After the first bunch a recovery process will take place. Because $\tau_{tr} \ll \delta t$, traveling wave will pass several times through the AS, smoothing the field pattern and the recovery happens within the natural cavity field rise-time τ_l. But $\delta t \ll 3\tau_l$. The time interval δt is not sufficient to restore the accelerating field amplitude to its starting value with the rf power P_0. The new power set-up point P_1 after the first bunch should be established to have another amplitude E_1 at $t \to \infty$ with the purpose to have E_0 for the next e^+ bunch.
Considering AS rf power balance, one can find:

$$P_1 \approx P_0(1 + \frac{W_b exp(\frac{-\delta t}{\tau_l})}{W_c(1 - exp(\frac{-\delta t}{\tau_l}))}), \tag{19}$$

$$E_0 T = \sqrt{\frac{Z_e P_1}{L}} - \frac{E_0 T W_b}{2W_c} \frac{exp(\frac{-\delta t}{\tau_l})}{(1 - exp(-\frac{\delta t}{\tau_l}))}. \tag{20}$$

For the long PPA sections $\frac{W_b}{W_c} \approx 8.0 \cdot 10^{-2}$ before and $\approx 4.0 \cdot 10^{-2}$ behind the separator. The factor $\frac{exp(\frac{-\delta t}{\tau_l})}{(1-exp(\frac{-\delta t}{\tau_l}))} \approx 3$. For the particular case $\delta t/\tau_l \approx 0.28$ the difference $P_1 - P_0$ is slightly smaller than the beam power gain (see Table 2.4.1). This shows the influence of the stored energy acceleration regime. P_1 is chosen to be $4MW$. $E_0 T$ for each AS was fitted in the beam dynamics consideration taking into account the varying total bunch charge along PPA. For different δt, P_1 should be fitted to have the same $E_0 T$. For this purpose the small reserve in total rf power is foreseen.

4.5 The cavity frequency control

A Cavity Frequency Control System (CFCS) is intended for the AS resonant frequency stabilization during the PPA operation. From the point of view of this system, the PPA consists of four sections with rf power dissipation of $\approx 26kW/m$ and of fourteen sections with rf-power dissipation of $\approx 6.4kW/m$. The parameters of the cavities are given in the table 1. The AS resonant frequency depends on the section dimension and may be varied with the section cooling or heating:

$$\frac{\Delta f}{f_0} = -K_T \Delta T, \quad , \Delta T = T_c - T_0, \tag{21}$$

where T_c is the current temperature, T_0 is the 'resonant temperature' and $K_T = 20kHz/(^oC)$ for the operating frequency $f_0 = 1300MHz$ and uniform heating. In this sense the AS resonant frequency depends on the amount of applied cooling or heating.
The structure of the PPA CFCS is shown in Fig. 4.5.1. The temperature of the first four AS is controlled from one cooling system. The system has two circuits - for 'warm' water (AS cooling) and 'cold' water (technical water to cool the warm water). The individual temperature control for every section is carried out by using mixing valves $CV1 \div CV4$. The temperature of the warm water is stabilized by a heater and the temperature of the cold water is stabilized by changing the water flow trough the cooling machine (CM) by using

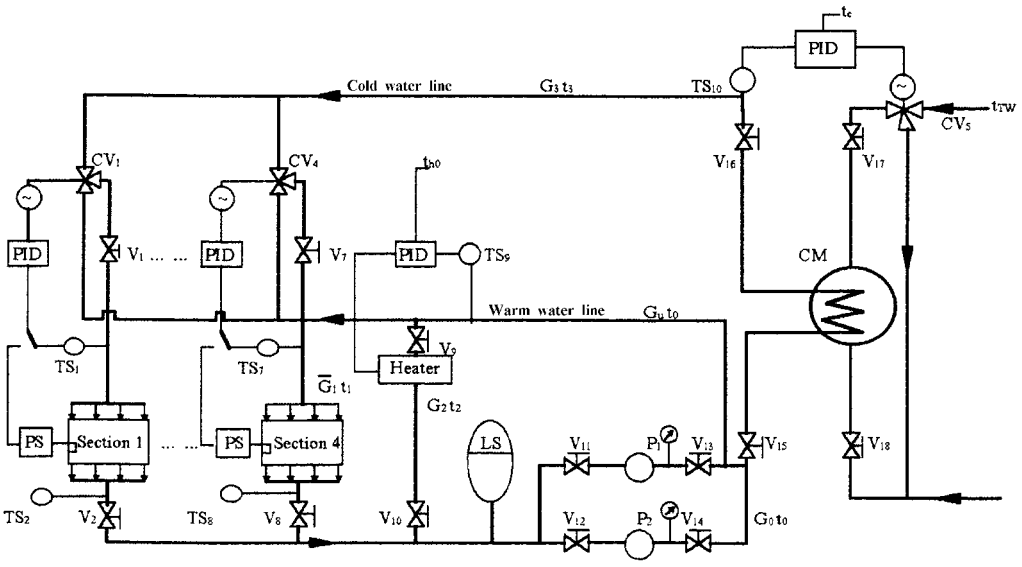

Figure 4.5.1. The scheme of the PPA resonant frequency control system.

the valve CV5. Two pumps (one is for normal operation and one is spare) and a cooling machine provide the required water flow and heat transfer to the cold water into the cooling machine primary water circuit.
The feedback loop regulates the water flow trough the cooling machine by using electrically controlled valves.
The water flow through the AS depends on the cooling channel cross - section and the water flow velocity. The total water flow G through the AS is estimated by:

$$G = \frac{P_d}{1.1\Delta T_{wwc}}, [m^3/h], \tag{22}$$

where P_d is the rf power dissipated in AS, ΔT_{wwc} is the temperature difference between the input and output warm water. The total water flow through the four sections is $G_0 = 16m^3/h$, taking into account additional $4m^3/h$ water flow trough the heater.
The temperature of the cold and the warm water is controlled by means of temperature sensors and PID controllers. The temperature of the cold water depends on the technical water temperature and on the surface of the cooling machine. The required surface S_{cm} of the cooling machine is estimated by using the relation:

$$S_{cm} = \frac{P_d}{K_{cm}\Delta T_{pr}}, [m^2], \tag{23}$$

where K_{cm} is the heat transfer coefficient into the cooling machine, ΔT_{pr} is the temperature difference between cold water and primary (technical) water in the cooling machine. For $K_{cm} = 7800W/(m^{2o}C), \Delta T_{pr} = 2^oC, S_{cm} \approx 4m^2$. For the primary water temperature $T_{prim} = 20^oC$ and $S_{cm} \approx 4m^2$, the minimum cold water temperature is equal to 22^oC. Before the rf power input the warm water temperature depends on the heater power and the characteristic AS time τ_{ASheat} for heating. For the heater power $70kW$ the temperature increase will be $\approx 15^oC$ after $3\tau_{ASheat}$.

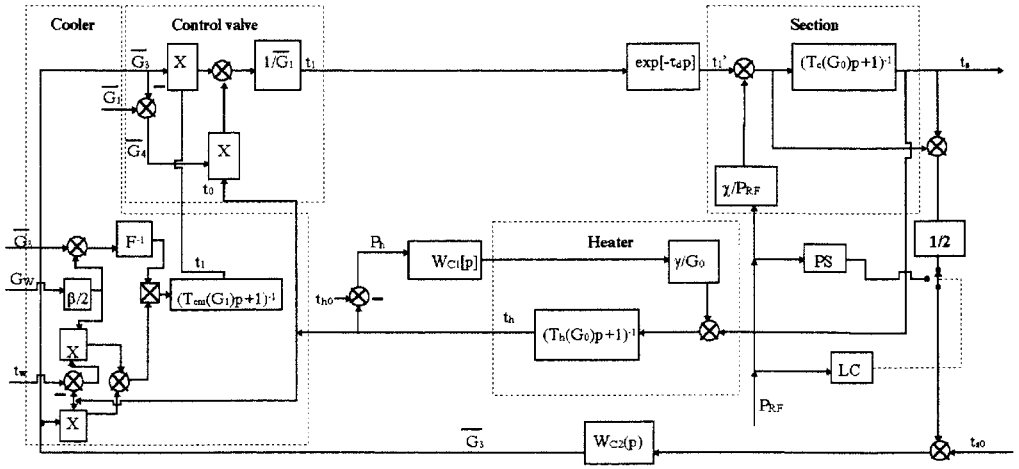

Figure 4.5.2. The functional scheme of the CFCS.

Before the rf power input the AS temperature is stabilized with the help of temperature sensors. Every AS has its own temperature which is put experimentally at the minimal rf power level. In the moment of rf power input the controller has to be switched to the phase sensors. The further regulation is done by means of phase sensors.
The other fourteen AS have similar cooling systems. The AS and the cooling system parameters are listed in Table 4.5.1 for two options of the AS cooling channels (see Paragraph 3.6).
The AS and cooling water system may be described by the relations:

$$\tau_{ASheat}(\overline{G_3})\frac{dT_{AS}}{d\tau} + T_{AS} = \vartheta\frac{\overline{P}}{\overline{G_3}} + T_1^l, \tag{24}$$

$$T_1^l = T_1(\tau - \tau_d)$$

$$T_1 = \frac{\overline{G_3}}{\overline{G_1}}T_3 + \frac{\overline{G_4}}{\overline{G_1}}T_0,$$

$$\overline{G_4} = \overline{G_1} - \overline{G_3},$$

$$\tau_{he}(\overline{G_1})\frac{dT_0}{d\tau} + T_0 = \varsigma\frac{P_{he}}{\overline{G_1}} + T_{AS}^l,$$

$$T_0 = \frac{\overline{G_4}}{\overline{G_0}}T_4 + \frac{\overline{G_3}}{\overline{G_0}}T_3,$$

$$\tau_{cm}(\overline{G_3})\frac{dT_3}{d\tau} + T_3 = \frac{G_3 - \varpi/2G_{tw}}{G_3 + \varpi/2G_{tw}} + \frac{\varpi G_{tw}}{G_3 + \varpi/2G_{tw}}T_{tw},$$

where $\tau_{ASheat}, \tau_{he}, \tau_{cm}$ are the characteristic time values for the AS, the heater and the cooling machine respectively, $T_{AS}, T_1^l, T_3, T_0, T_{tw}$ are the temperatures in the cooling system (see Fig. 4.5.1), τ_d is the water transport time delay and $\overline{G_i} = G_i/4$ for each section.

The functional structure of the CFCS system is shown in Fig. 4.5.2 in accordance with relations (25).
The steady-state AS temperature is:

$$T_{AS}^0 = \vartheta\overline{P}(\frac{1}{\varpi G_{tw}} + \frac{1}{\varpi\overline{G_3}}) + \varsigma P_{he}(\frac{1}{\varpi G_{tw}} + \frac{1}{2\overline{G_3}} - \frac{1}{G_1}) + T_1. \tag{25}$$

Table 4.5.1. Parameters of the CFCS cooling system. Here δT_{1opt} and δT_{2opt} is the average temperature difference between the AS surface and the cooling water for the first and the second chansels scheme design (see Chapter 3.6) respectively.

AS number	1	2	3	4	5	...	18
Rf power dissipated, kW	18	18	18	18	18	...	18
G m^3/h	2.8	2.8	2.8	2.8	2.8	...	2.8
Input-output water temperature difference, ^oC	5	5	5	5	5	... .	5
Heat exchange constant, $W/(m^{2o}C)$	10^4	10^4	10^4	10^4	$4 \cdot 10^3$	... .	$4 \cdot 10^3$
$\delta T_{1opt}, ^oC$	38.5	38.5	38.5	38.5	24	...	24
$\delta T_{2opt}, ^oC$	28.0	28.0	28.0	28.0	18	...	18
Resonant temperature, ^oC	30	30	30	30	30	...	30

The AS resonant frequency is stabilized by the water temperature, using the electronically controlled valves $CV1 \div CV4$. The phase sensors (PS) are used during operation with the design rf power level. For each AS the temperature is stabilized with the help of the PID controllers.
For all AS the operating temperature is chosen to be equal to 30^oC. For long AS with moderate rf power dissipation $\approx 6kW/m$ this temperature can be decreased to $(25 \div 27)^oC$ by increasing the water flow through the AS.
The section cooling system described above is designed to keep the resonant temperature with the accuracy $\delta T_0 \approx \pm 0.1^oC$, corresponding to the phase stabilization precision $\delta\phi \approx \pm(2 \div 3)^o$. The total cooling water consumption is estimated to be equal $\approx 54m^3/h$.

4.6 Summary

The weak beam loading and the lorse tolerances for the rf field amplitude and phase stability in the PPA AS's allow to propose the simpler of the two FeedCS considered above in (A/P) coordinates. The structure of the feedback controller depends on the relationship between τ_l and τ_d in the control loop. The Smith predictor as integrator must be included in the feedback controller. The FeedCS modulator consists of standard rf elements and doesn't need special devices. Only one AS is controlled by the feedback loop. The Cavity Frequency Control System parameters are chosen to keep the field phase shift in the other AS in the required limits. There are special requirements to the AS tuning and TL phase length equalizing.
The possibility to combine rf power from two klystron outputs must be investigated, for the benefit of a significant simplification in the rf power and control systems design.

5 Beam instrumentation

The purpose of the PPA diagnostic system is to provide a sufficient amount of information about the e^+ beam during both linac conditioning and routine operation. The PPA general scheme and beam parameters are described in Chapter 1 and Chapter 8. Essential points

for the PPA diagnostic system are:
- in the first PPA part the main e^+ bunch is accompanied by a subtrain of e^- and e^+ bunches, separated by one half rf period. Moreover, a powerful photon beam exists in the first PPA part.
- in the PPA a complicated magneto-optical device - the separator - exists with the additioanl purpose - to translate the e^+ beam by a distance of 1.3 m.
- the e^+ bunches in the PPA are relatively short ($\approx 100ps$ in the second PPA part).
Differing from diagnostic systems for usual electron linacs, the PPA system for the first part should have a faster response time and provide transparent measurements for the beam intensity and position. For the second PPA part the diagnostic tools may be more or less conventional.
To solve these problems, both well known tools as the Beam Current Transformers (BCT), Buttons PickUps (BPU), Faraday Cup's (FC), Secondary EMission grids (SEM-grid), and, rather new for electron linacs, a monitor for the longitudinal beam profile (longitudinal Bunch Shape Monitor - BSM) are foreseen.

5.1 Monitors for beam intensity and position measurements

In the mixed e^+, e^- bunch of the first PPA part the e^- charge will dominate. The charge measurement therefore is possible for such neutralized bunches in the middle of the first PPA part and on its exit only. With BCTs installed at the exit of the first PPA part and behind the first separator dipole magnet it is possible to measure the e^+ bunch intensity and to adjust the first PPA part (including AMD) parameters. For this purpose it is reasonable to use the transformers ICT BERGOZ [27] or the BCT developed for the bunch charge measurements in LEP. Recent developments [28] show examples of the bunch charge measurements for bunches with time duration $100ps$ and less. The peak pulse amplitudes, proportional to the bunch charges, are measured by using the sampler module [28] (SRS, model SR255) or the digitizer Tectronix SCD5000 with a bandwidth up to 5 GHz [32].
The accuracy for the charge measurements is better than 1% [28] and doesn't depend on the beam position.
For the position measurements at the exit of the first PPA part the application of the BPUs [29] is necessary. It can ensure "transparent" measurements of the position for the short bunches in conditions of large particle losses. The BPU should be protected from direct particle losses and may be installed in places, where the chamber diameter is larger than the regular diameter (like quadrupole lenses).
The beam position measurements are necessary in the beginning and at the end of the first matching section (MS1) before the separator in order to correct beam input in the first bending magnet. Knowing the beam trace up to the first magnet and the pathway behind it, it is possible to evaluate the beam energy after the first PPA part. It is necessary to have BPMs installed in several points in the separator both for commissioning and for routine operation.
The measurements of the position can be done by using nonresonant BPU's, developed for TESLA [29] (in the chamber with radius 39 mm for bunch charge $\approx 8nC$) with a resolution of $\pm 0.1mm$. Such precision is sufficient for BPU application in the PPA.

5.2 The transverse profile measurements

The transverse profile measurements are necessary in the separator and at the exit of the PPA for the definition of both dimensions alone and such parameters as energy spectrum and emittance. As profile monitors both secondary emission multiwire chambers (SEM-grid) and thin metal foils - for the generation of transition radiation (OTR) [30] can be utilized. The most simple and cheap system for the beam profile definition in conditions of large particle losses is a system on the basis of a multiwire SEM-grid. In these monitors are no segments, that are fast aging fast in high radiation fields. It is reasonable to realize a SEM-grid with gear input/output mechanics.
The profile monitors are required for the separator adjustment. The profile monitor behind the third bending magnet is inserted into dispersion plane, so that is possible to evaluate the beam energy spectrum. To adjust the beam into the second PPA part, it is necessary to install a profile monitor after the end of second matching section. Additional profile monitor should be installed at the PPA exit for the profile definition and position measurements of the output beam.
Taking into account, that:
- the beam intensity of the e^+ is large;
- the e^+ beam has large cross-section and, thus;
- the beam density doesn't reaches dangerous a thermal emission limit,
it is easy to see, that a SEM-grid with a thin wire diameter about $20\mu m$, made of tungsten or carbon and a spacing interval between the wires of $2mm$, will disturb the beam parameters only by a small amount. Their reliability and durability are well-known. Methods of data-processing for these monitors are also known. Depending on the problem, both complicated and simple systems can be realized, giving information on the bunch to bunch evolution during a macro-pulse, or measuring the average beam profile [31].

5.3 Transverse emittance measurements

The estimation of the transverse emittance is based on a quadrupole scan and one profile monitor. This method specially often used during linac commissioning [28], [33].
In the PPA case, for the emittance measurement after first PPA part it is necessary to use one lens and one SEM-grid after the fourth bending magnet. This method may also be realized at the PPA exit. To provide the emittance measurements three $800\mu s$ bunch trains are needed.
Because the transfer line after PPA is very long, the beam emittance measurement at the PPA exit might better be realized by three profile measurements with three SEM-grids in the transfer line. For this method only one bunch train is needed, allowing to provide "on-line" measurements.

5.4 The energy and energy spectrum measurement

The measurements of the e^+ bunch energy and energy spectrum is made at the PPA exit by means of a special measuring station. The station consists of a collimator and a spectrometer with dipole magnets.
The estimations shows, that the time-of-flight method for the beam energy and energy distribution measurements is not the best option, because for a e^+ beam energy of $\approx 250MeV$

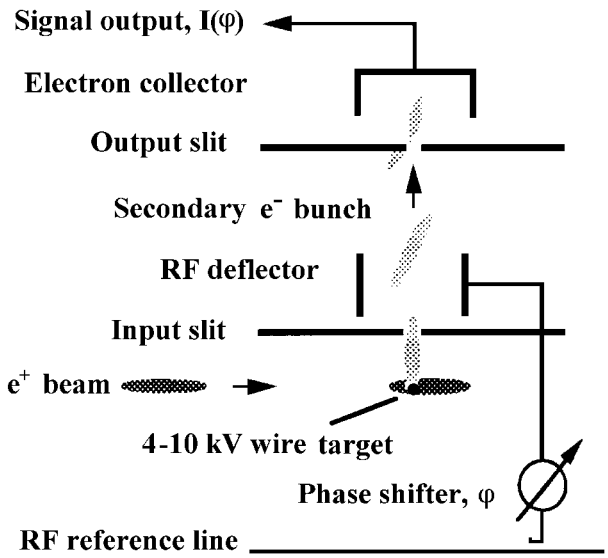

Figure 5.5.1. The scheme of the beam shape monitor.

the drift length appears too large ($\approx 300m$) and the intensity is too small to obtain the required accuracy.
The spectrometer may consist of two lenses, which are arranged up to dipole magnet and reshape a beam before a magnet from collimated beam, dipole magnet and focusing lens after the magnet. In the focal plane of the last lens it is possible to observe the spectrum of the beam. Such schemes are used for positron beams, for example in [32]. The results of the spectrometer are described for a spectormeter consisting of a pulse dipole magnet, turning the e^+ beam by a small angle, and DC dipole magnet, turning the e^+ beam by $\approx 60^o$. The SEM-grid monitor is placed in the focus of the spectrometer. The resolution of the spectrometer for positrons is $\delta E/E = \pm 0.18\%$ (for conditions described in [32]). Such scheme at the PPA exit allows additionally to provide precise bunch charge measurements by means of a Faraday Cup.
At the first PPA part exit, the estimation of the energy distribution is made in the separator with the help of the profile sensor installed in the plane with high dispersion, and an estimation of the beam energy can be done with the help of BMPs, installed behind the first separator dipole magnet.

5.5 Longitudinal profile and bunch duration measurements

In comparison to expensive streak cameras, it is more easy and cheaper to use for this purpose a longitudinal Bunch Shape Monitor based on the wire probe [33] (Fig. 5.5.1). The thin wire probe has a potential of $(4 \div 10)kV$. The positron beam beats out secondary electrons, which are accelerated in the field of the wire probe. The secondary electron bunches pass through the first slit in the vacuum chamber wall, and are accelerated in the high frequency field of the deflector. The secondary beam also goes through the next slit onto the collector. Depending on the scanning field phase, different parts of the secondary bunch come to the collector. The output signal is proportional to the longitudinal particle distribution in the

primary e^+ bunch. This monitor should be installed at the PPA exit behind the collimator.

5.6 The PPA beam parameters measurement system

All beam monitor subsystems, described above, are integrated into the joint PPA beam monitoring system. The main part of the devices described above are useful during linac commissioning. During routine operation not so many tools are needed.
Two BCTs in the first PPA part are accounted for measurements of the charge of the mixed e^+, e^- bunches. Signals from these transformers are processed by high frequency electronic devices, which allow to measure the peak amplitude of very short signals (sampler SR255 or newer and better). These two transformers give the beam intensity in the middle and at the exit of the first PPA part.
Two similar devices (without rigid requirements for fast data processing) are installed before and behind the second PPA part. It is very useful, that BERGOZ manufactures not only BCT's, but also a standard set of equipment as preamplifiers with generators for calibration signals for the transformers [27].
Absolute measurements of the e^+ charge (during commissioning) are made by a FC, arranged behind the first spectrometer magnet. The FC design for an e^- beam with an average current of $50\mu A$ and an energy of $1GeV$ is given in [34]. For the PPA parameters a similar FC design may be simpler and cheaper.
The beam position monitors (BPMs) are installed in the insertion (first and second matching parts), in the separator, and in some places of the second PPA part. BPMs should be designed on the basis of "buttons" with a diameter of $(10 \div 15)$ mm. In the separator the area of the "buttons" is increased, because the separator vacuum chamber is larger than the regular chamber.
Both BPMs and BCTs are protected from direct particles losses by placing them at positions with enlarged chamber diameter.
The beam profile monitors are installed behind the separator banding magnets to estimate the transverse distribution, energy distribution and emittance before the second PPA part entrance. At the PPA exit three SEM-grids are installed to provide 'on-line' emittance measurements.
The beam collimator is introduced before the energy spectrometer and the BSM. The energy spectrometer has an additional beam profile monitor.
For longitudinal bunch length measurements by means of the BSM, it is placed at the PPA exit.
The PPA beam monitors are mainly clustered on two sites:
- the insertion (including separator), to measure and adjust the main parameters of the first PPA part, to trace the beam through the separator, to control the e^+ collimation and the beam parameters before the second PPA part;
- at the PPA exit, to measure the output beam parameters.
The scheme of the recommended beam monitor arrangement is shown in Fig. 8.1, and the list of the sensors is collected in Table 5.7.1.
The space along the beam axis to place the BPMs, SEM-grids and BCTs doesn't exceed $\approx (10 \div 18)cm$. All of them may be easily placed along the PPA.

Table 5.7.1 The list of the sensors for the PPA beam diagnostics system (including PPA commissioning).

Monitor	Quantity	Placement	Designation
BCT-1	2	in the middle of the first PPA part	fast charge measurements for mixed e^+, e^- beam.
BCT-2	2	2nd PPA part entrance PPA exit	e^+ charge measurements
FC	1	1st spectrometer magnet exit	precise e^+ charge measurements
BPM	$\approx 15 \div 25$	insertion 2nd PPA part	beam center position measurements
SEM-grid	6	insertion PPA exit spectrometer	beam size and position, emittance measurement, energy distribution.
BSM	1	PPA exit	bunch shape and length measurements.
Spectrometer	1	PPA exit	energy distribution measurements.

6 Focusing elements

For the positron beam focusing in the PPA both elements with longitudinal magnetic field (the solenoid in first PPA part), and with transverse fields (quadrupole lenses in the matching parts, separator, triplets of the second PPA part) are used. Below the proposal both for the solenoid and for quadrupole lenses are considered. All numerical simulations have been performed by using POISSON-SUPERFISH code.

6.1 Solenoid

The accelerating sections (AS) of the first PPA part are placed inside a solenoid, limiting the inner solenoid diameter to $\approx (230 \div 240) mm$. Because the PPA acceptance $A_{ac} \sim B$ and the DC power P_{dc} required to provide the inductance B is $P_{dc} \sim B^2$, one can see $P_{dc} \sim A_{ac}^2$. Attempts to increase A_{ac} by B leads to a fast increase of the required power.
Basing on the results of the beam dynamics study (see Chapter 1) and preliminary estimations of the solenoid design and DC power consumption, a compromise value of $B = 0.24T$ has been chosen. This value is lower than for the focusing solenoid of the KEK positron generator ($0.4T$) [26], confirming the realistic value for our proposal.
Due to technical reasons, we can not accept a continuous 11 m long solenoid with the 4 short ASs and 4 long ASs inside. Consideration of possible solenoid designs leads to the proposal, shown in (Fig. 8.2) together with the ASs.
The solenoid consists of separated sections. Each section has its winding and a magnet screen made of low-carbon steel. For every AS two solenoid sections are required and the total number of sections is 16. To close the gaps for the magnetic flux, screens of adjacent sections are connected with low-carbon steel plates. The space between the plates is intended for AS supports, rf input, cooling water tubes and other connections. To compensate the lower magnetic field in the gaps between the sections, the windings near the section ends

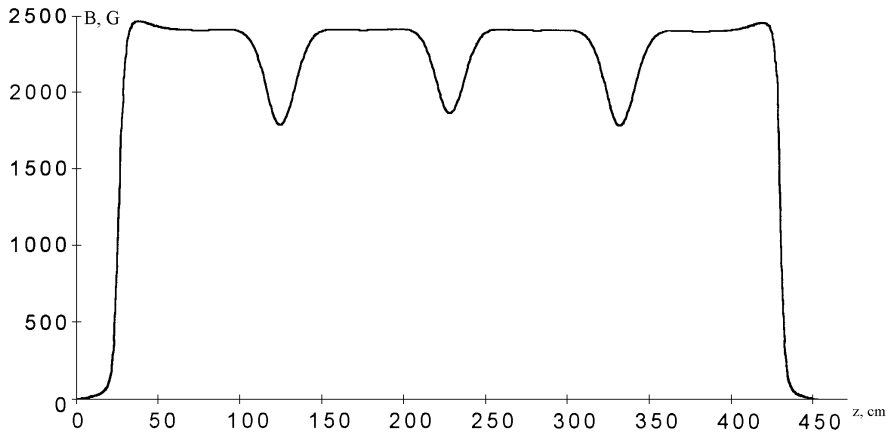

Figure 6.1.2. The magnetic inductance distribution along axis without correction.

Table 6.1.1 The basic parameters of the long solenoid section

Parameter	**Unit**	**Value**
Outer diameter	mm	500
Inner diameter	mm	250
Length	mm	920
Inductance	G	2400
DC power	kW	39
Current	A	480
Cooling water	m^3/h	2.4
δt, water cooling	^oC	16.5

have an enlarged number of turns.

Each section is assembled out of separate "pancakes" with screens. "Pancakes" are wound with a copper conductor with an internal channel for cooling water. For DC power "pancakes" inside one section are connected in series. For cooling "pancakes" are collected in groups. Inside one group the cooling channels are in series, groups are connected to the cooling system in parallel through alumina-ceramic insulators.

Two solenoid sections are connected electrically in series and powered by one DC power supply.

Parameters for one section of the solenoid for a long AS are listed in Table 6.1.1 The example of the B_z distributions along the solenoid axis is shown in Fig. 6.2.2 without correction of number of turns near the section ends. One sees $\approx$ 20% "pits" in the gaps between the sections. In the case of a strong influence on the e^+ beam dynamics, these B_z decreasing may be corrected "in average" by additional turns.

The total DC power and cooling water consumption for the solenoid are $450kW$ and $27m^3/h$, respectively.

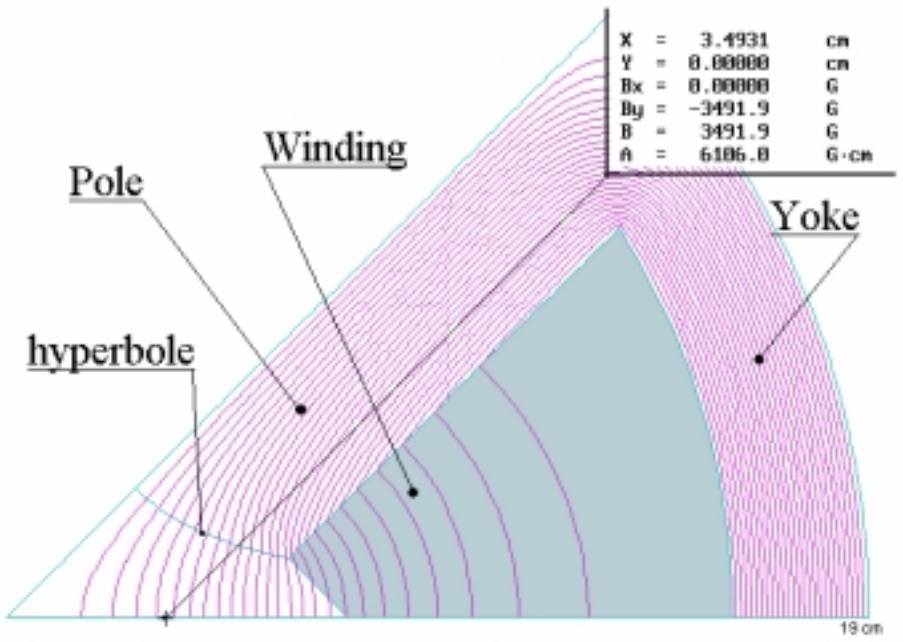

Figure 6.2.1. The pole profile and magnetic inductance distribution in the quadrupole for the second PPA part.

6.2 Quadrupole lenses

In the second PPA part identical triplets are used. The triplet consists of three identical (20 cm in length) quadrupoles. The distance between the quadrupoles is equal to $12cm$. The field gradient in central quadrupole is twice larger as the gradient in the outer quadrupoles. The gradient of the magnetic field in the central lenses varies along the PPA from $G = 0.4kG/cm$ at the entrance to $G = 1.0kG/cm$ at the exit. The basic parameters for the central and the adjacent quadrupoles are listed in Table 6.2.1 The pole profile together with the magnetic field lines are shown in Fig. 6.2.1.

The total DC power and cooling water consumption for the focusing elements in the second PPA part are $35kW$ and $3.6m^3/h$ respectively.

For the quadrupole lenses for the matching parts and the $e^+ - e^-$ separator focusing gradients $G < 0.7\,kG/cm$ and an aperture diameter $\geq 12cm$ are required. The magnetic inductance at the pole tip is so high, that a special lens design is required. In order to avoid saturation in steel, the pole width is enlarged near the the yoke. The cooling circuits of the coils are connected in parallel to lower the temperature. The basic parameters of the quadrupole lens are listed in Table 6.2.1. The pole profile together with the magnetic field lines are shown in Fig. 6.2.2.

The total number of quadrupoles in the matching part and the separator is 24. The total DC power and cooling water consumption are estimated for this group as $\approx 130kW$ and $4.7m^3/h$ respectively.

The poles of all lenses have a hyperbolic contour, resulting in a good performance of the focusing field (see Table 6.2.2).

Table 6.2.1. The basic parameters of the quadrupole lenses for the second PPA part and the matching part including the separator.

		Triplets		**Matching**
		Central	**Adjacent**	
Parameter	unit	value	value	value
Outer diameter	mm	380	380	800
Aperture diameter	mm	80	80	120 (150)
Length	mm	200	200	250 (400)
Gradient	kG/cm	1.0	0.5	0.7
DC power	kW	2.9	0.73	5.4 (6.4)
Voltage	V	6.3	3.15	8.9
Current	A	465	465	607
Conductor	mm^2	8.5x8.5	8.5x8.5	8.5x8.5
Turns per pole		14	14	17
Cooling bore diametermm^2	5.3	5.3	5.3	
Cooling consumption	m^3/h	0.14	0.035	0.19 (0.23)
δt cooling	^oC	18	18	24.6

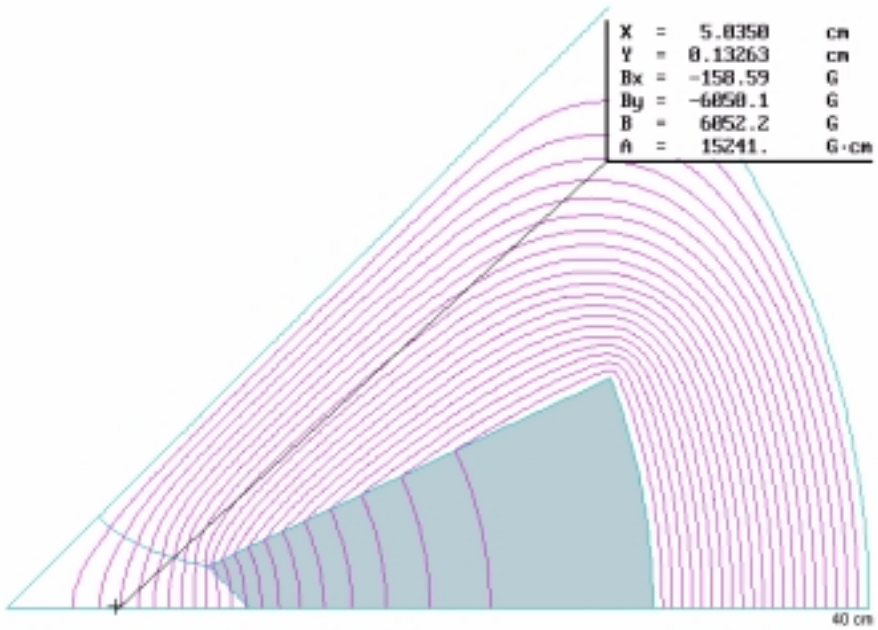

Figure 6.2.2. The pole profile and magnetic inductance distribution in the quadrupole for the matching and separator sections.

Table 6.2.2. The amplitudes for spatial harmonics of the magnetic field, r_m is the reference radius.

$$B_x - iB_y = i\sum \frac{n(A_n+iB_n)}{r_m}(\frac{r}{r_m})^{n-1}$$

	Triplet	$r_m = 4.0cm$	**Matching**	$r_m = 6.0cm$
n	nA_n/r	nB_b/r	nA_n/r	nB_n/r
2	$4.0051 * 10^3$	0.0000	$7.2160 * 10^3$	0.0000
6	-6.0909	0.0000	-7.9651	0.0000
10	-5.5527	0.0000	-6.1076	0.0000
14	-2.0103	0.0000	-8.6565	0.0000

6.3 Summary

The proposal for the solenoid design is close to an already realized design of the solenoid [26], differing in only in an extended length and a larger inner diameter. A careful study of the influence of the "pits" in the magnetic field distribution on the e^+ dynamics is required. The quadrupole lenses in triplets have low gradient. The quadrupole in the matching parts the and separator have a high gradient and the pole profile is chosen to have $B_{max} \leq 13kG$, below the saturation of low-carbon steel. During the technical design the operational conditions - high level of particle losses and x-ray radiation - should be taken into account to chose proper materials. Following present technology, manufacturing of the focusing elements will not cause serious problems.
The total consumption of the magnet system is $\approx 610kW$ DC power and $\approx 34m^3/h$ cooling water, the largest contribution of a system to the total PPA budget. (The DC power consumption for the separator bending magnets is not yet estimated). Comparing the DC power for the solenoid ($450kW$) and for all triplets in the second PPA part ($35kW$, even though this part is twice as longer) the efficience of the quadrupole focusing is seen.

7 Vacuum system

The PPA vacuum system, like the rf system, should basically use standard TESLA equipment, taking into account the PPA particularity of a room-temperature linac. Below one possible solution for the PPA vacuum system is described.
The total system consists of three parts, separated by DN63 gate valves (see Fig. 8.1). The first part, from the PPA beginning to the separator, includes 4 short and 4 long accelerating sections (AS). The second part includes vacuum equipment of the separator. The third part includes 10 long sections, from the separator to the PPA end.
To estimate the gas flow and the necessary conductance of the vacuum elements an outgassing rate of $1.33 * 10^{-6} m^3 Pa/sm^2$ for the cleaned and outgassed copper surface was used. The gas flow was estimated to be equal to $\approx 1.0 * 10^{-6} m^3 Pa/s$ for the short AS and to $\approx 3.8 * 10^{-6} m^3 Pa/s$ for the long sections. Due to the large aperture opening ($S \approx 21cm^2$), the AS vacuum conductivity is sufficient to pump, both long and short AS at one point.
The operating pressure of each of the three parts is obtained in two steps:
- Preliminary pumping by using a Leybold-Heraus movable pumping station. The station includes a rough pump with a pumping speed of $0.25m^3/s$ and a turbomolecular pump of $0.1m^3/s$. The station can be connected to the vacuum system via a manual valve installed

at one of the RF waveguides.
- The normal operational vacuum is obtained with the titan sublimation pumps with a pumping speed of $0.25 m^3/s$ for the long and $0.1 m^3/s$ for the short AS. The pumps are connected to the RF waveguides in the vicinity of the AS. The number of pumps is equal to that of the accelerating sections.
To pump the separator two discharge titanium pumps are used. They are located 4 m and 8 m away from the separator beginning.
To provide vacuum measurements Pirani and Penning gauges, installed at the RF waveguides, are used.
The PPA vacuum system is similar to that of existing proton linacs, and a normal operating pressure of $(5 \div 10) * 10^{-6} Pa$ seems not to be problem.

8 General layout and space requirements

The generalized PPA scheme is shown in Fig. 8.1. The total accelerator length is $\approx 60m$. It is acceptable taking into account the long distance to the main accelerator. This length allows to place klystrons and pulse transformers in line along the PPA. Assuming $\approx 6m$ space per each klystron and pulse transformer together with auxiliary connectors, the space for the nine rf channel lines is sufficient with reasonably short transmission line from the klystron to the accelerating sections.
The transverse PPA dimensions are also small. In Fig. 8.2 the proposed scheme for the PPA beginning is presented showing $\approx 0.6m$ diameter for the solenoid. For the second PPA part the triplet lenses also have transverse dimensions $\approx 0.5m$. So, the PPA can be easily placed in the standard TESLA tunnel. The beam instrumentaion equipment, like the energy spectrometer at the PPA exit should be discussed additionally.
The most power consuming PPA systems are the focusing ($\leq 610kW$ DC power) and the rf system ($360kW$ average rf power). The total DC+AC power consumption of the PPA may be estimated as $\approx (1.3 \div 1.5) MW$ and should be defined correctly during the technical design.
The cooling water consumption (without klystron cooling) is $\approx 90 m^3/h$.

9 Conclusion

In this report the results of the conceptual design study of a Positron Pre-Accelerator for the TESLA Linear Collider are presented. The special results for each topic are presented in Summary's for each Chapter.
The main result of the study is the proposal of a flexible and effective linac scheme for the PPA with a capture efficiency of $\approx 22\%$ with technically reasonable system parameters and reasonable and cost effective solutions.
The mainl points of the PPA proposal are:
- The PPA is standing wave L-band linac. The SW structure applications leads to a higher flexibility and allows to combine the required beam performance with a cost saving problem solution. With the AS aperture diameter increased to $52mm$ the SW PPA has a strongly enlarged acceptance in comparison with the TW PPA and reduced power consumption.
- An important PPA part is the insertion (including the separator) which allows to solve the beam separation and collimation problems and the separation of the powerful photon beam.

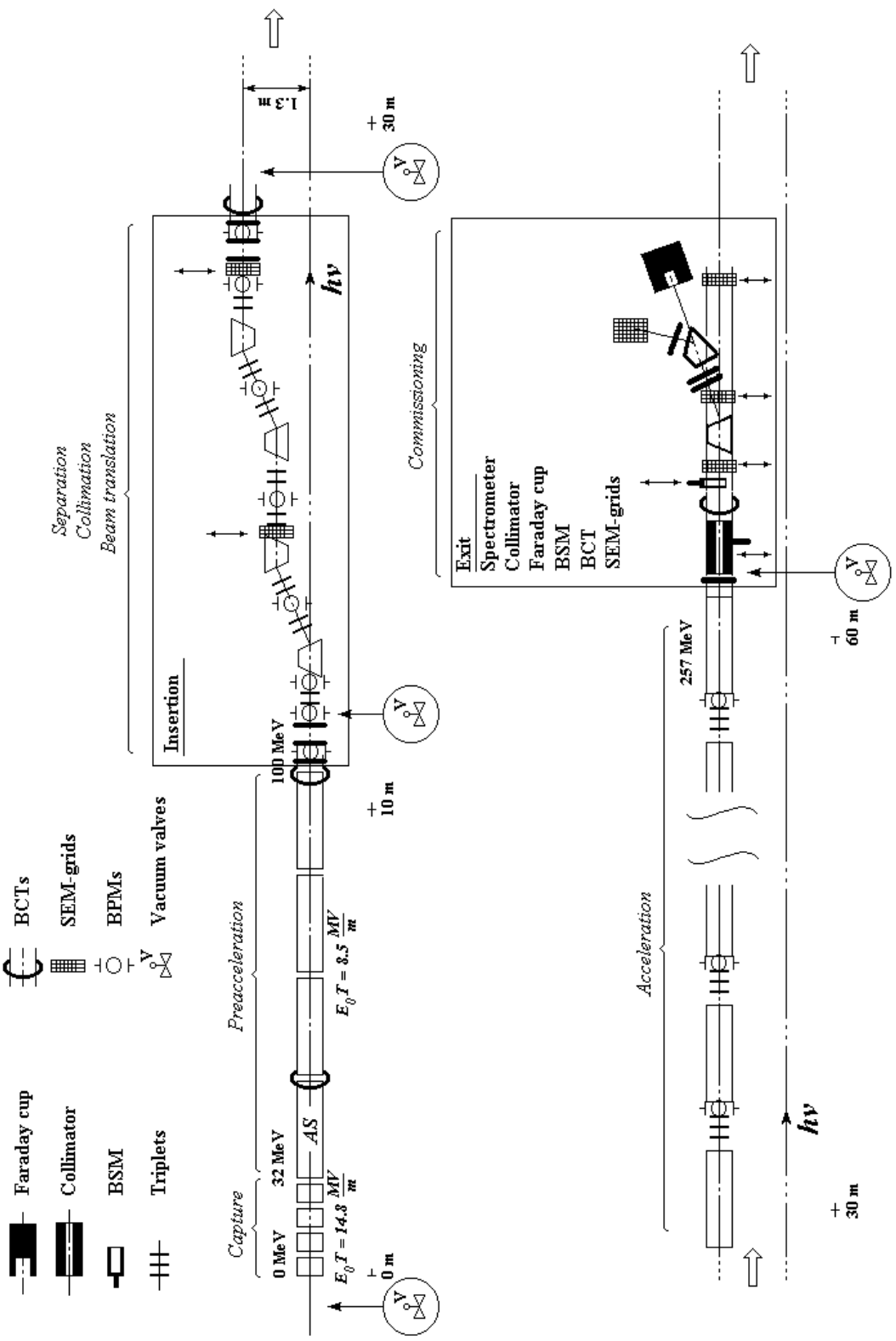

Figure 8.1. The general PPA scheme.

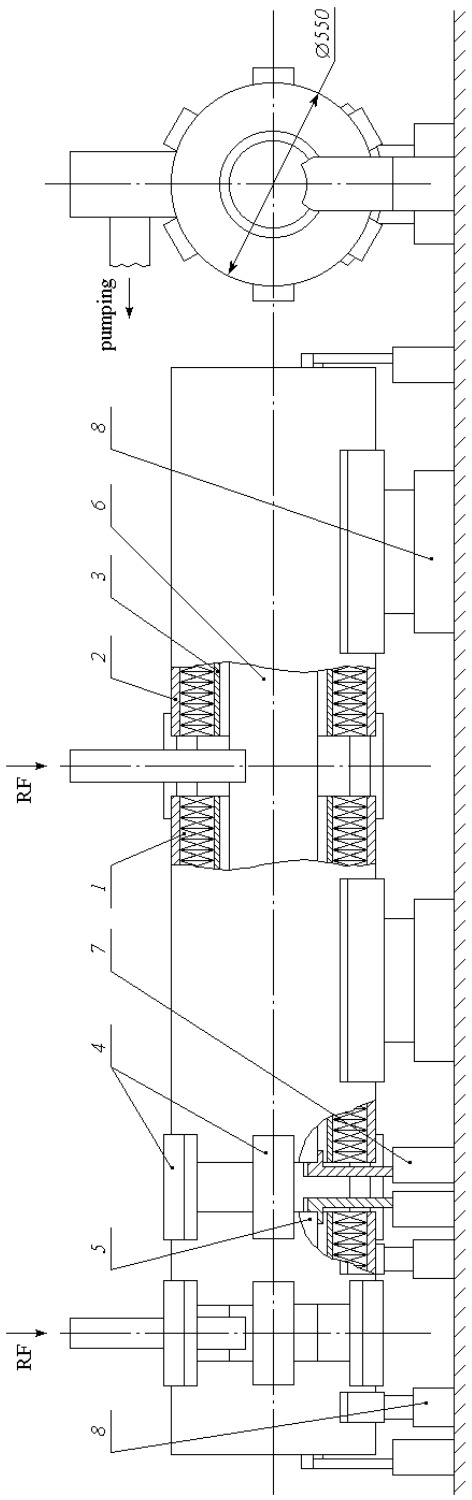

Figure 8.2. The proposed scheme for the design of the PPA beginning. 1- 'pancake' in the solenoid, 2- yoke, 3- support, 4- lowcarbon steel plate, 5- short AS, 6- long AS, 7- AS position adjustment, 8- solenoid adjustment.

Additionally, the insertion allows design the second PPA part as usual, simplifying the PPA commissioning, tuning and operation.
- The triplet focusing scheme is chosen for the second PPA part to reduce the DC power consumption.
- The moderate values both for the accelerating field and the focusing fields (except in the PPA beginning) are chosen to reduce the power consumption and expensive hardware requirements.
The present results clarify the main problems to be solved before the technical design phase:
- A PPA beam dynamics study taking into account nonlinear effects should be performed due to the wide energy spread of the PPA beam.
- A beam dynamics study should be performed for the total positron line from the target to the damping ring to optimize the solutions. Further e^+ beam parameter improvement may be realized in this way.
- An investigation of the possibility to combuine the rf power from the two outputs of the TESLA standard klystron is strongly desirable, leading to simplifications in the rf and control systems.

References

[1] Conceptual Design of a 500 GeV e^+e^- Linear Collider with Integrated X-ray Laser Facility. DESY 1997-048

[2] V.E. Balakin, A.A. Mikhailichenko, The conversion system for obtaining high polarized electrons and positrons. Preprint INP 79-85, 1979.

[3] K. Flöttmann. Investigations toward the development of polarized and unpolarized high intensity positron sources for linear colliders. DESY 93-161, 1993.

[4] V.A.Moiseev, P.N.Ostroumov, Code to Study the High Intensity Beam Dynamics in the Ion Linear Accelerators, Proc. of the VI European Particle Accelerator Conference (EPAC-6), Stockholm, Sweden, pp.1216-1217, 1998.

[5] M.F.Tautz, Magnet Systems for the Transport of Ion Beam with no Change in Properties, Nuclear Instruments and Methods, Vol.92, pp.263-268, 1971.

[6] K.G.Steffen, High Energy Beam Optics, Interscience publishers, New York, 1965.

[7] Recenet Technological Development in Accelerating Structures. Proc. of the 1992 Linac Conf., p.580, 1992

[8] V.V. Paramonov, The Cut Disk Structure for High Energy Linacs, Pros. 1997 PAC, v.3, p. 2962. 1998.

[9] O.A. Valdner et al., Disk Loaded Waveguides. Handbook, Atomizdat, 1997 (in Russian)

[10] Compendium of Scientific Linacs, CERN/PS 96-32, 1996

[11] Linear Accelerators, Ed. P. Lapostole, A. Septier, North-Holland Pub. Comp., 1970

[12] J. Billen, Smooth transverse and longitudinal focusing in high intensity ion linacs. Pros. 1996 Linac Conf., v. 2 p. 587, CERN 96-07.

[13] T. Kroc et al. Continued conditioning of the Fermilab 400 MeV linac high-gradient side-coupled cavities. Proc. 1996 Linac Conf., v. 1, p.338, CERN 96-07, 1996.

[14] H.A. Hoag et al. High-field capture section for SLC positron source. SLAC-PUB-3971, 1986 (A)

[15] V.F. Vikulov, V.E. Kallyuzhny, The influence of manufacturing errors on parameters of standing wave accelerating structures, Journal of technical physics, V. 50, n4, p. 773, 1980

[16] J.-P. Labrie et al. A high-power efficient L-band structure. Proc. 1988 Linac Conf., p. 273, 1988

[17] J.-P. Labrie, Power handling capability of water cooled cw linac structures. Nuclear Instruments and Methods, A 247, p.281, 1986

[18] Injector linac for MAMI microtron. Proc of EPAC'88, Rome, pp. 997 and 1149.

[19] V.V. Paramonov, L.V. Kravchuk, V.A. Puntus, The cold model of the CDS structure, Proc. 1998 Linac Conference, Chicago, USA, (to be published).

[20] I.V. Gonin et al, Some Methods of the Stop-band Width Evaluation in Compensated Accelerating Structures, IEEE Trans. , NS-32, n.5, p. 2818, 1985

[21] Y. Morozumi et al., Multy-cell bridge cavity. Proc. 1990 Linac Conference, p.153, 1990
V. Paramonov et al., Rectangular directly coupled bridge cavities. Proc. 1998 Linac Conference, (and related references) (to be published).

[22] F. Pedersen, Beam loading effects in the CERN PS booster. IEEE Trans. Nucl. Sci., NS-22, p. 1906, 1975

[23] A.I. Kwasha et al., Fast accelerating field stabilization systems for the Moscow meson facility linac accelerating cavities. Los Alamos, LA-TR-77-93.

[24] P. Wilson, Transient beam loading in electron-positron storage rings, CERN-ISR-TH/78-23, 1978

[25] D.A. Edwards (ed.), TESLA Test Facility Linac - Design Report, DESY-TESLA-95-01, 1995.

[26] A. Enomoto et al. Performance of the Upgrated Positron Generator at KEK. Proc. of the 1992 EPAC Conference, 1992, p. 524.

[27] BERGOZ information list, 1995.

[28] M.E. Biagini, et al, Overview DAFNE Beam Diagnostics, Proc. EPAC-94, London, p. 1503.
K.B. Unser, Measuring Bunch Intensity, Beam Loss and Bunch Lifetime in LEP, Proc. EPAC-90, Nice, France, p. 786.

[29] K. Yezza, et al., Beam Position Monitor Developments for TESLA, Proc. EPAC-94, London, p.1533.

[30] M. Bernard et al., The TESLA Test Facility Linac Injector, Proc. EPAC-94, London, p. 692.

[31] N. Il'insky et al., Transients in Linac and Beam Fast Measuring System, Proc. EPAC-94, London, p.1708.

[32] S. Kramer et al., Bunch current measurements in VUV light source. Proc. EPAC-94, London, p. 1696.

[33] A.V. Feschenko et al., Bunch Shape Monitor for DESY H^- Linac, Proc. PAC-97, Vancouver, Canada, p.2078.

[34] J.Shaw et al., A High Power Faraday Cup to Measure Extracted Beam Current from the Bates South Hall Ring, Proc. PAC-97, Vancouver, Canada, p. 2274

[35] K. Flöttmann et al., Travelling wave positron injector linac for TESLA, TESLA 99-03, DESY, 1999

[36] V.V. Paramonov, The data library for accelerating structures development. Proc. of the 1996 Linac Conference, CERN 96-07, v.2, p493.

[37] I.V. Gonin et al, 2D codes set for rf cavities design. Proc. of the 1990 EPAC Conference, 1990, p 1249

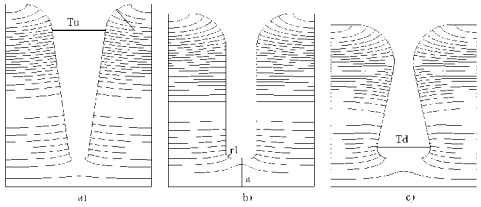

Figure A1: Geometry definition for different shapes of the DLW cells.

10 Appendix A: Optimization of the accelerating structure

The shape of the DLW cells and the shape of the standing wave structures have been optimized in 2D approximation to study the behaviour of the parameters. The procedure of such an extensive wide-range optimization is described in [36].

DLW cells optimization

The shape of the DLW cell may be described with five independent parameters:
- aperture radius a;
- lower web thickness T_d;
- upper web thickness T_u;
- lower web circular radius r_1;
- upper web circular radius r_2.

The cell radius R_c should be adjusted to set the resonant frequency. The ranges for parameter changes during optimization are:
$a = (5.0 \div 30.0)mm$, six steps;

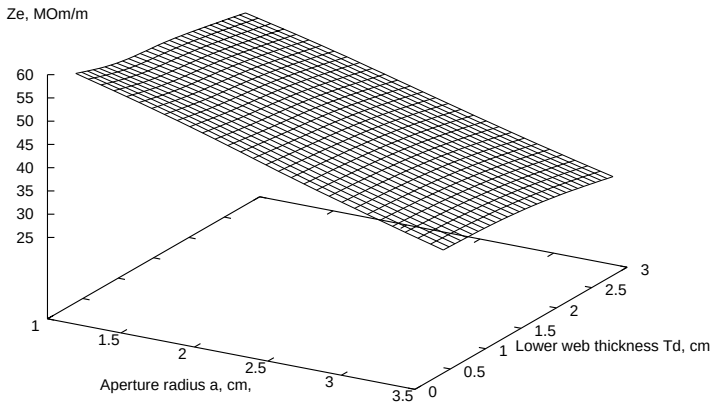

Figure A2: The surface $Z_e(a, T_d)$ for a DLW with $r_1 = 0.3cm, T_d = 1.2cm$

$T_d = (4.0 \div 28)mm$, five steps;
$T_u = (4.0 \div 28)mm$, five steps;
$r_1 = (0.2 \div 1.0)T_d$, five steps;
$r_2 = (0.2 \div 1.0)(R_c - a - 2r_1)$ or $(0.2 \div 1.0)(L - T_u)$, five steps.
As one can see from Fig. A1, this set of parameters allows to consider a large variety of DLW cell shapes with a wide range of dimensions.
By means of a very powerful set of 2D codes [37], the DLW cells (totally $6 \cdot 5 \cdot 5 \cdot 5 \cdot 5 = 3750$) were calculated with an automatic tuning of the $2\pi/3$ mode frequency to 1300.0 MHz. For each variant all important DLW parameters have been stored.
The resulting data library may be considered as five-dimensional cube. Then, by neans of an interpolating procedure with cubic spline algorithm, one can consider different DLW realizations with different limitations. For example, with the specification $E_{smax} \leq E_{fixed}, T_d \geq T_{dfixed}$ (for cooling) $a = const$ or $a \geq a_{fixed}, P_{inp} = P_{fixed}$, one can find the best solution with respect to Z_e for a constant gradient DLW section with cell dimensions within the limits. During this search with the interpolation all cell dimensions may vary in an attempt to find the best solution. Such an optimization provides better results as the usual optimization "by hand". (The simultaneous change of the aperture radius and the iris thickness to find the required β_g with a minimal Z_e reduction for a constant gradient DLW section was done in [35]). Results (examples) of such an optimization for different DLW options are given in Tables A1 - A3. The short parameter list in Table A3 means, that within the frame of the specified dimensions it is not possible (for the specified conditions) to find a solution for a DLW cell with a large aperture of $a = 20mm$ and a high accelerating gradient of $E_0T = 15MV/m$. There are no cells with the required small value of β_g.

Another useful possibility of this approach is in the presentation of the general behaviour of the parameters. For example the two dimensional surfaces $Z_e(a, T_d)$ and $\beta_g(a, T_d)$ are shown in Fig. A2 and Fig. A3, respectively.

Table A1: DLW section parameters (21 cells) for
$E_0T = 15MV/m, a = 15.0mm, P_{inp} = 7.26MW$. Total attenuation $\alpha_t = 1.25Np$.

N	T_d	r_2	T_u	R_c	P_{tr}	α	Q	β_g	Z_e	P_s
	mm	mm	mm	mm	MW	Np/m	$*10^{-3}$		$M\Omega/m$	kW
1	8.32	32.35	12.16	96.05	7.26	0.0224	22.61	0.00207	53.19	325.14
2	8.32	32.35	12.16	95.90	6.93	0.0234	22.63	0.00198	53.47	323.44
3	8.80	32.35	12.16	95.86	6.61	0.0246	22.58	0.00189	53.37	324.05
4	9.28	32.35	12.16	95.80	6.29	0.0258	22.53	0.00180	53.28	324.61
5	9.28	32.36	12.16	95.64	5.96	0.0271	22.56	0.00171	53.57	322.85
6	9.76	32.35	12.16	95.56	5.64	0.0287	22.51	0.00162	53.53	323.10
7	10.24	32.36	12.16	95.46	5.32	0.0305	22.47	0.00153	53.51	323.24
8	10.72	32.36	12.16	95.36	4.99	0.0324	22.42	0.00144	53.48	323.42
9	11.20	32.36	12.16	95.22	4.67	0.0347	22.38	0.00135	53.50	323.28
10	11.68	32.36	12.16	95.09	4.35	0.0371	22.35	0.00126	53.52	323.15
11	12.16	32.36	12.16	94.92	4.02	0.0402	22.32	0.00117	53.61	322.62
12	12.64	32.36	12.16	94.74	3.70	0.0436	22.29	0.00108	53.70	322.06
13	13.60	32.36	12.16	94.54	3.38	0.0478	22.19	0.00099	53.57	322.85
14	14.56	32.36	12.16	94.30	3.06	0.0529	22.10	0.00090	53.49	323.32
15	15.52	32.36	12.16	94.02	2.73	0.0593	22.03	0.00080	53.49	323.34
16	16.48	32.36	12.16	93.71	2.41	0.0672	21.95	0.00071	53.54	323.05
17	17.92	32.36	12.16	93.32	2.09	0.0778	21.82	0.00062	53.36	324.15
18	19.36	32.36	12.16	92.88	1.76	0.0924	21.69	0.00052	53.26	324.74
19	21.28	32.36	12.16	92.29	1.44	0.1139	21.50	0.00043	52.96	326.58
20	24.16	32.36	12.16	91.32	1.11	0.1489	21.18	0.00033	52.17	331.53
21	27.52	29.25	12.16	89.05	0.78	0.2191	20.63	0.00023	50.39	343.23

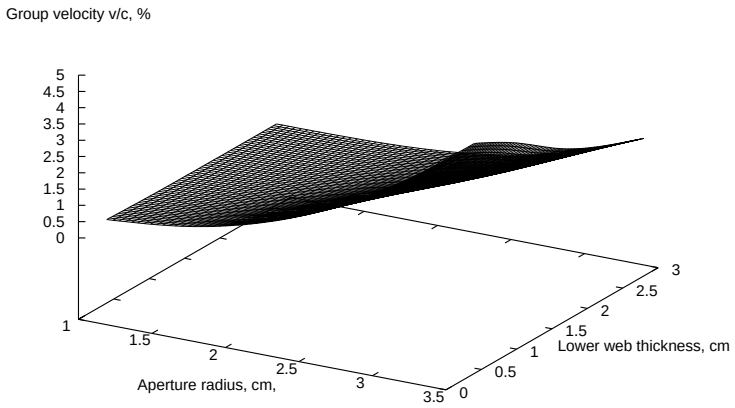

Figure A3: The surface $\beta_g(a, T_d)$ for a DLW with $r_1 = 0.3cm, T_d = 1.2cm$

Table A2: DLW section parameters (21 cells) for
$E_0T = 12MV/m, a = 15.0mm, P_{inp} = 7.26MW$. Total attenuation $\alpha_t = 0.45Np$.

N	T_d	r_2	T_u	R_c	P_{tr}	α	Q	β_g	Z_e	P_s
	mm	mm	mm	mm	MW	Np/m	$*10^{-3}$		$M\Omega/m$	kW
1	4.48	32.36	12.16	96.86	7.26	0.0144	22.94	0.00317	53.13	208.33
2	4.48	32.35	12.16	96.68	7.05	0.0147	22.98	0.00310	53.34	207.51
3	4.96	32.36	12.16	96.70	6.84	0.0153	22.91	0.00300	53.23	207.96
4	4.96	32.36	12.16	96.56	6.64	0.0156	22.94	0.00294	53.39	207.32
5	5.44	32.35	12.16	96.55	6.43	0.0162	22.88	0.00282	53.32	207.59
6	5.92	32.35	12.16	96.56	6.22	0.0168	22.82	0.00273	53.18	208.16
7	5.92	32.35	12.16	96.39	6.01	0.0173	22.85	0.00265	53.41	207.24
8	6.40	32.35	12.16	96.41	5.81	0.0180	22.78	0.00256	53.27	207.79
9	6.40	32.35	12.16	96.23	5.60	0.0185	22.82	0.00248	53.51	206.86
10	6.88	32.36	12.16	96.24	5.39	0.0193	22.76	0.00238	53.40	207.30
11	6.88	30.28	12.16	95.51	5.18	0.0199	22.71	0.00231	53.34	207.51
12	7.36	32.35	12.16	96.06	4.98	0.0208	22.73	0.00221	53.52	206.84
13	7.84	32.35	12.16	96.04	4.77	0.0218	22.67	0.00212	53.42	207.23
14	7.84	32.35	12.16	95.89	4.56	0.0226	22.70	0.00205	53.62	206.43
15	8.32	32.35	12.16	95.84	4.36	0.0238	22.65	0.00195	53.56	206.66
16	8.80	32.35	12.16	95.79	4.15	0.0250	22.59	0.00185	53.49	206.95
17	9.28	32.36	12.16	95.74	3.94	0.0263	22.54	0.00176	53.40	207.28
18	9.28	32.36	12.16	95.57	3.74	0.0276	22.57	0.00168	53.67	206.25
19	9.76	32.35	12.16	95.49	3.53	0.0293	22.53	0.00159	53.63	206.38
20	10.24	32.36	12.16	95.39	3.32	0.0312	22.48	0.00149	53.62	206.45
21	10.72	32.36	12.16	95.29	3.12	0.0331	22.44	0.00141	53.59	206.55

Table A3: DLW section parameters (9 cells) for
$E_0T = 15MV/m, a = 20.0mm, P_{inp} = 7.26MW$. Total attenuation $\alpha_t = 0.3Np$.

N	T_d	r_2	T_u	R_c	P_{tr}	α	Q	β_g	Z_e	P_s
	mm	mm	mm	mm	MW	Np/m	$*10^{-3}$		$M\Omega/m$	kW
1	22.24	32.35	12.16	92.43	7.26	0.0246	21.35	0.00199	48.26	358.36
2	23.20	32.35	12.16	92.10	6.90	0.0262	21.24	0.00188	47.95	360.70
3	23.68	32.35	12.16	91.90	6.54	0.0274	21.19	0.00180	47.95	360.70
4	24.64	32.35	12.16	91.54	6.18	0.0294	21.08	0.00169	47.70	362.61
5	25.60	32.35	12.16	91.16	5.82	0.0314	20.97	0.00159	47.43	364.63
6	26.56	32.35	12.16	90.78	5.45	0.0336	20.86	0.00150	47.16	366.74
7	27.52	32.35	12.16	90.38	5.09	0.0363	20.76	0.00139	46.97	368.20
8	28.00	26.87	14.08	89.34	4.72	0.0416	20.16	0.00125	43.89	394.07
9	28.00	26.83	23.20	93.01	4.32	0.0523	19.19	0.00104	38.34	451.14

SW structure cell optimization

The SW structures cell dimensions have been optimized with the same procedure. But the SW cell has seven independent parameters (Fig. A4):
- aperture radius a;
- lower drift tube radius r_1;
- upper drift tube radius r_2;
- gap length $g, \alpha_{gp} = 2g/\lambda_0$;
- drift tube cone angle ϕ;
- total web thickness T_w;
- upper circular radius r_3;
- cavity radius R_c.

For the optimization the drift cone angle was fixed to $\phi = 30^o$. The other parameters are in the limits:
- $a = (5.0 \div 30.0)mm$, six steps;
- $r_1 = (0.5 \div 9.7)mm$, five steps;
- $r_2 = (1.0 \div (2.83 - 1.5r_1)(1.33 + a/3))r_1$, four steps;
- $T_w = (0.0 \div 36.0)mm$, four steps;
- $g = (0.225\lambda_0 \div g_{max})$, ten steps;
- $r_3 = (0.2 \div 1.0)(0.25\lambda_0 - 0.5T_w)$, four steps.

As before, the cavity radius R_c was adjusted to set the resonant frequency.

After storage of the data library into the six dimensional cube, for every r_1 r_2 was fitted to have the same electric field value both at the lower and at the upper drift tube circule. Then, for the specified T_w and a an interpolation was used to find the maximum Z_e with limited $E_{smax} \leq 40.0MV/m$. The surfaces at Fig. A5 and Fig. A6 show the typical behaviour of $E_{smax}(\alpha_{gp}, r_1)/(E_0T)$ and $Z_e(\alpha_{gp}, r_1)$ surfaces. In Fig. A5 one can see the different cells with maximal Z_e for $E_0T = 5.0MV/m(a), 10.0MV/m(b)$ and $15.0MV/m(c)$, assuming $E_{smax} \leq 40.0MV/m$.

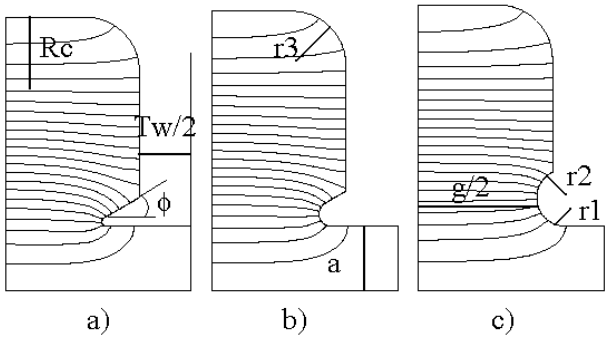

Figure A4: Geometry definition and SW cells with optimized shape for a) - $E_0T = 5.0MV/m$, b) - $E_0T = 10.0MV/m$, c) - $E_0T = 15.0MV/m$.

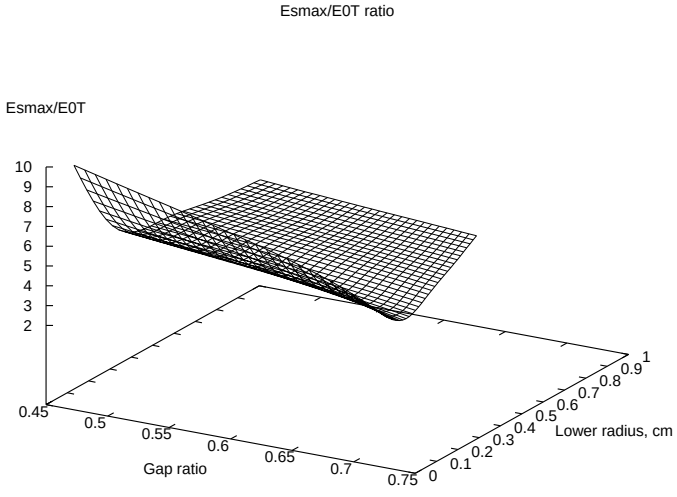

Figure A5: The surface of $E_{smax}(\alpha_{gp}, r_1)/(E_0T)$ for a SW structure cell with $a = 2.0cm, T_w = 3.0cm$.

More extended results of the cell shape optimization for different T_w, a and E_0T values are listed in the Tables A4 - A6.

Table A4: SW structure cell parameters for $T_w = 14.0mm$

a	E_0T	r_1	r_2	r_3	R_c	α_g	Z_e	T	$Q * 10^{-3}$
mm	MV/m	mm	mm	mm	mm		$M\Omega/m$		
5.00	6.00	1.79	4.76	20.12	79.02	0.46222	73.66	0.884	22.95
5.00	7.50	2.34	6.22	20.75	80.84	0.50624	70.61	0.870	23.68
5.00	9.00	2.89	7.50	20.42	81.58	0.53307	68.40	0.862	23.98
5.00	10.50	3.72	9.05	20.44	82.54	0.56563	66.01	0.850	24.37
5.00	12.00	6.30	10.95	20.34	85.08	0.64839	61.10	0.813	25.43
5.00	13.50	8.14	10.73	20.29	86.84	0.70727	57.81	0.783	26.20
5.00	15.00	9.52	10.18	20.28	88.41	0.76836	54.24	0.752	26.89
10.00	6.00	1.70	3.05	19.85	80.83	0.53192	64.61	0.843	23.56
10.00	7.50	2.34	4.19	20.33	81.77	0.55918	62.99	0.834	23.94
10.00	9.00	2.89	5.06	20.57	82.77	0.58597	61.71	0.824	24.36
10.00	10.50	3.72	6.22	20.35	83.65	0.61519	59.87	0.813	24.72
10.00	12.00	5.65	8.25	20.49	85.72	0.67994	56.17	0.785	25.61
10.00	13.50	7.68	10.14	20.41	85.91	0.69778	53.99	0.778	25.62
10.00	15.00	9.52	10.47	20.27	87.65	0.75407	51.30	0.755	26.43
15.00	6.00	1.60	2.31	19.95	82.69	0.59366	56.73	0.803	24.15
15.00	7.50	2.16	3.12	20.44	83.91	0.62455	55.89	0.792	24.70
15.00	9.00	2.80	4.07	20.15	83.40	0.62228	55.10	0.794	24.41
15.00	10.50	3.44	4.86	20.01	84.47	0.65165	54.08	0.783	24.89
15.00	12.00	4.55	6.11	20.22	86.51	0.70887	51.93	0.763	25.83
15.00	13.50	6.66	7.84	19.20	87.31	0.74531	49.50	0.752	26.14
15.00	15.00	8.14	8.57	19.50	88.27	0.77853	47.64	0.745	26.59
20.00	6.00	1.51	1.88	19.80	84.39	0.64326	49.03	0.779	24.63
20.00	7.50	2.16	2.67	19.80	84.90	0.66108	48.27	0.775	24.85
20.00	9.00	2.71	3.27	20.13	85.87	0.68683	47.59	0.769	25.32
20.00	10.50	3.54	4.18	19.64	85.72	0.69073	46.78	0.769	25.19
20.00	12.00	4.36	4.59	20.07	88.10	0.75642	45.03	0.755	26.41
20.00	13.50	6.94	6.93	17.84	87.72	0.76185	43.12	0.757	26.06
20.00	15.00	8.04	8.05	18.17	88.94	0.80069	41.60	0.755	26.70
25.00	6.00	1.42	1.54	19.70	86.32	0.68893	42.49	0.767	25.22
25.00	7.50	2.06	2.18	19.59	86.97	0.71027	41.87	0.764	25.54
25.00	9.00	2.71	2.83	19.32	86.95	0.71493	41.41	0.765	25.49
25.00	10.50	3.35	3.40	19.49	87.65	0.73522	40.84	0.762	25.85
25.00	12.00	4.27	4.26	19.41	88.98	0.77645	39.61	0.758	26.55
25.00	13.50	6.39	6.39	17.54	89.33	0.79910	37.87	0.760	26.63
25.00	15.00	8.78	8.78	16.02	89.13	0.79829	36.57	0.763	26.37
30.00	6.00	1.42	1.42	19.13	87.98	0.72189	37.17	0.764	25.62
30.00	7.50	2.06	2.07	18.94	88.46	0.73874	36.77	0.763	25.87
30.00	9.00	2.71	2.71	18.38	88.28	0.73901	36.42	0.763	25.71
30.00	10.50	3.35	3.35	18.33	88.94	0.75899	36.01	0.762	26.08
30.00	12.00	4.27	4.27	18.48	90.30	0.79976	35.17	0.760	26.85
30.00	13.50	6.48	6.48	16.10	90.54	0.81693	33.94	0.760	26.85

Table A4: SW structure cell parameters for $T_w = 22.0mm$

a	E_0T	r_1	r_2	r_3	R_c	α_g	Z_e	T	$Q * 10^{-3}$
mm	MV/m	mm	mm	mm	mm		$M\Omega/m$		
5.00	6.00	1.79	4.79	18.67	81.32	0.45000	70.59	0.890	23.26
5.00	7.50	2.43	6.43	18.67	80.73	0.45661	67.77	0.891	23.02
5.00	9.00	3.08	7.79	18.75	81.28	0.47906	65.43	0.885	23.20
5.00	10.50	3.90	9.03	18.74	83.68	0.53749	62.53	0.864	24.10
5.00	12.00	6.85	10.76	18.71	85.38	0.60315	57.94	0.835	24.70
5.00	13.50	8.41	10.40	18.67	87.27	0.66418	54.80	0.806	25.42
5.00	15.00	9.61	9.94	18.66	88.59	0.71757	51.84	0.779	25.90
10.00	6.00	1.79	3.16	18.53	81.22	0.48729	61.97	0.864	23.09
10.00	7.50	2.43	4.27	18.55	81.69	0.50672	60.36	0.858	23.25
10.00	9.00	3.08	5.27	18.65	82.41	0.52879	58.96	0.851	23.50
10.00	10.50	3.81	6.14	18.70	84.62	0.58213	56.97	0.829	24.36
10.00	12.00	6.11	8.50	18.77	85.89	0.63083	53.43	0.809	24.79
10.00	13.50	8.04	9.97	18.71	86.51	0.65713	51.37	0.797	24.99
10.00	15.00	9.61	10.06	18.74	88.08	0.70842	49.12	0.775	25.62
15.00	6.00	1.60	2.25	18.69	83.74	0.55901	54.48	0.819	23.89
15.00	7.50	2.25	3.19	18.64	83.90	0.57069	53.63	0.816	23.92
15.00	9.00	2.89	4.11	18.65	83.78	0.57532	52.87	0.815	23.83
15.00	10.50	3.63	5.05	18.87	84.77	0.60207	51.88	0.806	24.22
15.00	12.00	5.01	6.38	18.73	86.98	0.66520	49.56	0.782	25.11
15.00	13.50	6.94	7.85	18.59	87.66	0.69240	47.81	0.772	25.34
15.00	15.00	8.04	8.12	18.73	88.80	0.73057	46.17	0.761	25.82
20.00	6.00	1.51	1.85	18.72	85.24	0.60365	47.31	0.793	24.23
20.00	7.50	2.25	2.79	18.61	84.76	0.60086	46.59	0.795	23.98
20.00	9.00	2.80	3.35	18.63	85.83	0.62851	45.98	0.788	24.43
20.00	10.50	3.63	4.17	18.79	86.44	0.64737	45.18	0.783	24.67
20.00	12.00	4.27	4.33	18.79	88.53	0.70767	43.63	0.769	25.61
20.00	13.50	6.76	6.76	18.26	88.57	0.71745	42.13	0.768	25.54
20.00	15.00	9.15	9.15	18.01	88.67	0.72417	40.73	0.767	25.50
25.00	6.00	1.51	1.62	18.73	86.09	0.62414	41.36	0.783	24.24
25.00	7.50	2.16	2.27	18.68	86.78	0.64489	40.85	0.780	24.54
25.00	9.00	2.80	2.91	18.48	86.88	0.65165	40.38	0.779	24.55
25.00	10.50	3.44	3.44	18.54	87.82	0.67759	39.82	0.774	24.99
25.00	12.00	4.27	4.28	18.85	89.29	0.72039	38.84	0.768	25.69
25.00	13.50	6.30	6.30	17.61	89.70	0.74200	37.43	0.767	25.82
30.00	6.00	1.42	1.42	18.69	88.41	0.66902	36.35	0.774	24.92
30.00	7.50	2.06	2.06	18.78	88.94	0.68575	36.03	0.772	25.17
30.00	9.00	2.71	2.71	18.53	88.78	0.68526	35.74	0.772	25.05
30.00	10.50	3.35	3.35	18.18	89.36	0.70420	35.37	0.770	25.34
30.00	12.00	4.18	4.18	18.29	90.54	0.74019	34.76	0.767	25.95
30.00	13.50	6.66	6.66	15.93	90.39	0.74496	33.70	0.767	25.72

Table A6: SW structure cell parameters for $T_w = 30.0mm$

a	E_0T	r_1	r_2	r_3	R_c	α_g	Z_e	T	$Q * 10^{-3}$
mm	MV/m	mm	mm	mm	mm		$M\Omega/m$		
5.00	6.00	1.70	4.28	17.02	84.15	0.45268	64.37	0.890	23.38
5.00	7.50	2.43	6.14	17.09	83.19	0.45000	62.72	0.895	23.05
5.00	9.00	3.17	7.66	17.12	82.72	0.45502	60.82	0.895	22.87
5.00	10.50	4.18	8.98	16.98	84.81	0.51172	57.46	0.876	23.55
5.00	12.00	7.12	10.42	17.02	86.17	0.56861	53.47	0.851	23.95
5.00	13.50	8.60	10.14	17.06	87.79	0.62429	50.65	0.826	24.46
10.00	6.00	1.88	3.21	17.45	82.01	0.45000	57.99	0.880	22.55
10.00	7.50	2.52	4.27	17.31	82.58	0.47099	56.43	0.874	22.72
10.00	9.00	3.26	5.39	17.33	82.87	0.48583	55.00	0.869	22.79
10.00	10.50	4.00	6.09	16.95	85.53	0.54981	52.68	0.845	23.69
10.00	12.00	6.66	8.77	16.95	86.14	0.58381	49.54	0.831	23.82
10.00	13.50	8.23	9.44	17.02	87.44	0.62484	47.63	0.813	24.25
15.00	6.00	1.79	2.50	17.57	83.06	0.49303	51.03	0.847	22.71
15.00	7.50	2.43	3.41	17.44	83.28	0.50528	50.18	0.844	22.76
15.00	9.00	2.98	4.11	17.18	84.63	0.53783	49.43	0.832	23.23
15.00	10.50	3.90	5.27	17.38	85.35	0.56006	48.36	0.824	23.46
15.00	12.00	5.84	7.00	17.05	87.09	0.61306	46.19	0.804	24.03
15.00	13.50	7.22	7.59	17.10	88.15	0.64640	44.80	0.791	24.40
20.00	6.00	1.60	1.92	17.36	85.51	0.55281	44.51	0.811	23.35
20.00	7.50	2.34	2.83	17.42	85.22	0.55298	43.88	0.812	23.20
20.00	9.00	2.98	3.51	17.21	85.71	0.56883	43.27	0.808	23.36
20.00	10.50	3.81	4.22	17.28	86.92	0.60057	42.46	0.799	23.81
20.00	12.00	4.36	4.35	17.02	88.89	0.65913	41.04	0.784	24.57
20.00	13.50	7.03	7.03	17.16	88.90	0.66342	39.89	0.782	24.51
25.00	6.00	1.60	1.70	17.39	86.50	0.57446	39.07	0.797	23.39
25.00	7.50	2.25	2.33	17.38	87.01	0.59037	38.65	0.794	23.58
25.00	9.00	2.89	2.94	17.26	87.28	0.60030	38.23	0.792	23.67
25.00	10.50	3.54	3.53	17.16	88.25	0.62739	37.70	0.787	24.07
25.00	12.00	4.46	4.46	17.28	89.62	0.66824	36.83	0.779	24.64
25.00	13.50	7.12	7.12	16.39	89.48	0.66928	35.69	0.779	24.47
30.00	6.00	1.42	1.42	17.30	88.97	0.62148	34.54	0.784	24.07
30.00	7.50	2.16	2.16	17.43	89.01	0.62534	34.27	0.783	24.06
30.00	9.00	2.71	2.71	17.33	89.49	0.64036	34.03	0.781	24.27
30.00	10.50	3.44	3.44	17.10	89.68	0.64830	33.72	0.780	24.33
30.00	12.00	4.36	4.36	17.22	90.86	0.68373	33.22	0.776	24.87
30.00	13.50	7.49	7.49	14.79	89.97	0.66604	32.02	0.777	24.23

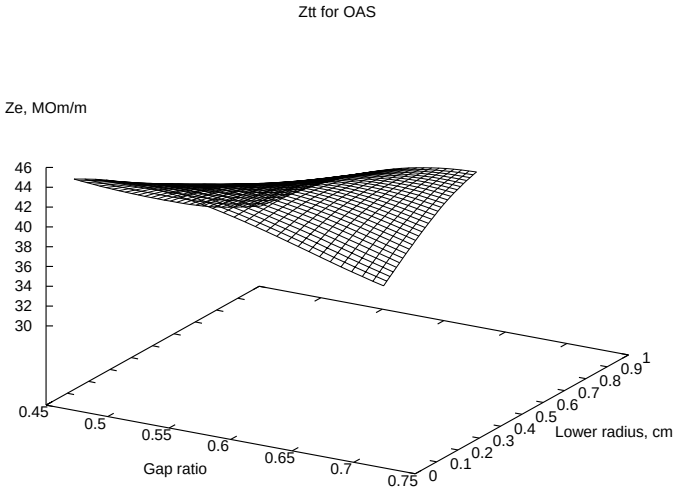

Figure A6: The surface of $Z_e(\alpha_{gp}, r_1)$ for a SW structure cell with $a = 2.0cm, T_w = 3.0cm$.